NUMERICAL SIMULATION OF THERMAL CONVECTION UNDER THE
INFLUENCE OF A MAGNETIC FIELD BY USING SOLENOIDAL BASES

A THESIS SUBMITTED TO
THE GRADUATE SCHOOL OF NATURAL AND APPLIED SCIENCES
OF
MIDDLE EAST TECHNICAL UNIVERSITY

BY

DURMUŞ YARIMPABUÇ

IN PARTIAL FULFILLMENT OF THE REQUIREMENTS
FOR
THE DEGREE OF DOCTOR OF PHILOSOPHY
IN
ENGINEERING SCIENCE

JUNE 2011

Approval of the thesis:

NUMERICAL SIMULATION OF THERMAL CONVECTION UNDER THE INFLUENCE OF A MAGNETIC FIELD BY USING SOLENOIDAL BASES

submitted by **DURMUŞ YARIMPABUÇ** in partial fulfillment of the requirements for the degree of
Doctor of Philosophy in Engineering Science Department, Middle East Technical University by,

Prof. Dr. Canan Özgen
Dean, Graduate School of **Natural and Applied Sciences** _____

Prof. Dr. Turgut Tokdemir
Head of Department, **Engineering Science** _____

Assoc. Prof. Dr. Hakan I. Tarman
Supervisor, **Department of Engineering Sciences, METU** _____

Examining Committee Members:

Prof. Dr. Münevver Tezer
Dept. of Mathematics, METU _____

Assoc. Prof. Dr. Hakan I. Tarman
Dept. of Eng. Sci., METU _____

Assoc. Prof. Dr. Erol Kurt
Faculty of Tech. Edu., Gazi University _____

Assoc. Prof. Dr. Utku Kanoğlu
Dept. of Eng. Sci., METU _____

Assist. Prof. Dr. Cüneyt Sert
Dept. of Mech. Eng., METU _____

Date: _____

I hereby declare that all information in this document has been obtained and presented in accordance with academic rules and ethical conduct. I also declare that, as required by these rules and conduct, I have fully cited and referenced all material and results that are not original to this work.

Name, Last Name: DURMUŞ YARIMPABUÇ

Signature   :

ABSTRACT

NUMERICAL SIMULATION OF THERMAL CONVECTION UNDER THE
INFLUENCE OF A MAGNETIC FIELD BY USING SOLENOIDAL BASES

Yarımpabuç, Durmuş

Ph.D., Department of Engineering Science

Supervisor   : Assoc. Prof. Dr. Hakan I. Tarman

June 2011, 110 pages

The effect of an imposed magnetic field on the thermal convection between rigid plates heated from below under the influence of gravity is numerically simulated in a computational domain with periodic horizontal extent. The numerical technique is based on solenoidal basis functions satisfying the boundary conditions for both velocity and induced magnetic field. The expansion bases for the thermal field are also constructed to satisfy the boundary conditions. The governing partial differential equations are reduced to a system of ordinary differential equations governing the time evolution of the expansion coefficients under Galerkin projection onto the subspace spanned by the dual bases. In the process, the pressure term in the momentum equation is eliminated. The system validated in the linear regime is then used for some numerical experiments in the nonlinear regime.

Keywords: Thermal convection, Magnetic fields, Solenoidal Bases, Legendre Polynomials

ÖZ

MANYETİK BİR ALAN ETKİSİNDE ISIL KONVEKSİYON HAREKETİNİN SOLENOİDAL BAZ KULLANIMI İLE SAYISAL BENZETİMİ

Yarımpabuç, Durmuş

Doktora, Mühendislik Bilimleri Bölümü

Tez Yöneticisi   : Doç. Dr. Hakan I. Tarman

Haziran 2011, 110 sayfa

Manyetik bir alanın etkisi altında ve yerçekimi ortamında alttan ısıtılan iki rijid plaka arasında oluşan ısıl konveksiyon hareketi yatay yönlerde periyodik kabul edilen bölgede sayısal benzetim yoluyla oluşturulmuştur. Sayısal metod hız ve indüklenmiş manyetik alan değişkeninin sınır şartlarını sağlayan solenoidal baz fonksiyonları cinsinden yazılmasına dayanmaktadır. Sıcaklık değişkenide sınır şartlarını sağlayan baz fonksiyonları cinsinden yazılmıştır. Hareketi modelleyen kısmi diferansiyel denklemler çifteş baz fonksiyonları tarafından karşılanan alt uzaya Galerkin yöntemiyle yansıtılarak zamana bağlı açılım katsayılarının evrimini modelleyen adi diferansiyel denklem sistemine indirgenmiştir. Bu işlem sırasında, momentum denkleminde bulunan basınç terimi ortadan kalkmaktadır. Doğrusal akış rejiminde doğrulanan bu sistem, doğrusal olmayan akış rejiminde çeşitli sayısal deneyler için kullanılmıştır.

Anahtar Kelimeler: Termal konveksiyon, Manyetik alan, Solenoidal bazlar, Legendre polinomları

to my family

ACKNOWLEDGMENTS

I would like to express my gratitude to all those who gave me the possibility to complete this thesis.

First and foremost I offer my sincerest gratitude to my supervisor, Assoc. Prof. Dr. Hakan I. Tarman, who has supported me throughout my thesis with his patience, continuous support, knowledge, stimulating suggestions, criticism and encouragement and helped me in all the time of research and writing of this thesis.

During my PhD period, I thank my parents for supporting me throughout all my studies at University, and encouraging me to go ahead with my thesis. I furthermore wish to express my deepest gratitude to each member of my family for providing me a comfortable and excellent environment.

In my daily work I would like to thank my friends, Cihan Yıldırım, Baran Aydın, Eray Arslan, Volkan İşbuğa, Ozan Tuğluk, Ersan Güray, Sevgi Özen and Cengizhan Durucan for their help, suggestions and friendship.

TABLE OF CONTENTS

LIST OF TABLES

LIST OF FIGURES

FIGURES

CHAPTER 1

INTRODUCTION

In many astrophysical and geophysical contexts, magnetoconvection plays an important role. There are two aspects of the interaction between magnetic fields and convection: on the one hand, the motion sweeps magnetic flux aside and concentrates it; on the other, the Lorentz force affects, and may suppress the pattern of convection. In the outer layers of the Sun and Earth's core thermal convection is affected by the presence of the magnetic fields, the existence of the sunspot indicates the suppression of convections by sufficiently strong magnetic fields. It is well known that unavoidable hydrodynamic movements can be damped with help of a magnetic field, therefore magneto-convection has become relevant in material processing facilities, such as molten metal casting and crystallization. For instance, the investigations of heat transfer for melt flows under crystal growth conditions permit one to qualify the critical operating parameters of crystal growth. The study of Oreper and Szekely [23] shows that the magnetic field suppress the natural-convection currents and the magnetic field strength is one of the most important factors of crystal formation.

In this study, the effect of an imposed magnetic field on the thermal convection between rigid plates heated from below under the influence of gravity is numerically simulated in a computational domain with periodic horizontal extent. As the liquid is heated, it warms, expands and rises because it is less dense. When it reaches upper cool boundary it transfers its energy, cools down, becomes denser and falls. Flow is driven by the heat source and resists against gravity and magnetic fields. The gravity acts in the direction of heat transfer, while Lorentz force due to magnetic induction acts in the opposite direction of gravity. Thus, the total heat transfer is reduced considerably due to the braking effect of Lorentz force. Since, the problem of the ordinary hydrodynamics nearly doubles in dimension by inserting magnetic variables into the system, it is no wonder that the magnetic convection exhibits a rich

variety of new phenomena, such as oscillatory onset of convection and subcritical steady finite amplitude convection. Further, the increase in the convective heat transport with supercritical Rayleigh number is more rapid in the presence of magnetic field than nonmagnetic case. In addition, magnetic field has a stabilizing effect on the oscillatory convection. The object of the study is to obtain numerical solution for the velocity and temperature fields between rigid plates and to determine the effects of magnetic field strength on the convective transport phenomena.

The numerical technique that we use in this study is based on solenoidal basis functions satisfying the boundary conditions for both velocity and induced magnetic field, therefore the number of model equations reduce from nine to four equations which are the momentum and energy equations. Dimensionless form of these equations involve well known parameters, Rayleigh number (Ra), Chandrasekhar number (Q), thermal Prandtl number (Pr) and magnetic Prandtl number (Pm). Rayleigh number for a fluid is associated with the heat transfer within the fluid and describes the ratio of buoyancy force driven by temperature difference to viscous dissipative effect. Chandrasekhar number is the ratio of the viscous dissipation to Joule dissipation that is an appropriate measure of the strength of the magnetic flux density. The thermal Prandtl Number is the ratio of kinematic viscosity, ν to thermal diffusivity, κ. The magnetic Prandtl number the ratio of kinematic viscosity to the magnetic diffusivity λ. The ratio of thermal to magnetic Prandtl number (Pm/Pr) is shown to be important in the dynamics of the magnetoconvection. When the Pm/Pr is small, that is $\kappa \ll \lambda$, magnetoconvection exhibits a particularly rich variety of behavior. This limit is appropriate for liquid metals and the analysis thus applies to laboratory as well as to planetary cores, but the problem of astrophysical interest such as the convection in penumbra of sunspot are not covered in this limit. However, the physical mechanisms underlying the mathematical results are persistent in more general cases; the assumed limit just serves to isolate them from other effects. In this study, we concentrate on situations where this ratio becomes very small.

1.1 Earlier Research

Rayleigh-Bénard convection in an electrically conducting fluid in the presence of magnetic field has long been interest to fluid dynamics mainly due to its importance in astrophysics and planetary physics applications. Rayleigh-Bénard convection in the context of magne-

tohydrodynamics has been examined by Thompson [1] in 1951 and Chandrasekhar [2] in 1952 with a linear constitutive relationship between magnetic field and magnetic induction. In 1955, Lehnert [3] stated that the uniform magnetic field has damping effect on turbulence in conducting fluids and modeled the problem by the linear equations. In 1963, Deissler [6] analyzed these equations numerically. Then Nestlerade and Lumey [7] used Taylor series expansion of the variables in time to solve the problem of the strong magnetic field. Nakagawa reported some experiments on the magnetic inhibition of thermal convection in horizontal layers of mercury heated from below in the studies [8] and [9]. Permanent and cyclotron magnets reconditioned for hydromagnetic studies were used in these experiments. This work was determined the dependence of the critical Rayleigh number for the onset of instability and confirmed the experimental results with the theoretical results driven by Chandrasekhar [2]. Further, He reported some measurements of the heat flux and notes the increased efficiency of the convection heat transport with increasing field strength. Linear theory of the magnetoconvection is extensively discussed in Chandrasekhar (1961) [5] for different boundary conditions and the results are in agreement with the experiments of Nakagava [8]- [9]. The relationship between critical Rayleigh number and magnetic number was shown in these experiments. The first systematic study of non-linear magnetoconvection results were performed by Spiegel [10] and Weiss [11]. Nonlinear aspect of thermal convection in a fluid layer heated from below in the presence of magnetic field investigated by Busse [12] who studied the subcritical finite amplitude convection. Fauve et al. [13] showed that the increase in the magnetic field in the horizontal directions generates a new convective pattern, with two-dimensional rolls parallel to the magnetic field direction, which is in agreement with the theoretical predictions of Chandrasekhar [5]. They observed that a horizontal magnetic field has an inhibition effect on the oscillatory instability in a mercury layer. A general review of non-linear analysis of magnetoconvection is given by Proctor and Weiss [14].

There exists a series of research papers [15]-[17] by Busse and Clever where they cover different aspects of magnetoconvection in the case of $\kappa \ll \lambda$. They showed that the onset of the oscillatory instability is delayed and by further increasing the intensity of the magnetic field the convection rolls become stable. In their study, they deal with the numerical analysis of convection rolls and their stability for various Prandtl numbers on the limit of a high ratio of magnetic to thermal diffusivity. Theoretical study of magnetic inhibition effect on the stability of two-dimensional convection rolls in a horizontal fluid layer heated from below

3

is performed in the work of the Busse and Clever [15]. They pointed out that convection assumes the form of the two dimensional rolls near the critical value of the Rayleigh number. And, the stability region of the rolls was investigated by analyzing various instabilities in [15]. A horizontal homogeneous magnetic field intersecting the layer is discussed in Busse and Clever [16] where they investigated the effect of a purely horizontal magnetic field on the onset of three-dimensional instabilities. They indicated that as long as Rayleigh number is close to its critical value and the horizontal magnetic field is aligned with the convection rolls, the Lorentz force has stabilizing influence on the onset of oscillatory instability. In [17], a systematic study of convection rolls in a fluid layer heated from below for $Pr = 0.1$ and $Pr = 0.025$ is described, which is related to studies of convection rolls and their stability in the presence of a vertical magnetic field [15]. They showed that the onset of the oscillatory instability reduces the heat transport by convection, and even though the magnetic field has an inhibiting influence on steady convection, the effect on the onset of oscillatory instability is much stronger such that in the presence of magnetic field higher heat transport is obtained in some cases than in its absence. Convection in the presence of oblique magnetic field is studied in [18]. The results of vertical and horizontal magnetic field are compared and they showed that the horizontal field has more inhibiting effect on the instability than the vertical magnetic field and further the horizontal magnetic field on the perfectly conducting boundaries has more stabilizing influence on the onset of oscillations than on the insulating boundaries. They further pointed out that the horizontal magnetic field has the most inhibiting effect on the onset of the oscillatory instability whereas its effect on steady two-dimensional convection is nil. In 1996, the thermal convection is numerically simulated in the case of a strong vertical magnetic field permeating the layer by Clever and Busse [19]. They reported that the heat transport decreases with increasing Rayleigh number for steady three-dimensional convective flows as well as for time periodic flows. Further, under the influence of strong magnetic field, they observed higher order instabilities and time-dependent flows in infinite horizontal fluid layer. They showed that the stability limits of distinct flow regimes are shifted to higher Rayleigh numbers as Chandrasekhar number is increased.

Ozoe and Maruo [20] numerically investigated the natural convection of a low Prandtl number fluid in the presence of a magnetic field and obtained correlations for Nusselt number in terms of Rayleigh, Prandtl and Hartmann numbers. Mössner and Müller [25] investigated the flow patterns for various thermal boundary conditions and directions of the magnetic field by

looking over closure patterns of the electric currents and the resulting Lorentz forces in insulated rectangular cavities. They showed that magnetic field perpendicular to the heated wall was most effective in damping the natural convection whereas the parallel field resulted in the least damping. Further, the number of the convection rolls associated with the Hartmann and the Rayleigh numbers such that increasing the Rayleigh numbers decrease and increasing Hartmann numbers increase the number of convection rolls in cavity. In 2001, Aurnou and Olson [36] performed an experimental study to measure heat transfer in rectangular box for low Prandtl number ($Pr = 0.023$) on an electrically conducting fluid as a function of the temperature, rotation, magnetic field strength and fluid-layer aspect ratio. They demonstrated the effect of rotation and magnetic fields on the onset of the thermal convection and convective heat transfer in liquid gallium. In their experimental study, they found a relationship between Rayleigh and Nusselt numbers for Rayleigh-Bénard convection, magnetoconvection and rotating magnetoconvection. For magnetoconvection, they found that critical Rayleigh number increases linearly with magnetic field. Further, they indicated that the vertical magnetic field and rotation have both individually inhibiting effects on the onset of convection, but they observed a reduction in convective heat transfer when both are applied to the system. The influence of a vertical magnetic field on liquid metal Rayleigh-Bénard convection is studied experimentally by Burr and Müller [38] for heat transfer and local temporal behavior for highly supercritical condition, which is most relevant for technical applications. They showed that the damping of the temperature field fluctuations by magnetic field depends on the frequency. Long term fluctuations are strongly damped by magnetic field whereas short term fluctuations are less damped or may even be enhanced. In addition, the intensity of the temperature fluctuations is always decreased by increasing the intensity of the magnetic field at large supercritical Rayleigh numbers. The problem of convection by radial buoyancy in an electrically conducting fluid contained by a rotating cylindrical annulus in the presence of horizontal magnetic field in the azimuthal direction is considered in the studies of Kurt et al. [[46],[47]]. They used a small gap approximation to reduced the problem to the case of a horizontal fluid layer, which is heated from below. They introduced some detailed results on instabilities and pattern formation. Güray and Tarman [37] used an efficient computational scheme based on spectral element method in order to simulate magnetoconvective flow in liquid melts. They did not use staggered grid approach in the treatment of the pressure terms, commonly used in literature, instead Legendre polynomials and rescaled Legendre-Lagrangian polynomial interpolation are used in the expansion of the pressure and the other variables in the variational

weak formulation, respectively. Although divergence conditions of the problem is not satisfied exactly, the method gave satisfactory results for some regions when the solutions are sufficiently smooth. Yarımpabuç and Tarman [49] used solenoidal bases method to analyse the effect of the vertical magnetic field on the thermal convection. They observed that this technique gave satisfactory results for both linear and nonlinear regimes.

1.2   Scope of the work

In modeling incompressible flows, the flow field is restricted to satisfy the divergence-free condition or the continuity equation. This is an important hurdle to be overcome in the numerical simulation studies. For this purpose, various techniques have been employed in literature such as the fractional step [21], the influence matrix [22] and the staggered grid [24] methods. The common focus in these techniques is to numerically treat the pressure variable which usually comes without any boundary conditions and whose role is to enforce the divergence-free condition on the flow. On the other hand, these techniques help to enforce the divergence-free condition only to a certain limited degree of accuracy. Accurate handling of the divergence-free condition is important in numerical hydrodynamic stability studies where the flow is perturbed to identify the critical parameter values between the transitory regimes. Furthermore, the numerical simulation studies of flow under the influence of a magnetic field encounter an additional divergence-free condition on the magnetic field variable. Various numerical approaches [25]-[15] have been used for this purpose and the effects of the poor handling of the divergence-free condition [26] and some remedies [27] are presented in literature.

In this work, we present some preliminary results on the use of solenoidal (divergence-free) bases expansion in the numerical simulation of thermal convection under the influence of an oblique magnetic field. By introducing an expansion in terms of the solenoidal basis functions for the velocity and the magnetic field into the model equations in a Galerkin projection, both divergence-free criteria are exactly satisfied and the pressure variable is completely eliminated, thus the number of equations and the number of flow variables are reduced. This reduces the burden on the numerical technique and increases the accuracy with which the divergence-free condition is satisfied. While the velocity solenoidal basis functions are generated independently, a quasi-steady relationship between the velocity and the magnetic field

variables is used to generate the corresponding magnetic solenoidal basis functions. This relationship arises in the case of liquid metals or melts as the convective fluid. Some studies that use solenoidal bases in literature are Busse & Clever [15], Leonard & Wray [28], Moser, Moin & Leonard [29], Mhuiris [30], Pasquarelli, Quarteroni & Sacchi [31], Kessler [32], Noack & Eckelmann [33], Meseguer & Trefethen [34] and Tarman [35].

This thesis can be outlined in the following way: In Chapter 2, the geometry of the problem, the system of model partial differential equations and forcing terms coming from an oblique magnetic field are constructed for incompressible fluids under the Boussinesq approximation. And then the nondimensionalization is performed in accordance with Chandrasekhar [5] in order to present the dimensionless numbers. In addition, the boundary conditions for velocity, temperature and magnetic field are constructed in both horizontal and vertical directions. In Chapter 3, solenoidal basis functions for the velocity and temperature field which satisfy the divergence free constraint and the boundary conditions of the system exactly, are constructed and, further dual bases are constructed to characterize the projection space, such that, the pressure term is eliminated from the system. Solenoidal magnetic bases are generated using the velocity solenoidal bases by utilizing the quasi-steady relationship for the cases of oblique, vertical and horizontal magnetic fields, separately. In Chapter 4, a weak solution is obtained by applying Galerkin projection to the partial differential equations. The discretization in the horizontal directions in the form of Fourier expansion and in the vertical direction in the form Legendre polynomials based on the Legendre-Gauss-Lobatto quadrature are described. In addition, velocity and magnetic solenoidal bases are presented in detail as a function of the angle of the magnetic field applied to the system. Moreover, the time discretization of the system and the implementation of the nonlinear terms are explained. In Chapter 5, linear and nonlinear numerical simulation under a vertical magnetic field is presented. The linear stability analysis of the system are performed by dropping the nonlinear terms in accordance with the perturbation theory and the results are compared with [5]. Nonlinear analysis in stationary and time-dependent flow regimes is presented in two different sections and the results are compared with some numerical and experimental work in literature. In the last chapter, linear and nonlinear analysis is performed in the case of external oblique magnetic field. The linear analysis is performed and the effects of four different parameters, which are the magnetic field strength, the wavenumber, the angle of the magnetic field applied and Rayleigh number are examined. Lastly, nonlinear numerical simulation of the oblique magnetic field with various

angles is performed and the effect of the angle on the flow is discussed for different flow parameters.

CHAPTER 2

MAGNETO-CONVECTION PROBLEM

2.1 Governing Equations

Thermal convective motion of a perfectly conducting fluid is considered in a periodic horizontal layer of thickness d between conducting plates that are heated from below under the influence of a uniform magnetic field B_0 applied externally in the yz plane with angle χ from y axis (Figure 2.1).
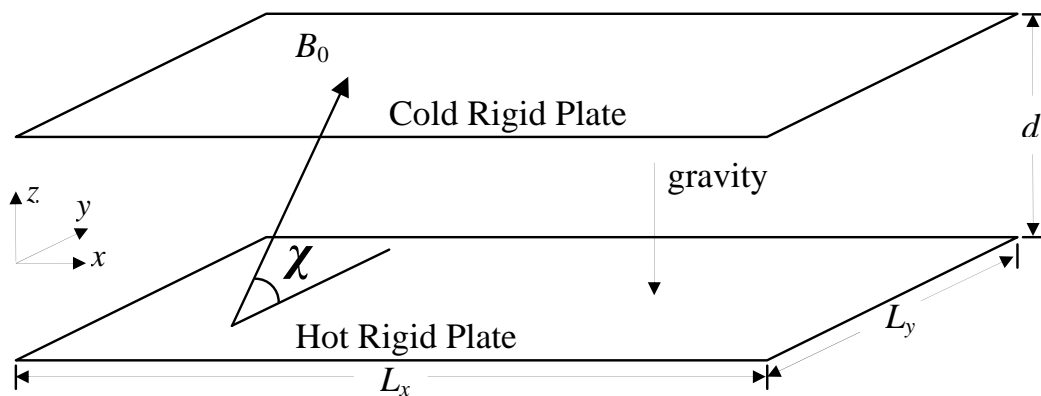
Figure 2.1: The geometry of the periodic convective domain

When a temperature difference is maintained across the horizontal fluid layer by heating from below and cooling from above, the fluid flows in a pattern of convection rolls if the temperature difference between plates exceeds a threshold value. The fluid motion transports additional heat over that carried by thermal conduction through the fluid. Many variations

on this process have been studied in the laboratory since Bénard's first experiments around the turn of the century. The onset of convection is the typical example of a pattern forming instability. This simplest and most studied version is Rayleigh-Bénard convection, shown schematically below in Figure 2.2.
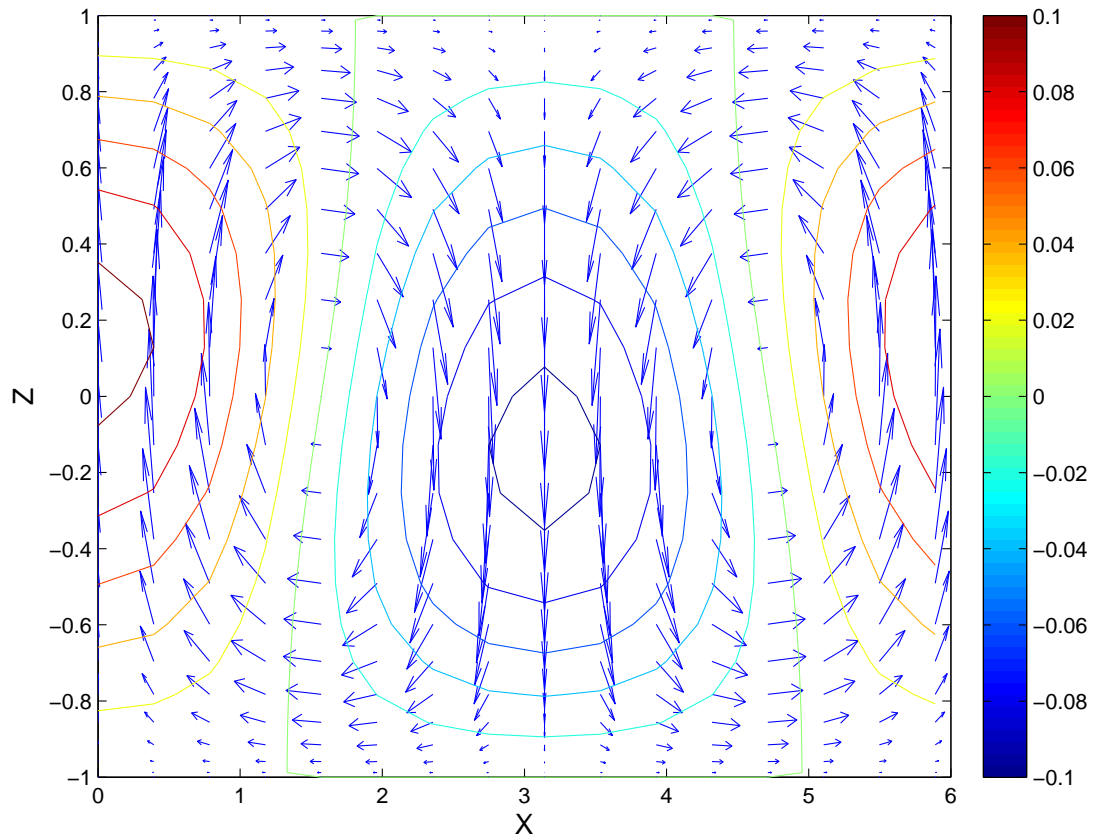
Figure 2.2: Roll motion of the fluid between hot and cold plates

In Figure 2.2 the fluid is confined between rigid plates which are held at constant temperatures with the hot plate below. Here, the arrows indicate the velocity field and the contours shows isothermal lines. In a classic 1916 paper, Lord Rayleigh showed that initially motionless fluid layer becomes unstable to small flow perturbations when the temperature difference is sufficiently large. Flow perturbations grow when the buoyancy forces on a perturbed parcel of fluid become sufficient to overcome dissipation due to viscosity. Hot fluid near the bottom thermally expands and becomes lighter than the fluid above it, so it rises, cools and returns in an overturning flow. In this study, this motion is opposed by a uniform magnetic field B_0

in addition to the viscosity of the fluid and the tendency of thermal diffusion to smooth out temperature gradients.

A mathematical model for magneto-convection is obtained by coupling the equations for the fluid motion and the classical electromagnetism. In other words, incompressible Navier-Stokes equations with Lorentz body force, which is derived from Maxwell equations and Ohm's law, forms the magneto-convection equations. The model equations for the convective motions are obtained using Boussinesq approximation under the assumption of small temperature difference between the two plates. Under this assumption the density variation with temperature is small and yet the motion is driven by buoyancy force which results from neglecting the variation of density everywhere except at the buoyancy term. Here, the density is assumed to obey the following relation:

$$\rho = \rho_o[1 - \beta(T - T_o)] \tag{2.1}$$

where T_o and T are the temperatures of the bottom and top layer, respectively, ρ_0 is the density of the fluid at the temperature T_0 and β is the coefficient of the volumetric expansion, which is a small number for gas and liquids as stated in Chandrasekhar [5] and Davidson [40].

Conservation of mass and momentum equations for incompressible fluids under the Boussinesq approximation and an external magnetic field can be written in cartesian coordinates as:

$$\nabla \cdot \mathbf{u} = 0 \tag{2.2}$$

$$\frac{\partial \mathbf{u}}{\partial t} + (\mathbf{u} \cdot \nabla) \mathbf{u} = -\frac{1}{\rho_o} \nabla P - \frac{\rho}{\rho_o} g \mathbf{e}_z + \nu \nabla^2 \mathbf{u} + \frac{1}{\rho_o} (\mathbf{J} \times \mathbf{B}) \tag{2.3}$$

$$\frac{\partial T}{\partial t} + (\mathbf{u} \cdot \nabla) T = \alpha \nabla^2 T \tag{2.4}$$

where $\mathbf{e}_z$ is the direction vector opposite to gravity, P is the pressure, $\mathbf{u} = (u, v, w)$ is the velocity vector, ρ_o is the density at a reference temperature T_o, $\mathbf{J}$ is the current density, $\mathbf{B}$ is the magnetic field, ν is kinematic viscosity, α is the thermal diffusivity and g acceleration of gravity. Here, (2.4) denotes the equation that governs the evolution of temperature. The additional forcing term in the equations of motion is the Lorentz force generated by the interaction of the imposed magnetic field with the currents induced by the fluids. This Lorentz force term in (2.3) can be rewritten by using the differential form of Ampére's law:

$$\nabla \times \mathbf{B} = \mu \mathbf{J}. \tag{2.5}$$

where μ is the magnetic permeability. The current density is eliminated by using the relation in (2.5) and then the equation (2.3) take the following form:

$$\frac{\partial \mathbf{u}}{\partial t} + (\mathbf{u} \cdot \nabla)\mathbf{u} = -\frac{1}{\rho_o}\nabla P - \frac{\rho}{\rho_o}ge_z + \nu\nabla^2\mathbf{u} + \frac{1}{\mu\rho_o}(\nabla \times \mathbf{B} \times \mathbf{B}). \tag{2.6}$$

The linear algebraic relation

$$\nabla \times \mathbf{B} \times \mathbf{B} = -\nabla\left(\frac{\mathbf{B} \cdot \mathbf{B}}{2}\right) + (\mathbf{B} \cdot \nabla)\mathbf{B} \tag{2.7}$$

is used in order to write the Lorentz term in a simpler manner in (2.6):

$$\frac{\partial \mathbf{u}}{\partial t} + (\mathbf{u} \cdot \nabla)\mathbf{u} = -\frac{1}{\rho_o}\nabla\left(P + \frac{|\mathbf{B}|^2}{2\mu}\right) - \frac{\rho}{\rho_o}ge_z + \nu\nabla^2\mathbf{u} + \frac{1}{\mu\rho_o}(\mathbf{B} \cdot \nabla)\mathbf{B}. \tag{2.8}$$

In addition to these, the relation between velocity field, $\mathbf{u}$ and the magnetic field, $\mathbf{B}$,which are contained in Maxwell's equations, are used. Since we are not concerned with the effects of propagation of electromagnetic waves, the displacement currents are ignored in comparison with current density in Maxwell's equations. In magnetohydrodynamics equations, charge density and charge conservation are relatively small, so they are dropped as well Chandrasekhar [5] and Davidson [40]. Thus the reduced form of Maxwell's equations for magnetohydrodynamics can be written in the following form:

$$\nabla \cdot \mathbf{B} = 0 \tag{2.9}$$

$$\nabla \times \mathbf{E} = -\frac{\partial \mathbf{B}}{\partial t} \tag{2.10}$$

together with (2.5). Here, $\mathbf{E}$ is the electric field. According to the Ohm's law, current density can be stated by using electric field measured in a frame moving with the local velocity of the conductor:

$$\mathbf{J} = \sigma(\mathbf{E} + \mathbf{u} \times \mathbf{B}) \tag{2.11}$$

where σ is the coefficient of the electrical conductivity. In order to find a relation between velocity, $\mathbf{u}$ and magnetic field, $\mathbf{B}$, first, the electric field, $\mathbf{E}$, in (2.11) is substituted into (2.10):

$$\frac{\partial \mathbf{B}}{\partial t} = -\nabla \times \left(\frac{\mathbf{J}}{\sigma} - \mathbf{u} \times \mathbf{B}\right) \tag{2.12}$$

and then by using Ampére's law relation (2.5), the current density is put into to (2.12), to get:

$$\frac{\partial \mathbf{B}}{\partial t} = -\nabla \times \left(\frac{\nabla \times \mathbf{B}}{\sigma\mu} - \mathbf{u} \times \mathbf{B}\right) \tag{2.13}$$

12

or it can be represented in a simple manner by using some vector identities:

$$\frac{\partial \mathbf{B}}{\partial t} = -(\mathbf{u} \cdot \nabla)\mathbf{B} + (\mathbf{B} \cdot \nabla)\mathbf{u} + \lambda\nabla^2\mathbf{B} \tag{2.14}$$

where λ is the magnetic diffusivity and represented in a combined form as follows:

$$\lambda = \frac{1}{\sigma\mu}. \tag{2.15}$$

The total flow and temperature field can be decomposed into steady state and perturbation about this state:

$$\mathbf{u}(x, y, z, t) = \mathbf{0} + \mathbf{u}'(x, y, z, t) \tag{2.16}$$

$$P(x, y, z, t) = \bar{P}(z) + P'(x, y, z, t) \tag{2.17}$$

$$T(x, y, z, t) = \bar{T}(z) + \Theta'(x, y, z, t) \tag{2.18}$$

and the total magnetic field consists of two parts: externally imposed uniform magnetic field, B_o applied in the direction $\mathbf{e}_B$ in the yz plane with angle χ from y axis and the induced magnetic field $\mathbf{b}'$ which is created due to the convective motions:

$$\mathbf{B}(x, y, z, t) = B_o\mathbf{e}_B + \frac{\kappa}{\lambda}\mathbf{b}'(x, y, z, t), \tag{2.19}$$

with

$$\mathbf{e}_B = Cos\chi\mathbf{e}_y + Sin\chi\mathbf{e}_z \tag{2.20}$$

where κ is the thermal diffusivity, $\mathbf{e}_y$ and $\mathbf{e}_z$ are unit vectors in horizontal $y-$direction and vertical $z-$direction, respectively. Here, overbar shows the conduction state and prime shows the convection state. In conduction (no-motion) state, there is no convection so the pressure and temperature fields, $\bar{P}$ and $\bar{T}$ vary only in the vertical z direction. Thus, using the density relation (2.1) in conduction state, the governing equations (2.4) and (2.8) takes the following form:

$$\frac{1}{\rho_o}\frac{\partial \bar{P}}{\partial z} = -[1 - \beta(\bar{T} - T_o)]ge_z, \tag{2.21}$$

$$\frac{\partial^2 \bar{T}}{\partial z^2} = 0. \tag{2.22}$$

Linear vertical temperature distribution in the fluid layer is obtained by (2.22) as:

$$\bar{T}(z) = T_o + \frac{\Delta T}{2}\left(1 - \frac{z}{d/2}\right) \tag{2.23}$$

13

where $\Delta T = T_1 - T_o$ in which T_1 is the bottom plate temperature, whereas T_o is the upper plate temperature. Substitution of the expressions (2.16-2.19), (2.23), into (2.2), (2.4), (2.8), (2.9) and (2.14) gives the equations of motion:

$$\nabla \cdot \mathbf{u}' = 0, \tag{2.24}$$

$$\frac{\partial \mathbf{u}'}{\partial t} = -(\mathbf{u}' \cdot \nabla)\mathbf{u}' - \frac{1}{\rho_o}\nabla\Pi' + \beta g \Theta' \mathbf{e}_z + \nu\nabla^2\mathbf{u}' + \frac{1}{\mu\rho_o}\left[B_o\mathbf{e}_B \cdot \nabla + \frac{\kappa}{\lambda}\mathbf{b}' \cdot \nabla\right]\frac{\kappa}{\lambda}\mathbf{b}', \tag{2.25}$$

$$\frac{\Theta'}{\partial t} + (\mathbf{u}' \cdot \nabla)\Theta' = w'\frac{\Delta T}{2} + \kappa\nabla^2\Theta', \tag{2.26}$$

$$\nabla \cdot \mathbf{b}' = 0, \tag{2.27}$$

$$\frac{1}{\lambda}\frac{\partial \mathbf{b}'}{\partial t} = -\frac{1}{\lambda}(\mathbf{u}' \cdot \nabla)\mathbf{b}' + \frac{1}{\lambda}\left[\frac{B_o\lambda}{\kappa}\mathbf{e}_B \cdot \nabla + \mathbf{b}' \cdot \nabla\right]\mathbf{u}' + \nabla^2\mathbf{b}', \tag{2.28}$$

where Π' is the stagnation pressure in dimensional form:

$$\Pi' = P' + \frac{\left|B_o\mathbf{e}_B \cdot \nabla + \frac{\kappa}{\lambda}\mathbf{b}'\right|^2}{2\mu}. \tag{2.29}$$

For the numerical analysis and implementation purposes, the above equations are expressed in non-dimensionalized form. The nondimensionalization is performed in accordance with [5] except for the length scale which is based on the half depth $d_h = \frac{1}{2}d$ for computational convenience. Therefore, the non-dimensionalized variables are stated as:

$$x = \frac{x}{d/2}, t = \frac{t}{d^2/4\kappa}, \mathbf{u} = \frac{\mathbf{u}'}{2\kappa/d}, \tag{2.30}$$

$$\Theta = \frac{\Theta'}{\Delta T}, \Pi = \frac{\Pi'}{4\rho_o\kappa^2/d^2}, \mathbf{b} = \frac{\mathbf{b}'}{B_o}. \tag{2.31}$$

The dimensionless form of governing equations can be written in the following form:

$$\nabla \cdot \mathbf{u} = 0, \tag{2.32}$$

$$\frac{\partial \mathbf{u}}{\partial t} = -(\mathbf{u} \cdot \nabla)\mathbf{u} - \nabla\Pi + PrRa_h\Theta\mathbf{e}_z + Pr\nabla^2\mathbf{u} + Q_hPr\left(Cos\chi\frac{\partial}{\partial y} + Sin\chi\frac{\partial}{\partial z}\right)\mathbf{b}, \tag{2.33}$$

$$\frac{\partial \Theta}{\partial t} + (\mathbf{u} \cdot \nabla)\Theta = \frac{w}{2} + \nabla^2\Theta, \tag{2.34}$$

$$\nabla \cdot \mathbf{b} = 0, \tag{2.35}$$

$$\nabla^2\mathbf{b} = -\left(Cos\chi\frac{\partial}{\partial y} + Sin\chi\frac{\partial}{\partial z}\right)\mathbf{u}, \tag{2.36}$$

where $\mathbf{b} = (b_x, b_y, b_z)$ is the induced magnetic vector field and Θ is the deviation from the linear conductive temperature profile. Since we are dealing with liquid metals, the limit of low magnetic Prandtl number $P_m = \nu/\lambda$ ($\kappa \ll \lambda$) is adopted in the governing equations. In

14

the limit $P_m \rightarrow 0$, some terms involving the induced magnetic field become negligible and the problem can be formulated in such a way that the induction equation (2.28) reduces to a quasi-steady relation (2.36). It is also noted that the term $Q_h Pr (\mathbf{e}_B \cdot \nabla) \mathbf{b}$ in (2.33) is obtained by introducing (2.19) to the Lorentz term $(\mathbf{J} \times \mathbf{B})$.

The resulting dimensionless numbers are the Rayleigh number $Ra(= 8Ra_h)$, Chandrasekhar number $Q(= 4Q_h)$ and Prandtl number Pr where

$$Ra = \frac{g \triangle T d^3 \alpha}{\kappa \nu}, \quad Q = \frac{B_0^2 d^2}{\rho \mu \nu \lambda}, \quad Pr = \frac{\nu}{\kappa}. \tag{2.37}$$

Here, Chandrasekhar number Q represent square of the Hartmann number $Ha = \sqrt{Q}$. Magnetic field in the dimensionless form becomes

$$\mathbf{B} = Cos\chi \mathbf{e}_y + Sin\chi \mathbf{e}_z + \frac{\kappa}{\lambda}\mathbf{b} \tag{2.38}$$

which indicates that the induced magnetic field $\mathbf{b}$ is weak compared to the externally imposed uniform magnetic field B_0 under the limit of low P_m. Thus $\mathbf{b}$ can be viewed as a slaved variable prescribed by the velocity field as stated by the quasi-steady relationship (2.36). Liquid metals or melts are characterized by this limit.

2.1.1 Boundary Conditions

The fluid is confined between two perfectly conducting plates at $z = -1$ and $z = 1$ at constant temperatures in the vertical z direction. Due to the nature of the boundary the vertical component of velocity is zero at these bounding plates, that is:

$$w = 0 \quad \text{at} \quad z = \pm 1. \tag{2.39}$$

Further, the temperature perturbations Θ, which is shown in Figure 2.3, is zero at these boundaries:

$$\Theta = 0 \quad \text{at} \quad z = \pm 1. \tag{2.40}$$

Since the bounding surfaces are rigid, no slip occurs at the fluid-walls interface. Therefore the horizontal components of the velocity u and v both vanish at the boundary. Thus,

$$\mathbf{u} = 0 \quad \text{and} \quad \Theta = 0 \quad at \quad z = \pm 1. \tag{2.41}$$

15
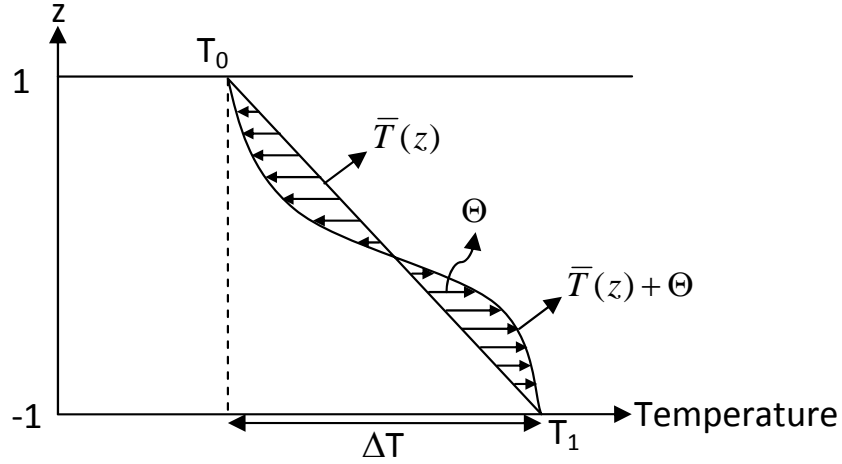
Figure 2.3: Profiles of the conductive temperature, $\bar{T}(z)$ and temperature perturbations, Θ in z direction.

The electromagnetic boundary conditions depend upon the electric properties of the medium adjoining the fluids. Since the walls are perfectly conducting, currents may cross the interface between fluid and the wall. However, due to the rigidity of the boundary, the horizontal components ($\mathbf{J}_x = 0$ and $\mathbf{J}_y = 0$) of the current vanish at the boundary. By using charge conservation equations ($\nabla \cdot \mathbf{J} = 0$) and $\mathbf{J}_x = 0$ and $\mathbf{J}_y = 0$ on the plane boundary, we conclude that

$$\frac{\partial \mathbf{J}_z}{\partial z} = 0 \quad \text{at} \quad z = \pm 1. \tag{2.42}$$

By using the Ampére's law, ($\nabla \times \mathbf{B} = \mu \mathbf{J}$) and magnetic conservation equations, ($\nabla \cdot \mathbf{B} = 0$) this relation becomes,

$$\frac{\partial \mathbf{b}}{\partial n} = 0. \tag{2.43}$$

Therefore, electrically high conductive boundary conditions for the induced magnetic field, are,

$$\frac{\partial b_x}{\partial z} = \frac{\partial b_y}{\partial z} = b_z = 0 \quad \text{at} \quad z = \pm 1. \tag{2.44}$$

We assume that the flow takes place in a doubly periodic three-dimensional rectangular region as in Figure 2.1 with aspect ratio $s_x \times s_y \times 2$ or $\Gamma \left[\frac{1}{2} s_x : \frac{1}{2} s_y \right]$ such that

$$0 \leq x \leq s_x, \quad 0 \leq y \leq s_y, \quad -1 \leq z \leq 1, \tag{2.45}$$

where $s_x = L_x/d_h$ and $s_y = L_y/d_h$ are the dimensionless periods in the horizontal x and y directions, respectively. Therefore, the periodic boundary conditions are defined for all the physical variables $\mathbf{u}$, Θ and $\mathbf{b}$ in the horizontal directions, that are:

$$\mathbf{u}(x + ms_x, y + ns_y, z, t) = \mathbf{u}(x, y, z, t), \tag{2.46}$$

$$\Theta(x + ms_x, y + ns_y, z, t) = \Theta(x, y, z, t), \tag{2.47}$$

$$\mathbf{b}(x + ms_x, y + ns_y, z, t) = \mathbf{b}(x, y, z, t). \tag{2.48}$$

where m and n are integers.

CHAPTER 3

SOLENOIDAL BASES

In modeling incompressible flow, the flow field is restricted to satisfy the divergence-free condition or the continuity equation, which is an important handicap to be overcome in order to get high accuracy and robust results in the numerical simulation studies. For this purpose, various techniques have been employed in literature such as the fractional step [21], the influence matrix [22] and the staggered grid [24] methods. In another study [48], pressure variable is expressed in terms of Legendre polynomials in a variational setting. The common focus in these techniques is to numerically treat the pressure variable which usually comes without any boundary conditions and whose role is to enforce the divergence-free condition on the flow. On the other hand, these techniques help to enforce the divergence-free condition only to a certain limited degree of accuracy. Further, the numerical simulation undertaken in this work involves a magnetic field variable which requires to satisfy an additional divergence-free condition. Thus, as an alternative, solenoidal (divergence-free) basis functions are used to expand the solenoidal variables in this study. By introducing expansions in terms of solenoidal bases functions for the velocity and the magnetic fields into the model equations in a Galerkin projection, both divergence-free criteria are exactly satisfied and the pressure variable is completely eliminated, so the number of equations and the number of flow variables are reduced. This reduces the burden on the numerical technique and increases the accuracy with which the divergence-free conditions are satisfied.

In this study, while the velocity solenoidal basis functions are generated independently, the quasi-steady relationship (2.36) between the velocity and the magnetic field variables is used to generate the corresponding magnetic solenoidal basis functions. This is a crucial step in this approach. The solenoidal basis functions are based on the Legendre polynomials in the vertical z-direction which are so constructed to satisfy the boundary conditions. Therefore,

the velocity and the magnetic fields can directly be expanded in terms of the solenoidal bases in the following way:

$$\hat{\mathbf{u}}(m, n, z, t) = \sum_{p=0}^{M} a_p^{(1)}(t)\mathbf{V}_p^{(1)}(z) + a_p^{(2)}(t)\mathbf{V}_p^{(2)}(z), \tag{3.1}$$

$$\hat{\mathbf{b}}(m, n, z, t) = \sum_{p=0}^{M} a_p^{(1)}(t)\mathbf{B}_p^{(1)}(z) + a_p^{(2)}(t)\mathbf{B}_p^{(2)}(z), \tag{3.2}$$

where $\mathbf{V}_p^{(1,2)}(\mathbf{z})$ and $\mathbf{B}_p^{(1,2)}(\mathbf{z})$ are the solenoidal basis for velocity and magnetic fields, respectively. The velocity and magnetic fields share the same time evolution as dictated by the quasi-steady relation (2.36).

3.1   Construction of Solenoidal Bases

3.1.1   Velocity Bases

The velocity basis functions are constructed to satisfy the continuity equation, (2.32), and the boundary conditions (2.41) so that the number of equations to be solved is reduced in this manner. At the outset, the solenoidal basis functions $\mathbf{V}_p(\mathbf{x})$ are required to satisfy

$$\nabla \cdot \mathbf{V}_p = 0, \quad \mathbf{V}_p(\mathbf{x})\,|_{z=\pm 1} = \mathbf{0}. \tag{3.3}$$

The assumption of periodicity in the horizontal directions allows the use of Fourier representation

$$\mathbf{V}_p(\mathbf{x}) = \mathbf{V}_p(z)exp(i\xi_m x + i\eta_n y) \tag{3.4}$$

and reduces the continuity equation to the form

$$i\xi_m U + i\eta_n V + \mathbb{D}W = 0 \tag{3.5}$$

where $\mathbf{V}(z) = (U, V, W)$ and $\mathbb{D} = \frac{d}{dz}$ is the differentiation operator. It turns out that the basis functions come in pairs $\mathbf{V}_p^{(j)}(\mathbf{x})$, $j = 1, 2$ because the continuity equation reduces the degree of freedom in selecting the components of $\mathbf{V}_p(\mathbf{x})$ to two by connecting the three components together. A typical set of solenoidal basis functions are then:

<u>CASE 1:</u>

$$\xi_m \neq 0 \quad \text{and} \quad \eta_n = 0 \quad \rightarrow \quad i\xi_m \hat{u} + \mathbb{D}\hat{w} = 0$$

$$\mathbf{V}_p^{(1)}(z) = \begin{bmatrix} 0 \\ isign(\xi_m)g(z) \\ 0 \end{bmatrix}, \quad \mathbf{V}_p^{(2)}(z) = \begin{bmatrix} isign(\xi_m)\mathbb{D}h(z) \\ 0 \\ |\xi_m|h(z) \end{bmatrix} \tag{3.6}$$

CASE 2:

$$\xi_m = 0 \quad \text{and} \quad \eta_n \neq 0 \quad \rightarrow \quad i\eta_n\hat{v} + \mathbb{D}\hat{w} = 0$$

$$\mathbf{V}_p^{(1)}(z) = \begin{bmatrix} isign(\eta_n)g(z) \\ 0 \\ 0 \end{bmatrix}, \quad \mathbf{V}_p^{(2)}(z) = \begin{bmatrix} 0 \\ isign(\eta_n)\mathbb{D}h(z) \\ |\eta_n|h(z) \end{bmatrix} \tag{3.7}$$

CASE 3:

$$\xi_m = 0 \quad \text{and} \quad \eta_n = 0 \quad \rightarrow \quad \mathbb{D}\hat{w} = 0$$

$$\mathbf{V}_p^{(1)}(z) = \begin{bmatrix} -g(z) \\ 0 \\ 0 \end{bmatrix}, \quad \mathbf{V}_p^{(2)}(z) = \begin{bmatrix} 0 \\ g(z) \\ 0 \end{bmatrix} \tag{3.8}$$

CASE 4:

$$\xi_m \neq 0 \quad \text{and} \quad \eta_n \neq 0 \quad \rightarrow \quad i\xi_m\hat{u} + i\eta_n\hat{v} + \mathbb{D}\hat{w} = 0$$

$$\mathbf{V}_p^{(1)}(z) = \begin{bmatrix} -(\eta_n/\xi_m)g(z) \\ g(z) \\ 0 \end{bmatrix}, \quad \mathbf{V}_p^{(2)}(z) = \begin{bmatrix} (i/\xi_m)\mathbb{D}h(z) \\ 0 \\ h(z) \end{bmatrix} \tag{3.9}$$

These bases have to satisfy the no-slip boundary conditions therefore it can be written as:

$$g(\pm 1) = h(\pm 1) = \mathbb{D}h(\pm 1) = 0. \tag{3.10}$$

Then, functions, $g(z)$ and $h(z)$ can be constructed as $g(z) = (1 - z^2)L_p(z)$ and $h(z) = (1 - z^2)^2 L_p(z)$ where $L_p(z)$ denotes Legendre polynomial of order p.

In all four cases, base pairs meet the divergence condition and the boundary conditions, and also for computational convenience all of them fulfill the condition of pairwise orthogonality $\mathbf{V}^{(1)} \cdot \mathbf{V}^{(2)} = 0$ except for Case 4. Therefore, by using Gram Schmidt orthogonality procedure, the base pairs for Case 4 can be rebuilt-up as follows:

$$
\mathbf{V}_p^{(1)}(z) = \begin{bmatrix} \dfrac{-i sign(\xi_m \eta_n)\eta_n g(z)}{\gamma} \\ \dfrac{i sign(\xi_m \eta_n)\xi_m g(z)}{\gamma} \\ 0 \end{bmatrix}, \quad \mathbf{V}_p^{(2)}(z) = \begin{bmatrix} \dfrac{i\xi_m \mathbb{D}h(z)}{\gamma} \\ \dfrac{i\eta_n \mathbb{D}h(z)}{\gamma} \\ \gamma h(z) \end{bmatrix} \tag{3.11}
$$

where $\gamma^2 = \xi_m^2 + \eta_n^2$. The solenoidal bases can further be characterized as $\mathbf{V}^{(1)}$ having the toroidal nature with vanishing vertical component $\mathbf{V}^{(1)} \cdot \mathbf{e}_z = 0$ and $\mathbf{V}^{(2)}$ having the poloidal nature with vanishing vertical vorticity component $\left(\nabla \times \mathbf{V}^{(2)}\right) \cdot \mathbf{e}_z = 0$.

For the subsequent Galerkin projection procedure, dual bases $\bar{\mathbf{V}}_p^{(j)}(\mathbf{x})$ need to be constructed to satisfy

$$
\nabla \cdot \bar{\mathbf{V}}_p^{(j)} = 0, \quad \bar{\mathbf{V}}_p^{(j)} \cdot \mathbf{e}_z \big|_{z=\pm 1} = 0. \tag{3.12}
$$

These requirements on the dual basis causes the elimination of the pressure term $\left(\bar{V}, \nabla p\right)$ in the projection procedure under the inner product:

$$
\left(\bar{V}, \nabla p\right) = \iiint_\Omega \bar{V} \cdot \nabla p \, d\Omega = \iiint_\Omega \nabla \cdot \left(p\bar{V}\right) d\Omega - \iiint_\Omega p \nabla \cdot \bar{V} \, d\Omega \tag{3.13}
$$

since dual basis, $\bar{\mathbf{V}}$ solenoidal, the second term on the right hand side

$$
\iiint_\Omega p \nabla \cdot \bar{V} d\Omega = 0 \tag{3.14}
$$

and by Gauss's theorem, the first term can be converted to a surface integral to get:

$$
\left(\bar{V}, \nabla p\right) = \iint_s p\bar{V} \cdot n \, dS. \tag{3.15}
$$

Under the condition $\bar{\mathbf{V}}_p^{(j)} \cdot \mathbf{e}_z \big|_{z=\pm 1} = 0$, (3.15) becomes zero. Therefore, the pressure term under the Galerkin projection drops from the momentum equation.

$$
\left(\bar{V}, \nabla p\right) = 0 \tag{3.16}
$$

Thus, dual basis can be set up under the conditions (3.12) as follows:

CASE 1:

$$\xi_m \neq 0 \quad \text{and} \quad \eta_n = 0 \quad \rightarrow \quad i\xi_m \hat{u} + \mathbb{D}\hat{w} = 0$$

$$\bar{\mathbf{V}}_q^{(1)}(z) = \begin{bmatrix} 0 \\ isign(\xi_m)f(z) \\ 0 \end{bmatrix}, \quad \bar{\mathbf{V}}_q^{(2)}(z) = \begin{bmatrix} isign(\xi_m)\mathbb{D}g(z) \\ 0 \\ |\xi_m|g(z) \end{bmatrix} \qquad (3.17)$$

CASE 2:

$$\xi_m = 0 \quad \text{and} \quad \eta_n \neq 0 \quad \rightarrow \quad i\eta_n \hat{v} + \mathbb{D}\hat{w} = 0$$

$$\bar{\mathbf{V}}_q^{(1)}(z) = \begin{bmatrix} isign(\eta_n)f(z) \\ 0 \\ 0 \end{bmatrix}, \quad \bar{\mathbf{V}}_q^{(2)}(z) = \begin{bmatrix} 0 \\ isign(\eta_n)\mathbb{D}g(z) \\ |\eta_n|g(z) \end{bmatrix} \qquad (3.18)$$

CASE 3:

$$\xi_m = 0 \quad \text{and} \quad \eta_n = 0 \quad \rightarrow \quad \mathbb{D}\hat{w} = 0$$

$$\bar{\mathbf{V}}_q^{(1)}(z) = \begin{bmatrix} -f(z) \\ 0 \\ 0 \end{bmatrix}, \quad \bar{\mathbf{V}}_q^{(2)}(z) = \begin{bmatrix} 0 \\ f(z) \\ 0 \end{bmatrix} \qquad (3.19)$$

CASE 4:

$$\xi_m \neq 0 \quad \text{and} \quad \eta_n \neq 0 \quad \rightarrow \quad i\xi_m \hat{u} + i\eta_n \hat{v} + \mathbb{D}\hat{w} = 0$$

$$\bar{\mathbf{V}}_q^{(1)}(z) = \begin{bmatrix} -(\eta_n/\xi_m)f(z) \\ f(z) \\ 0 \end{bmatrix}, \quad \bar{\mathbf{V}}_q^{(2)}(z) = \begin{bmatrix} (i/\xi_m)\mathbb{D}g(z) \\ 0 \\ g(z) \end{bmatrix} \qquad (3.20)$$

The dual bases need to satisfy the no-flux boundary condition in (3.12), therefore the functions, $f(z)$ and $g(z)$ can be constructed as $f(z) = L_q(z)$ and $g(z) = (1 - z^2)L_q(z)$ where $L_q(z)$ denotes Legendre polynomials of order q. Gram Schmidt orthogonality procedure again is used to reformulate the dual bases pairs for Case 4:

$$\bar{\mathbf{V}}_q^{(1)}(z) = \begin{bmatrix} \frac{-isign(\xi_m\eta_n)\eta_n g(z)}{k} \\ \frac{isign(\xi_m\eta_n)\xi_m g(z)}{k} \\ 0 \end{bmatrix}, \quad \bar{\mathbf{V}}_q^{(2)}(z) = \begin{bmatrix} \frac{i\xi_m \mathbb{D}h(z)}{k} \\ \frac{i\eta_n \mathbb{D}h(z)}{k} \\ kh(z) \end{bmatrix} \tag{3.21}$$

For the numerical evaluation of the inner product integrals arising in the projection procedure, Gauss-Legendre-Lobatto (GLL) quadrature is used

$$(\mathbf{f}, \mathbf{g}) = \int_{-1}^{1} \mathbf{f}^*(z) \cdot \mathbf{g}(z)\, dz \approx \sum_{j=0}^{N_z} w_q \mathbf{f}^*(z_q) \cdot \mathbf{g}(z_q) \tag{3.22}$$

where (w_q, z_q) are GLL quadrature weights and nodes, respectively. For linear terms, it can be shown that associated with the GLL quadrature rules, the number of quadrature nodes N_z and the number of solenoidal basis M should be related in the least by $N_z = M + 4$ in order to render the numerical quadrature exact.

With the inclusion of the nonlinear terms, $V_p^{(1,2)}(z) \in P_{M+4}$ and $\bar{V}_q^{(1,2)}(z) \in P_{M+2}$, thus the Gaussian quadrature yields exact results for nonlinear terms if

$$2N_z - 1 \geq (M + 3) + (M + 4) + (M + 2) = 3M + 9 \rightarrow N_z \geq (3M + 10)/2. \tag{3.23}$$

3.1.2 Magnetic Bases

Magnetic solenoidal basis functions are generated by using the quasi-steady relationship, (2.36), between the velocity and the magnetic field variables. These magnetic bases are analytically solved by using quasi-steady relation and solution procedure was shown in Appendix A.

3.1.2.1 Magnetic bases for the oblique case

The induced magnetic field $\mathbf{b}$ is prescribed by the velocity field as stated by the quasi-steady relationship as follows:

$$\nabla^2 \mathbf{b} = -(\mathbf{e}_B \cdot \nabla)\mathbf{u}, \tag{3.24}$$

where $\mathbf{e}_B$ shows the direction of the obliquely imposed magnetic field. Substitution of Fourier series expansion for the velocity and magnetic field variables into this equation yields the boundary value problem:

$$\left[\frac{d^2}{dz^2} - \gamma^2\right]\hat{\mathbf{b}}(m, n, z, t) = \left[Cos\chi\eta_m i + Sin\chi\frac{d}{dz}\right]\hat{\mathbf{u}}(m, n, z, t) \tag{3.25}$$

to be solved subject to the boundary conditions

$$\frac{db_x}{dz} = \frac{db_y}{dz} = b_z = 0 \quad \text{at} \quad z = \pm 1. \tag{3.26}$$

where $\gamma^2 = \xi_m^2 + \eta_n^2$. The singularity in the equations for b_x and b_y at $\xi_m = \eta_n = 0$ due to the homogeneous Neumann boundary conditions is removed by setting

$$b_x(z = 0) = b_y(z = 0) = 0 \tag{3.27}$$

without loss of generality. Solenoidal basis

$$\mathbf{B}(\mathbf{x}) = \mathbf{B}(z)exp(i\xi_m x + i\eta_n y) \tag{3.28}$$

for the magnetic field is constructed by solving

$$\mathbb{D}^2\mathbf{B} - \gamma^2\mathbf{B} = -\left[Cos\chi\eta_m i + Sin\chi\mathbb{D}\right]\mathbf{V}, \tag{3.29}$$

for $\mathbf{B}(z)$ subject to the boundary conditions

$$\mathbb{D}B_x = \mathbb{D}B_y = B_z = 0 \quad \text{at} \quad z = \pm 1. \tag{3.30}$$

and for each $\mathbf{V} = \mathbf{V}_p^{(j)}(z)$ where $\mathbf{B}(z) = (B_x, B_y, B_z)$.

3.1.2.2   Magnetic bases for the vertical case

In this case, the magnetic field applied in the vertical direction, in other words, the angle in the yz plane is taken as $\chi = \pi/2$, so that;

$$\mathbf{e}_B = Cos\left(\frac{\pi}{2}\right)\mathbf{e}_y + Sin\left(\frac{\pi}{2}\right)\mathbf{e}_z = \mathbf{e}_z. \tag{3.31}$$

The induced magnetic field $\mathbf{b}$ is prescribed by the velocity field as stated by the quasi-steady relationship as follows:

$$\nabla^2\mathbf{b} = -(\mathbf{e}_z \cdot \nabla)\mathbf{u}, \tag{3.32}$$

where $\mathbf{e}_z$ direction vector opposite to gravity. Substitution of Fourier series expansion for the velocity and magnetic field variables into this equation yields the boundary value problem:

$$\left[\frac{d^2}{dz^2} - \gamma^2\right]\hat{\mathbf{b}}(m, n, z, t) = -\left[\frac{d}{dz}\right]\hat{\mathbf{u}}(m, n, z, t) \tag{3.33}$$

to be solved subject to the boundary conditions

$$\frac{db_x}{dz} = \frac{db_y}{dz} = b_z = 0 \quad \text{at} \quad z = \pm 1. \tag{3.34}$$

where $\gamma^2 = \xi_m^2 + \eta_n^2$. The singularity in the equations for b_x and b_y at $\xi_m = \eta_n = 0$ due to the homogeneous Neumann boundary conditions is again removed by setting

$$b_x(z = 0) = b_y(z = 0) = 0 \tag{3.35}$$

without loss of generality. Solenoidal basis (3.28) for the magnetic field is constructed by solving

$$\mathbb{D}^2\mathbf{B} - \gamma^2\mathbf{B} = -\mathbb{D}\mathbf{V}, \tag{3.36}$$

for $\mathbf{B}(z)$ subject to the boundary conditions (3.30).

3.1.2.3 Magnetic bases for the horizontal case

In this case, the magnetic field applied in the horizontal direction, in other words, the angle in yz plane becomes $\chi = 0$ so that;

$$\mathbf{e}_B = Cos(0)\mathbf{e}_y + Sin(0)\mathbf{e}_z = \mathbf{e}_y. \tag{3.37}$$

The induced magnetic field $\mathbf{b}$ is prescribed by the velocity field as stated by the quasi-steady relationship as follows:

$$\nabla^2\mathbf{b} = -(\mathbf{e}_y \cdot \nabla)\mathbf{u}, \tag{3.38}$$

where $\mathbf{e}_y$ direction vector in y direction. Substitution of Fourier series expansion for the velocity and magnetic field variables into this equation yields the boundary value problem:

$$\left[\frac{d^2}{dz^2} - \gamma^2\right]\hat{\mathbf{b}}(m, n, z, t) = -\eta_m i\hat{\mathbf{u}}(m, n, z, t) \tag{3.39}$$

to be solved subject to the boundary conditions

$$\frac{db_x}{dz} = \frac{db_y}{dz} = b_z = 0 \quad \text{at} \quad z = \pm 1. \tag{3.40}$$

25

where $\gamma^2 = \xi_m^2 + \eta_n^2$. The singularity in the equations for b_x and b_y at $\xi_m = \eta_n = 0$ due to the homogeneous Neumann boundary conditions is again removed by setting

$$b_x(z = 0) = b_y(z = 0) = 0 \qquad (3.41)$$

without loss of generality. Solenoidal basis (3.28) for the magnetic field is constructed by solving

$$\mathbb{D}^2\mathbf{B} - \gamma^2\mathbf{B} = -\eta_m i\mathbf{V}, \qquad (3.42)$$

for $\mathbf{B}(z)$ subject to the boundary conditions (3.30).

3.2   Construction of Thermal Bases

The thermal bases are solely required to satisfy the boundary conditions. Thus, the expansion for the thermal field becomes

$$\hat{\Theta}(m, n, z, t) = \sum_{p=0}^{M} b_p(t)T_p(z), \qquad (3.43)$$

where $T_p(z) = (1 - z^2)L_p(z)$. The dual basis simply becomes $\bar{T}_q(z) = T_p(z)$.

After the substitution of the flow variables expanded in terms of the constructed basis functions into the model equations and projecting the model system of equations onto the space spanned by the dual bases in a Galerkin procedure, the resulting system of equations governing the evolution of the time dependent expansion coefficients $a_p^{(j)}(t)$ and $b_p(t)$ is numerically integrated in time.

CHAPTER 4

WEAK FORMULATION OF EQUATIONS

In this work of numerical simulations of thermal convection under the influence of a constant magnetic field, the governing partial differential equations are projected onto the dual space by Galerkin projection first to get the weak form of the equations in the form of ordinary differential equations goevrning the time evolution of the expansion coefficients. In this procedure, the representations of the flow variables and the dual space are formed by truncated expansion in terms of the basis functions as constructed in the previous chapter.

Equations from (2.32) to (2.36) are projected by Galerkin projection procedure, which employs the "error distribution principle" that the residue should be small. Since the velocity solenoidal bases are constructed by using the continuity equation and boundary conditions, and the corresponding magnetic bases are constructed by using quasi-steady relation from the velocity solenoidal bases, the equations (2.32), (2.35) and (2.36) are satisfied automatically. Thus, the number of equations in the model system drops from nine to four equations, which are the momentum and the energy equations. The residue of these equations can be written in the following form:

$$R_{\mathbf{u}} = -\frac{\partial \mathbf{u}}{\partial t} - (\mathbf{u} \cdot \nabla)\,\mathbf{u} - \nabla\Pi + PrRa_h\Theta\mathbf{e}_z + Pr\nabla^2\mathbf{u} + Q_hPr\left(Cos\chi\partial y + Sin\chi\partial z\right)\mathbf{b}, \qquad (4.1)$$

$$R_{\Theta} = -\frac{\partial \Theta}{\partial t} - (\mathbf{u} \cdot \nabla)\,\Theta - \frac{w}{2} + \nabla^2\Theta, \qquad (4.2)$$

after the substitution of the flow variables:

$$\mathbf{u}(m,n,z,t) = \sum_{|m|\leq N_x/2}\sum_{|n|\leq N_y/2} e^{(i\xi_m x + i\eta_n y)} \sum_{p=0}^{M} a_p^{(1)}(t)\mathbf{V}_p^{(1)}(z) + a_p^{(2)}(t)\mathbf{V}_p^{(2)}(z), \tag{4.3}$$

$$\mathbf{b}(m,n,z,t) = \sum_{|m|\leq N_x/2}\sum_{|n|\leq N_y/2} e^{(i\xi_m x + i\eta_n y)} \sum_{p=0}^{M} a_p^{(1)}(t)\mathbf{B}_p^{(1)}(z) + a_p^{(2)}(t)\mathbf{B}_p^{(2)}(z), \tag{4.4}$$

$$\Theta(m,n,z,t) = \sum_{|m|\leq N_x/2}\sum_{|n|\leq N_y/2} e^{(i\xi_m x + i\eta_n y)} \sum_{p=0}^{M} b_p(t)T_p(z), \tag{4.5}$$

represented in terms of the solenoidal velocity $\mathbf{V}_p^{(1,2)}(\mathbf{z})$, the solenoidal magnetic $\mathbf{B}_p^{(1,2)}(\mathbf{z})$ and the thermal $T_p(\mathbf{z})$ basis functions where $\partial y = \partial/\partial y$ and $\partial z = \partial/\partial z$. Due to the quasi-steady relation, the velocity and the magnetic fields share the same time coefficients, $a_p^{(1)}(t)$ and $a_p^{(2)}(t)$.

The Galerkin scheme is formulated by introducing (4.3), (4.4) and (4.5) into (4.1) and (4.2) and projecting onto the dual space spanned by the dual bases $\bar{V}_p^{(1)}$, $\bar{V}_p^{(2)}$ and $\bar{T}_p$ to get

$$\int_0^{L_x}\int_0^{L_y}\int_{-1}^{1} \bar{V}\cdot R_{\mathbf{u}}\,dz = \int_0^{L_x}\int_0^{L_y}\int_{-1}^{1} \bar{V}\cdot\left[-\frac{\partial\mathbf{u}}{\partial t} - (\mathbf{u}\cdot\nabla)\mathbf{u} - \nabla\Pi + PrRa_h\Theta e_z\right]dxdydz \;+$$

$$\int_0^{L_x}\int_0^{L_y}\int_{-1}^{1} \bar{V}\cdot\left[Pr\nabla^2\mathbf{u} + Q_hPr\left(Cos\chi\partial y + Sin\chi\partial z\right)\mathbf{b}\right]dxdydz = 0 \tag{4.6}$$

$$\int_0^{L_x}\int_0^{L_y}\int_{-1}^{1} \bar{T}R_\Theta\,dz = \int_0^{L_x}\int_0^{L_y}\int_{-1}^{1} \bar{T}\left[-\frac{\partial\Theta}{\partial t} - (\mathbf{u}\cdot\nabla)\Theta - \frac{w}{2} + \nabla^2\Theta\right]dxdydz = 0 \tag{4.7}$$

or in the matrix form,

$$\begin{bmatrix}\left(\bar{V}_q^{(1)},\hat{V}_p^{(1)}\right) & \left(\bar{V}_q^{(1)},V_p^{(2)}\right) \\ \left(\bar{V}_q^{(2)},V_p^{(1)}\right) & \left(\bar{V}_q^{(2)},V_p^{(2)}\right)\end{bmatrix}\begin{bmatrix}\dot{a}_p^{(1)} \\ \dot{a}_p^{(2)}\end{bmatrix} + \begin{bmatrix}c^{(1)} \\ c^{(2)}\end{bmatrix} = PrRa_h\begin{bmatrix}\left(\bar{V}_q^{(1)},T_p e_z\right) \\ \left(\bar{V}_q^{(2)},T_p e_z\right)\end{bmatrix}\begin{bmatrix}b_p\end{bmatrix}$$

$$+Pr\begin{bmatrix}\left(\bar{V}_q^{(1)},\nabla^2 V_p^{(1)}\right) & \left(\bar{V}_q^{(1)},\nabla^2 V_p^{(2)}\right) \\ \left(\bar{V}_q^{(2)},\nabla^2 V_p^{(1)}\right) & \left(\bar{V}_q^{(2)},\nabla^2 V_p^{(2)}\right)\end{bmatrix}\begin{bmatrix}a_p^{(1)} \\ a_p^{(2)}\end{bmatrix}$$

$$+PrQ_h\begin{bmatrix}\left(\bar{V}_q^{(1)},(Cos\chi\partial y + Sin\chi\partial z)B_p^{(1)}\right) & \left(\bar{V}_q^{(1)},(Cos\chi\partial y + Sin\chi\partial z)B_p^{(2)}\right) \\ \left(\bar{V}_q^{(2)},(Cos\chi\partial y + Sin\chi\partial z)B_p^{(1)}\right) & \left(\bar{V}_q^{(2)},(Cos\chi\partial y + Sin\chi\partial z)B_p^{(2)}\right)\end{bmatrix}\begin{bmatrix}a_p^{(1)} \\ a_p^{(2)}\end{bmatrix} \tag{4.8}$$

$$\left(\bar{T}_q, T_p\right)\dot{b}_p + d = \left(\bar{T}_q, V_p^{(1)} \cdot e_z\right)a_p^{(1)} + \left(\bar{T}_q, V_p^{(2)} \cdot e_z\right)a_p^{(2)} + \left(\bar{T}_q, \nabla^2 T_p\right)b_p \tag{4.9}$$

where

$$c^{1,2} = \left(\bar{V}, (\mathbf{u} \cdot \nabla)\mathbf{u}\right) = \int\limits_0^{L_x} \int\limits_0^{L_y} \int\limits_{-1}^{1} \left(\bar{V}^* (\mathbf{u} \cdot \nabla)\mathbf{u}\right) dxdydz \tag{4.10}$$

$$d = \left(\bar{T}, (\mathbf{u} \cdot \nabla)\Theta\right) = \int\limits_0^{L_x} \int\limits_0^{L_y} \int\limits_{-1}^{1} \left(\bar{T}^* (\mathbf{u} \cdot \nabla)\Theta\right) dxdydz \tag{4.11}$$

are the nonlinear terms.

The crucial point in this projection is that, the dual solenoidal bases (3.17), (3.18), (3.19) and (3.21) are chosen in such a way that the pressure term (3.16) drops from the system of equations. In addition, due to the structure of the solenoidal basis function $V_p^{(1)}$, the terms

$$V_p^{(1)} \cdot e_z = 0 \tag{4.12}$$

drop from the equation (4.9) and thus, the coefficients $a_p^{(1)}$ are absent in (4.9). Further, due to the construction of the solenoidal bases and their duals, cross terms between the bases and their duals vanish, therefore the system (4.8) and (4.9) reduce to:

$$\begin{bmatrix} \left(\bar{V}_q^{(1)}, \hat{V}_p^{(1)}\right) & 0 \\ 0 & \left(\bar{V}_q^{(2)}, V_p^{(2)}\right) \end{bmatrix} \begin{bmatrix} \dot{a}_p^{(1)} \\ \dot{a}_p^{(2)} \end{bmatrix} + \begin{bmatrix} c^{(1)} \\ c^{(2)} \end{bmatrix} = PrRa_h \begin{bmatrix} 0 \\ \left(\bar{V}_q^{(2)}, T_p e_z\right) \end{bmatrix} \begin{bmatrix} b_p \end{bmatrix}$$

$$+ Pr \begin{bmatrix} \left(\bar{V}_q^{(1)}, \nabla^2 V_p^{(1)}\right) & 0 \\ 0 & \left(\bar{V}_q^{(2)}, \nabla^2 V_p^{(2)}\right) \end{bmatrix} \begin{bmatrix} a_p^{(1)} \\ a_p^{(2)} \end{bmatrix}$$

$$+ PrQ_h \begin{bmatrix} \left(\bar{V}_q^{(1)}, (Cos\chi \partial y + Sin\chi \partial z) B_p^{(1)}\right) & 0 \\ 0 & \left(\bar{V}_q^{(2)}, (Cos\chi \partial y + Sin\chi \partial z) B_p^{(2)}\right) \end{bmatrix} \begin{bmatrix} a_p^{(1)} \\ a_p^{(2)} \end{bmatrix} \tag{4.13}$$

$$\left(\bar{T}_q, T_p\right)\dot{b}_p + d = \left(\bar{T}_q, V_p^{(2)} \cdot e_z\right)a_p^{(2)} + \left(\bar{T}_q, \nabla^2 T_p\right)b_p \tag{4.14}$$

If we combine (4.13) and (4.14) in a system and write it down in the matrix form, we get the Mass and Stiffness matrices as follows:

29

$$
\underbrace{\begin{bmatrix} \left(\bar{V}_q^{(1)}, V_p^{(1)}\right) & 0 & 0 \\ 0 & \left(\bar{V}_q^{(2)}, V_p^{(2)}\right) & 0 \\ 0 & 0 & \left(\bar{T}_q, T_p\right) \end{bmatrix}}_{Mass-Matrix} \begin{bmatrix} \dot{a}_p^{(1)} \\ \dot{a}_p^{(2)} \\ \dot{b}_p \end{bmatrix} + \begin{bmatrix} c^{(1)} \\ c^{(2)} \\ d \end{bmatrix} =
$$

$$
+Pr\underbrace{\begin{bmatrix} \left(\bar{V}_q^{(1)}, (-\gamma^2 + \mathbb{D}^2)V_p^{(1)}\right) & 0 & 0 \\ 0 & \left(\bar{V}_q^{(2)}, (-\gamma^2 + \mathbb{D}^2)V_p^{(2)}\right) & Ra_h\left(\bar{V}_q^{(2)}, T_p e_z\right) \\ 0 & \left(\bar{T}_q, V_p^{(2)} \cdot e_z\right)/2Pr & \left(\bar{T}_q, \nabla^2 T_p\right)/Pr \end{bmatrix}}_{Stiffness-Matrix} \begin{bmatrix} a_p^{(1)} \\ a_p^{(2)} \\ b_p \end{bmatrix}
$$

$$
+PrQ_h\underbrace{\begin{bmatrix} \left(\bar{V}_q^{(1)}, (Cos\chi\eta_m i + Sin\chi\mathbb{D})B_p^{(1)}\right) & 0 \\ 0 & \left(\bar{V}_q^{(2)}, (Cos\chi\eta_m i + Sin\chi\mathbb{D})B_p^{(2)}\right) \end{bmatrix}}_{Stiffness-Matrix} \begin{bmatrix} a_p^{(1)} \\ a_p^{(2)} \end{bmatrix} \tag{4.15}
$$

or in compact form:

$$
\underbrace{\begin{bmatrix} \left(\bar{V}_q^{(1)}, V_p^{(1)}\right) & 0 & 0 \\ 0 & \left(\bar{V}_q^{(2)}, V_p^{(2)}\right) & 0 \\ 0 & 0 & \left(\bar{T}_q, T_p\right) \end{bmatrix}}_{Mass-Matrix} \begin{bmatrix} \dot{a}_p^{(1)} \\ \dot{a}_p^{(2)} \\ \dot{b}_p \end{bmatrix} + \begin{bmatrix} c^{(1)} \\ c^{(2)} \\ d \end{bmatrix} =
$$

$$
Pr\underbrace{\begin{bmatrix} \begin{array}{l} \left(\bar{V}_q^{(1)}, (-\gamma^2 + \mathbb{D}^2)V_p^{(1)}\right)+ \\ \left(\bar{V}_q^{(1)}, Q_h (Cos\chi\eta_m i + Sin\chi\mathbb{D})B_p^{(1)}\right) \end{array} & 0 & 0 \\ 0 & \begin{array}{l} \left(\bar{V}_q^{(2)}, (-\gamma^2 + \mathbb{D}^2)V_p^{(2)}\right)+ \\ \left(\bar{V}_q^{(2)}, Q_h (Cos\chi\eta_m i + Sin\chi\mathbb{D})B_p^{(2)}\right) \end{array} & Ra_h\left(\bar{V}_q^{(2)}, T_p e_z\right) \\ 0 & \left(\bar{T}_q, V_p^{(2)} \cdot e_z\right)/2Pr & \left(\bar{T}_q, \nabla^2 T_p\right)/Pr \end{bmatrix}}_{Stiffness-Matrix} \begin{bmatrix} a_p^{(1)} \\ a_p^{(2)} \\ b_p \end{bmatrix}
$$

$$\tag{4.16}$$

where $\gamma^2 = \xi^2 + \eta^2$ and $\mathbb{D} = \frac{d}{dz}$.

4.1 Spatial Discretization

While Fourier expansions are used for the approximation of the variables in the horizontal directions, polynomial expansions are used for the approximations in the vertical direction.

The assumption of periodicity in the horizontal directions allows the use of Fourier series expansions of the dependent flow variables,

$$\mathbf{u}(x, y, z, t) = \sum_m \sum_n \hat{\mathbf{u}}(m, n, z, t) exp[i(\xi_m x + \eta_n y)], \tag{4.17}$$

$$\Theta(x, y, z, t) = \sum_m \sum_n \hat{\Theta}(m, n, z, t) exp[i(\xi_m x + \eta_n y)], \tag{4.18}$$

$$\mathbf{b}(x, y, z, t) = \sum_m \sum_n \hat{\mathbf{b}}(m, n, z, t) exp[i(\xi_m x + \eta_n y)], \tag{4.19}$$

where ξ_m and η_n are the wave numbers with

$$\xi_m = \frac{2\pi m}{s_x}, \tag{4.20}$$

$$\eta_n = \frac{2\pi n}{s_y} \tag{4.21}$$

for the integers m and n in the range

$$1 - \frac{1}{2}N_x \le m \le \frac{1}{2}N_x, \tag{4.22}$$

$$1 - \frac{1}{2}N_y \le n \le \frac{1}{2}N_y. \tag{4.23}$$

Here, N_x and N_y represent horizontal resolutions in x and y directions, respectively. The collocation points in the x and y directions are:

$$x_i = \frac{s_x i}{N_x}, \tag{4.24}$$

$$y_j = \frac{s_y j}{N_y}. \tag{4.25}$$

for $0 \le i \le N_x$ and $0 \le j \le N_y$.

Since the interval in the z direction is normalized to the range $[-1, 1]$, Gauss-Legendre-Lobatto (GLL) points are used as collocation points in the vertical direction. GLL points are found as roots of the polynomial

$$q(z) = (1 - z^2)\mathbb{D}L_{N_z}(z). \tag{4.26}$$

where $\mathbb{D} = \frac{d}{dz}$ and $L_{N_z}(z)$ is the Legendre polynomial of order N_z. The Legendre polynomials can be derived using the Rodrigues' formula:

$$L_{N_z}(z) = \frac{1}{2^{N_z} N_z!} \mathbb{D}^{N_z}(1 - z^2)^{N_z}. \tag{4.27}$$

The quadrature points consist of the boundary points $z_0 = -1$ and $z_{N_z} = 1$, and $N_z - 1$ interior points which are the roots of the Legendre polynomial $\mathbb{D}L_{N_z}(z)$. Unfortunately, no explicit

formulas are known for these interior roots, so Newton method is used in order to compute these roots numerically from recurrence relations for the Legendre polynomials.

Legendre polynomials satisfy some three term relations as a general property of Jacobi Polynomials. These relations are derived in [41] for Legendre polynomials as follows:

$$zL_{N_z}(z) = \frac{N_z}{2N_z + 1}L_{N_z-1}(z) + \frac{N_z + 1}{2N_z + 1}L_{N_z+1}(z), \tag{4.28}$$

$$L_{N_z}(z) = \frac{1}{2N_z + 1}\mathbb{D}L_{N_z+1}(z) - \frac{1}{2N_z + 1}\mathbb{D}L_{N_z-1}(z). \tag{4.29}$$

$$(1 - z^2)\mathbb{D}L_{N_z}(z) = \frac{N_z(N_z + 1)}{2N_z + 1}L_{N_z-1}(z) - \frac{N_z(N_z + 1)}{2N_z + 1}L_{N_z+1}(z). \tag{4.30}$$

A direct relationship for the GLL roots in terms of the Legendre polynomials can be obtained by substitution the relation (4.30) into the (4.26):

$$q(z) = \frac{N_z(N_z + 1)}{2N_z + 1}L_{N_z-1}(z) - \frac{N_z(N_z + 1)}{2N_z + 1}L_{N_z+1}(z). \tag{4.31}$$

The derivative of $q(z)$ can be written by taking the derivative of (4.31) to get:

$$\mathbb{D}q(z) = \frac{N_z(N_z + 1)}{2N_z + 1}\mathbb{D}L_{N_z-1}(z) - \frac{N_z(N_z + 1)}{2N_z + 1}\mathbb{D}L_{N_z+1}(z). \tag{4.32}$$

This can be written in the simple form by substituting (4.29) into (4.32) to get:

$$\mathbb{D}q(z) = -N_z(N_z + 1)L_{N_z}(z). \tag{4.33}$$

Now, the roots of the $q(z) = 0$ can be computed by using the Newton iterations

$$z_i^{n+1} = z_i^n - \frac{q(z_i^n)}{\mathbb{D}q(z_i^n)} = z_i^n - \frac{L_{N_z-1}(z) - L_{N_z+1}(z)}{(2N_z + 1)L_{N_z}(z)} \tag{4.34}$$

where Chebyshev points are used as initial guesses:

$$z_i^o = cos\left(\frac{i\pi}{N_z}\right) \quad for \quad 1 \leq i \leq N_z - 1. \tag{4.35}$$

The corresponding weights are given by:

$$w_i = \begin{cases} \frac{2}{N_z(N_z+1)} & \text{if } i = 0, N_z \\ \frac{2(L_{N_z}(z_i))^{-2}}{N_z(N_z+1)} & \text{if } i = 1, \ldots, N_z - 1. \end{cases} \tag{4.36}$$

4.2 Analysis of Solenoidal Bases

In this section, we present the solenoidal bases for a selected wavenumber pair (ξ_m, η_n) in order to study the structure of the bases. For this purpose, we choose $\xi_m = 1$ and $\eta_n = 1$

wavenumber pair, which is the one of the most energetic modes and exhibit dependence both on x and y variables. As mentioned in chapter 3 solenoidal basis functions come in pairs, ($\mathbf{V}^{(1,2)}$) for velocity and ($\mathbf{B}^{(1,2)}$) for magnetic fields. They can be classified as having toroidal ($\mathbf{V}^{(1)}, \mathbf{B}^{(1)}$) and poloidal ($\mathbf{V}^{(2)}, \mathbf{B}^{(2)}$) character. Each of the following figures shows the first, second and third components of the selected solenoidal basis in rows for velocity and the magnetic field with different angles χ.

As shown in Figure 4.1, the velocity solenoidal basis carries motion in all three directions with identical profiles for the first and second components corresponding to the horizontal directions since it represents a mode residing in the diagonal plane of the convective box. As mentioned before, the solenoidal magnetic basis is derived from the associated solenoidal velocity basis appearing as forcing in (2.38) in which the coefficient $Cos\chi$ weights y-variation and $Sin\chi$ weights z-variation of the velocity basis. When magnetic field is applied in the vertical direction $\chi = 90°$, z-variation weights the most and the rich vertical structure in the velocity basis is carried to the corresponding magnetic basis as shown in Figure 4.2. As the angle is reduced, y-variation begins to weight more and this is reflected in Figures 4.3 and 4.4 corresponding to the angles $\chi = 60°$ and $\chi = 30°$, respectively. In these cases, there is noticable change in the vertical profiles of the magnetic basis especially in the poloidal case as compared to that of the vertical angle.

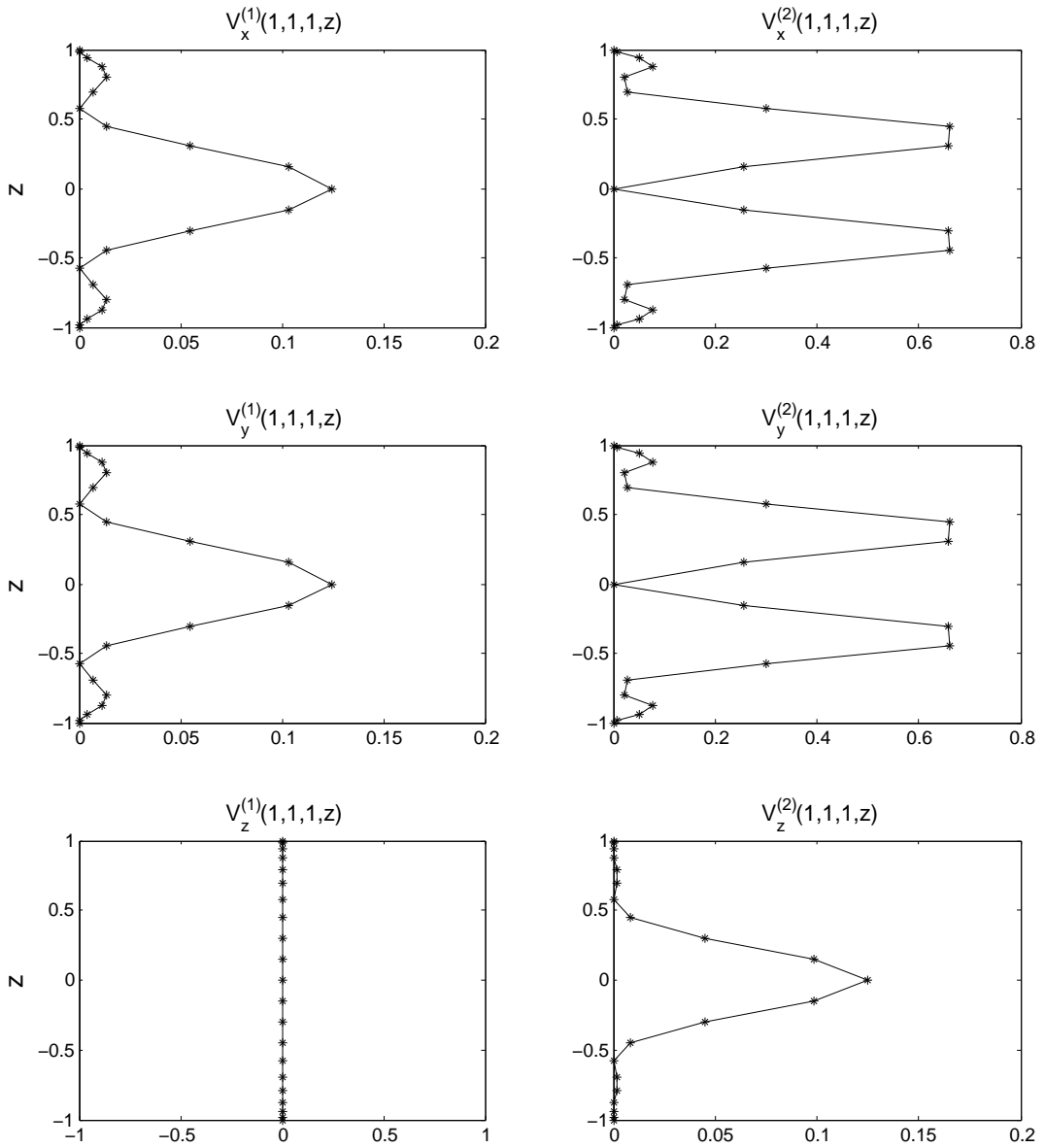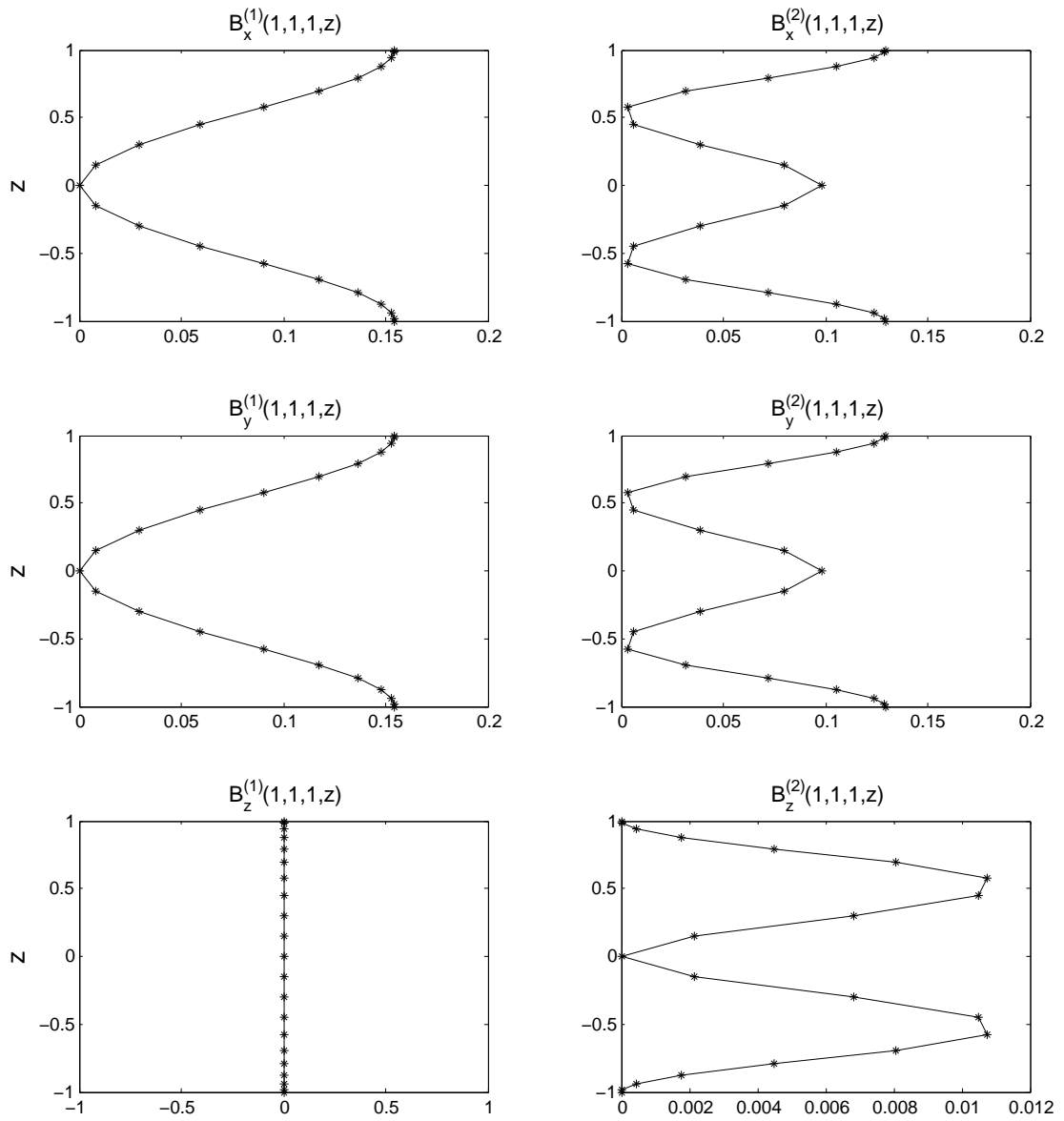Figure 4.1: Velocity solenoidal basis profile at $\xi_m = 1$ and $\eta_n = 1$ wavenumber pair.

Figure 4.2: Magnetic solenoidal basis profile at $\chi = 90°$, $\xi_m = 1$ and $\eta_n = 1$ wavenumber pair.
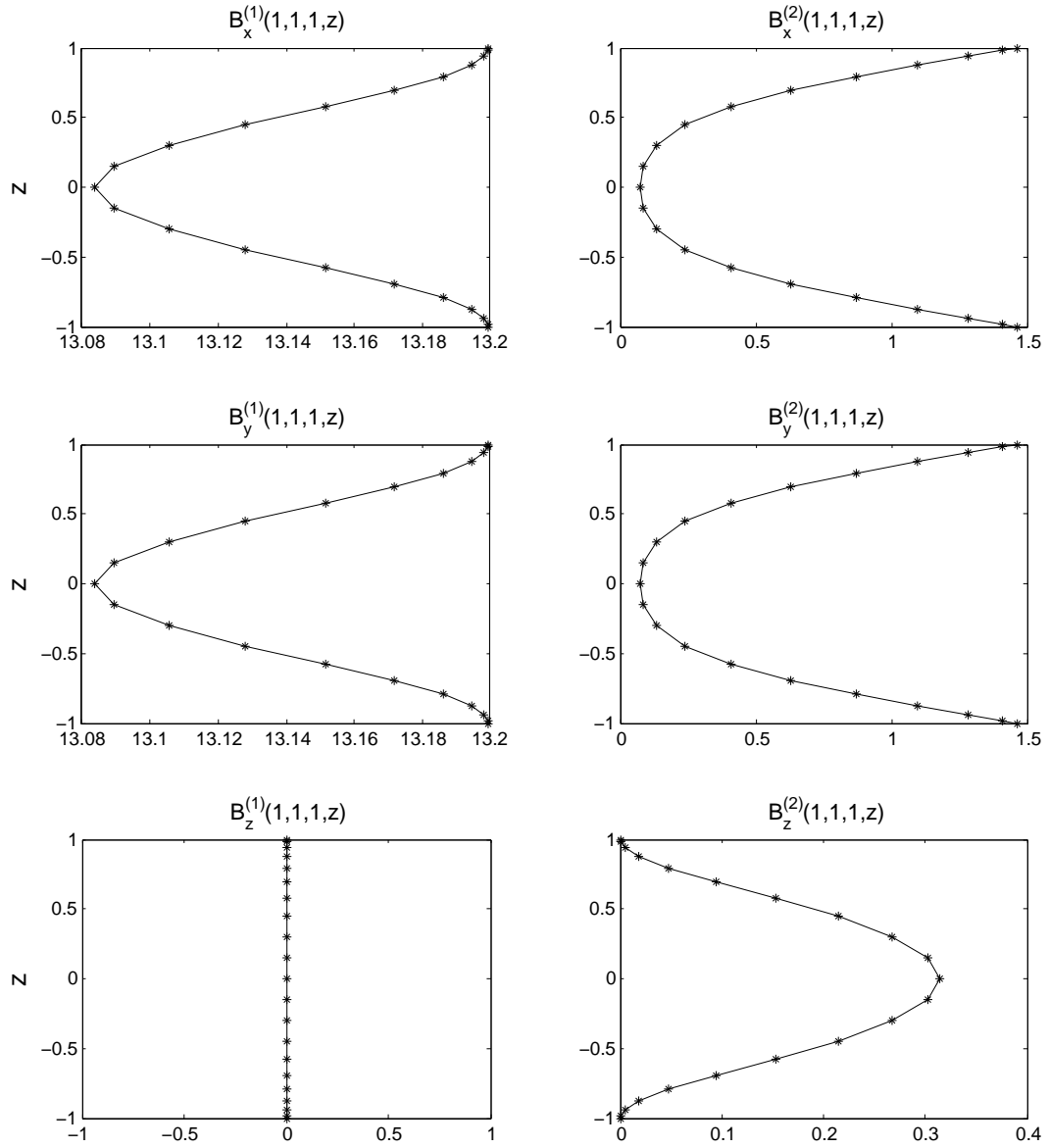
Figure 4.3: Magnetic solenoidal basis profile at $\chi = 60°$, $\xi_m = 1$ and $\eta_n = 1$ wavenumber pair.
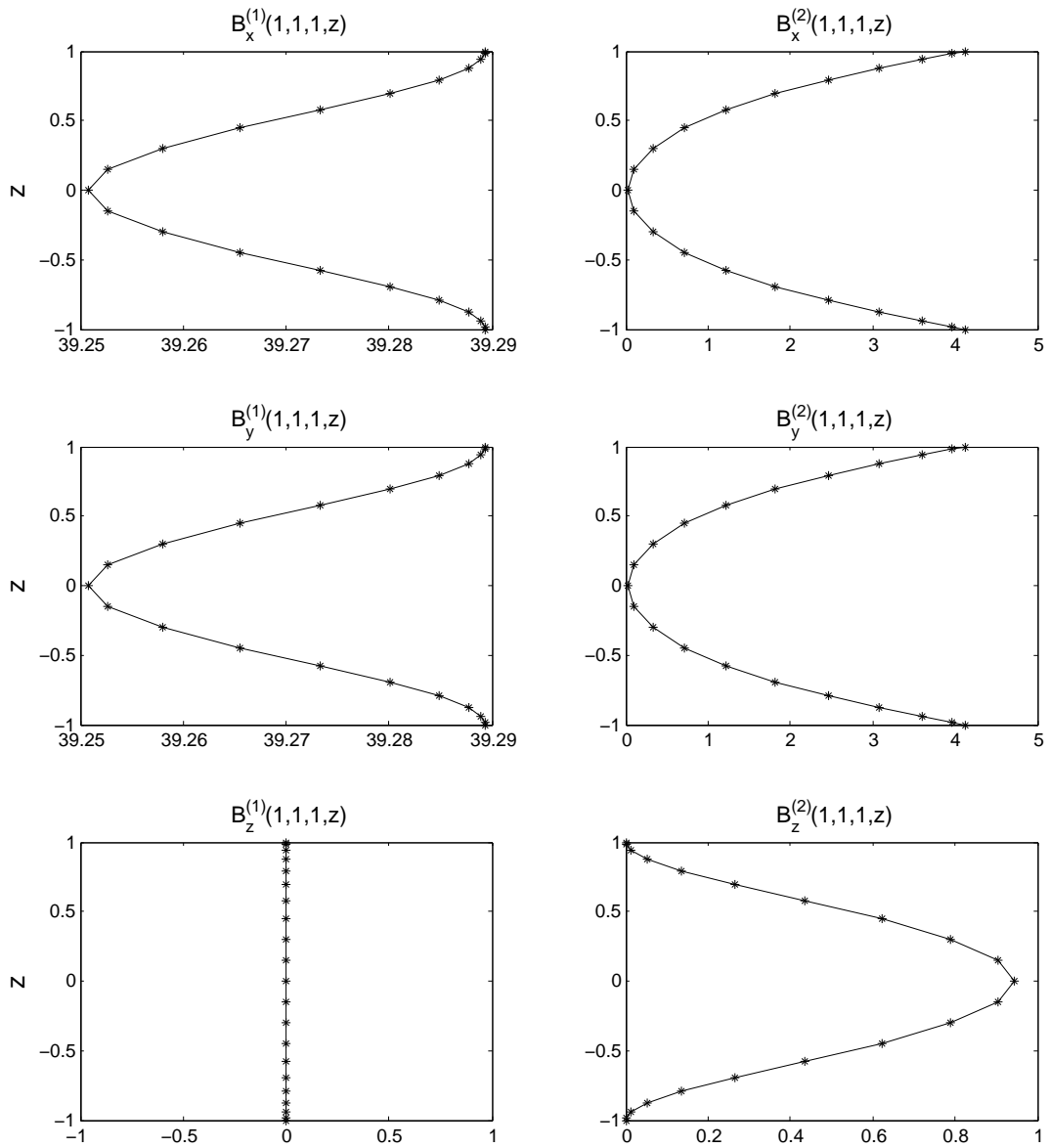
Figure 4.4: Magnetic solenoidal basis profile at $\chi = 30°$, $\xi_m = 1$ and $\eta_n = 1$ wavenumber pair.

4.3 Time Discretization

The linear terms are treated implicitly for the sake of the numerical stability [43], while non-linear advection and forcing terms are implemented explicitly. Thus, a semi-implicit scheme is used for the time discretization. In the initial testing stage, the nonlinear advective and forcing terms are discretized explicitly using second order Adams-Bashforth(AB2) and the linear terms implicitly by Crank Nicolson. We observed that for short time integration second order Adams-Bashforth is quite satisfactory, but for long time integration it is not suitable [41]. Then we tested third and fourth order semi-implicit schemes and Runge-Kutta type methods for the time integration of the system. We concluded that, third order Adams-Bashforth scheme is stable, robust and less costly than fourth and higher order Runge-Kutta type methods, as stated in Boyd [41]. So, the nonlinear advective terms are integrated explicitly using third order Adams-Bashforth and the linear terms are integrated implicitly by third order Adams-Moulton.

Fully nonlinear governing equations:

$$\frac{\partial \mathbf{u}}{\partial t} = -(\mathbf{u} \cdot \nabla)\mathbf{u} - \nabla\Pi + PrRa_h\Theta\mathbf{e}_z + Pr\nabla^2\mathbf{u} + Q_hPr(Cos\chi\partial y + Sin\chi\partial z)\mathbf{b}, \qquad (4.37)$$

$$\frac{\partial \Theta}{\partial t} + (\mathbf{u} \cdot \nabla)\Theta = \frac{w}{2} + \nabla^2\Theta, \qquad (4.38)$$

are then discretized in time based on the semi-implicit scheme mentioned

$$
\begin{aligned}
\frac{\mathbf{u}^{n+1} - \mathbf{u}^n}{\Delta t} &= \frac{23}{12}\left(-(\mathbf{u}\cdot\nabla)\mathbf{u} + PrRa\Theta e_z + Q_hPr(Cos\chi\partial y + Sin\chi\partial z)\mathbf{b}\right)^n \\
&\quad - \frac{16}{12}\left(-(\mathbf{u}\cdot\nabla)\mathbf{u} + PrRa\Theta e_z + Q_hPr(Cos\chi\partial y + Sin\chi\partial z)\mathbf{b}\right)^{n-1} \\
&\quad + \frac{5}{12}\left(-(\mathbf{u}\cdot\nabla)\mathbf{u} + PrRa\Theta e_z + Q_hPr(Cos\chi\partial y + Sin\chi\partial z)\mathbf{b}\right)^{n-2} \\
&\quad + Pr\nabla^2\left(\frac{5}{12}\mathbf{u}^{n+1} + \frac{8}{12}\mathbf{u}^n - \frac{1}{12}\mathbf{u}^{n-1}\right)
\end{aligned} \qquad (4.39)
$$

$$
\begin{aligned}
\frac{\Theta^{n+1} - \Theta^n}{\Delta t} &= \frac{23}{12}\left(-(\mathbf{u}\cdot\nabla)\Theta + \frac{w}{2}\right)^n - \frac{16}{12}\left(-(\mathbf{u}\cdot\nabla)\Theta + \frac{w}{2}\right)^{n-1} \\
&\quad + \frac{5}{12}\left(-(\mathbf{u}\cdot\nabla)\Theta + \frac{w}{2}\right)^{n-2} + \nabla^2\left(\frac{5}{12}\Theta^{n+1} + \frac{8}{12}\Theta^n - \frac{1}{12}\Theta^{n-1}\right)
\end{aligned} \qquad (4.40)
$$

or in more compact form:

$$\left(5Pr\nabla^2 - \frac{12}{\Delta t}\right)\mathbf{u}^{n+1} = g^n, \qquad (4.41)$$

$$\left(5\nabla^2 - \frac{12}{\Delta t}\right)\Theta^{n+1} = f^n, \tag{4.42}$$

where

$$\begin{aligned}
g^n \quad &= -23\left(-\left(\mathbf{u}\cdot\nabla\right)\mathbf{u} + PrRa\Theta e_z + Q_h Pr\left(Cos\chi\partial y + Sin\chi\partial z\right)\mathbf{b}\right)^n \\
&+ 16\left(-\left(\mathbf{u}\cdot\nabla\right)\mathbf{u} + PrRa\Theta e_z + Q_h Pr\left(Cos\chi\partial y + Sin\chi\partial z\right)\mathbf{b}\right)^{n-1} \\
&- 5\left(-\left(\mathbf{u}\cdot\nabla\right)\mathbf{u} + PrRa\Theta e_z + Q_h Pr\left(Cos\chi\partial y + Sin\chi\partial z\right)\mathbf{b}\right)^{n-2} \\
&- \left(8Pr\nabla^2 + \frac{12}{\Delta t}\right)\mathbf{u}^n + Pr\nabla^2\mathbf{u}^{n-1}
\end{aligned} \tag{4.43}$$

and

$$\begin{aligned}
f^n \quad &= -23\left(-\left(\mathbf{u}\cdot\nabla\right)\Theta + \frac{w}{2}\right)^n + 16\left(-\left(\mathbf{u}\cdot\nabla\right)\Theta + \frac{w}{2}\right)^{n-1} \\
&- 5\left(-\left(\mathbf{u}\cdot\nabla\right)\Theta + \frac{w}{2}\right)^{n-2} - \left(8\nabla^2 + \frac{12}{\Delta t}\right)\Theta^n + \nabla^2\Theta^{n-1}.
\end{aligned} \tag{4.44}$$

The time scheme is third order accurate, robust and stable, whereas it needs three known starting steps to start the iteration. The linear solution of the problem is used as the initial step.

4.4 Nonlinear Implementation

Momentum and Energy equations contain nonlinear advection terms which have significant importance at high Rayleigh numbers. Since convolution sum is needed in calculation of these nonlinear terms in Fourier space and consume more CPU time in Fourier space than in real space, all nonlinear terms are calculated in real space and then transformed to Fourier space to obtain their Fourier coefficients,

$$
c^{1,2} = \left(\bar{V}, (\mathbf{u} \cdot \nabla) \mathbf{u} \right) = \int_0^{L_x} \int_0^{L_y} \int_{-1}^{1} \left(\bar{V}^* (\mathbf{u} \cdot \nabla) \mathbf{u} \right) dx dy dz \tag{4.45}
$$

$$
d = \left(\bar{T}, (\mathbf{u} \cdot \nabla) \Theta \right) = \int_0^{L_x} \int_0^{L_y} \int_{-1}^{1} \left(\bar{T}^* (\mathbf{u} \cdot \nabla) \Theta \right) dx dy dz \tag{4.46}
$$

where $c^{(1)}$, $c^{(2)}$ and d are the time dependent coefficients corresponding to the nonlinear terms projected onto the corresponding dual space. Forward and backward Fast Fourier transforms (FFT) have been used in moving between real and Fourier spaces.

Derivatives of velocity and temperature fields are calculated by using Fast Fourier transforms for horizontal directions, while polynomial differentiation matrices [44] have been used for vertical direction. Fourier differentiation matrix approach [44] has been tested for horizontal derivatives as well, but it observed that FFT differentiation approach is faster than differentiation matrix approach for higher horizontal resolution.
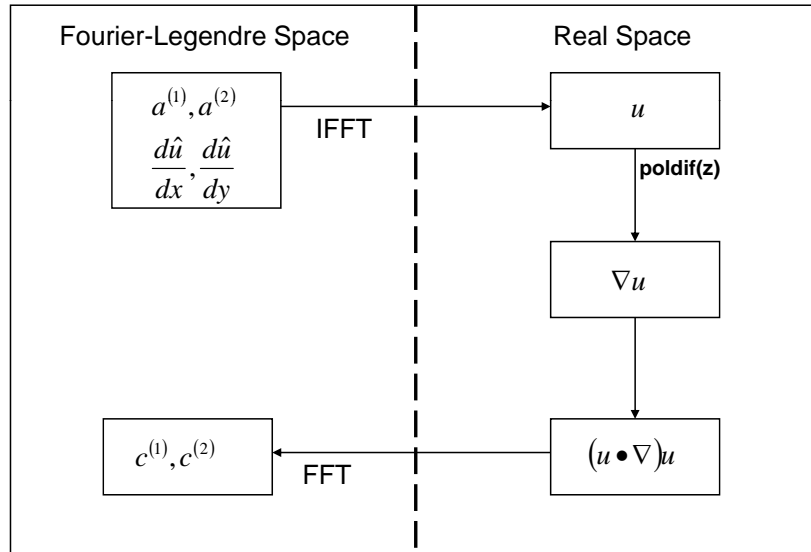
Figure 4.5: A schematic flow diagram of the solution of the time dependent nonlinear terms $c^{(1)}$ and $c^{(2)}$.
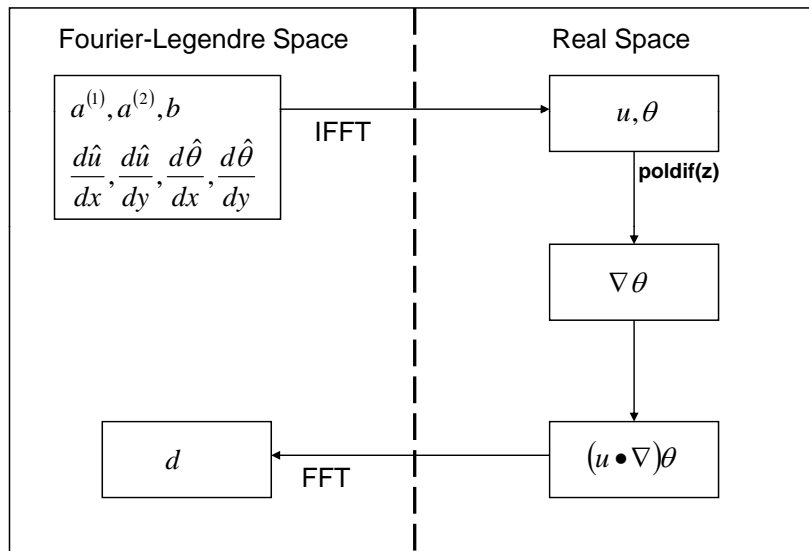
Figure 4.6: A schematic flow diagram of the solution of the time dependent nonlinear terms d.

CHAPTER 5

THERMAL CONVECTION UNDER VERTICAL MAGNETIC FIELD

A numerical study is performed in a periodic horizontal layer of thickness d between conducting plates that are heated from below under the influence of a uniform vertical magnetic field B_0 applied externally in order to study the effect of vertical magnetic field on the flow driven by the buoyancy in a rectangular cavity filled with low Prandtl number fluids such as silicon (Pr = 0.01), gallium (Pr = 0.023) and molten silicon (Pr = 0.054) (Figure 5.1).
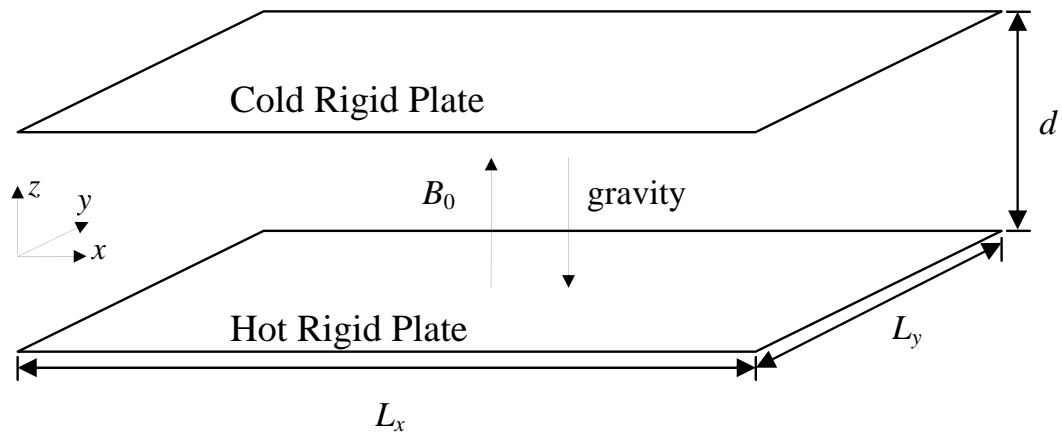
Figure 5.1: The geometry of the periodic convective domain under the vertical magnetic field

In this section, the governing equations for the vertical magnetic field are stated first as a special case of the oblique equations of Chapter 2. Weak formulation in terms of the generated bases is given. Discretized form of the equations is then numerically integrated to study the

linear and nonlinear convective regimes. The effect of the vertical magnetic field on thermal convection is studied in these regime. The results are discussed and compared with theoretical and experimental results in literature.

5.1 Governing Equations

To ensure the continuity of this chapter, some of the formulations in the previous chapters are repeated. Nondimensional form of the governing equations when only the vertical magnetic field is present in the system is written by introducing $\chi = \pi/2$ to (2.32)-(2.36) in the following form:

$$\nabla \cdot \mathbf{u} = 0, \tag{5.1}$$

$$\frac{\partial \mathbf{u}}{\partial t} = -(\mathbf{u} \cdot \nabla)\mathbf{u} - \nabla\Pi + PrRa_h\Theta\mathbf{e}_z + Pr\nabla^2\mathbf{u} + Q_hPr(\mathbf{e}_z \cdot \nabla)\mathbf{b}, \tag{5.2}$$

$$\frac{\partial \Theta}{\partial t} + (\mathbf{u} \cdot \nabla)\Theta = \frac{w}{2} + \nabla^2\Theta, \tag{5.3}$$

$$\nabla \cdot \mathbf{b} = 0, \tag{5.4}$$

$$\nabla^2\mathbf{b} = -(\mathbf{e}_z \cdot \nabla)\mathbf{u}, \tag{5.5}$$

where $\mathbf{e}_z$ is the unit vector in the z direction opposite to the direction of gravity, $\mathbf{b} = (b_x, b_y, b_z)$ the induced magnetic vector field and Θ is the deviation from the linear conductive temperature profile. The three dimensionless parameters Rayleigh ($Ra = 8Ra_h$), Chandrasekhar ($Q = 4Q_h$) and Prandtl (Pr) numbers in the vertical magnetic field are, as before, defined as follows:

$$Ra = \frac{g \triangle T d^3 \alpha}{\kappa\nu}, \quad Q = \frac{B_0^2 d^2}{\rho\mu\nu\lambda}, \quad Pr = \frac{\nu}{\kappa}. \tag{5.6}$$

The total magnetic field in the presence of an externally applied vertical magnetic field becomes

$$\mathbf{B} = \mathbf{e}_z + \frac{\kappa}{\lambda}\mathbf{b} \tag{5.7}$$

which indicates that the induced magnetic field $\mathbf{b}$ is weak compared to the externally imposed uniform magnetic field B_0 with the assumption of low magnetic Prandtl number $P_m = \nu/\lambda$ ($\kappa \ll \lambda$). Since the solenoidal bases are constructed to satisfy the divergence-free conditions and as well as the quasi-steady relation between magnetic and velocity fields, the equations (5.1), (5.4) and (5.5) are automatically satisfied. The number of equations in the system is

reduced from nine to four equations that are the momentum and the energy equations. After the introduction of the truncated expansion of the flow variables in terms of the bases as in (4.3), (4.4) and (4.5), the residues in these equations can be written in the following form:

$$R_{\mathbf{u}} = -\frac{\partial \mathbf{u}}{\partial t} - (\mathbf{u} \cdot \nabla)\mathbf{u} - \nabla\Pi + PrRa_h\Theta e_z + Pr\nabla^2\mathbf{u} + Q_hPr(e_z \cdot \nabla)\mathbf{b}, \tag{5.8}$$

$$R_\Theta = -\frac{\partial \Theta}{\partial t} - (\mathbf{u} \cdot \nabla)\Theta - \frac{w}{2} + \nabla^2\Theta, \tag{5.9}$$

The vanishing Galerkin projection of these residues in the projection space spanned by the dual vectors $\bar{V}_p^{(1)}$, $\bar{V}_p^{(2)}$ and $\bar{T}_p$ yields

$$\int_0^{L_x}\int_0^{L_y}\int_{-1}^1 \bar{V} \cdot R_{\mathbf{u}}\, dz = \int_0^{L_x}\int_0^{L_y}\int_{-1}^1 \bar{V} \cdot \left[-\frac{\partial \mathbf{u}}{\partial t} - (\mathbf{u} \cdot \nabla)\mathbf{u} - \nabla\Pi + PrRa_h\Theta e_z\right]dxdydz \quad +$$

$$\int_0^{L_x}\int_0^{L_y}\int_{-1}^1 \bar{V} \cdot \left[Pr\nabla^2\mathbf{u} + Q_hPr(e_z \cdot \nabla)\mathbf{b}\right]dxdydz = 0 \tag{5.10}$$

$$\int_0^{L_x}\int_0^{L_y}\int_{-1}^1 \bar{T}R_\Theta\, dz = \int_0^{L_x}\int_0^{L_y}\int_{-1}^1 \bar{T}\left[-\frac{\partial \Theta}{\partial t} - (\mathbf{u} \cdot \nabla)\Theta - \frac{w}{2} + \nabla^2\Theta\right]dxdydz = 0 \tag{5.11}$$

or in compact matrix form:

$$
\underbrace{\begin{bmatrix} \left(\bar{V}_q^{(1)}, V_p^{(1)}\right) & 0 & 0 \\ 0 & \left(\bar{V}_q^{(2)}, V_p^{(2)}\right) & 0 \\ 0 & 0 & \left(\bar{T}_q, T_p\right) \end{bmatrix}}_{Mass-Matrix}\begin{bmatrix} \dot{a}_p^{(1)} \\ \dot{a}_p^{(2)} \\ \dot{b}_p \end{bmatrix} + \begin{bmatrix} c^{(1)} \\ c^{(2)} \\ d \end{bmatrix} =
$$

$$
Pr\underbrace{\begin{bmatrix} \begin{array}{c}\left(\bar{V}_q^{(1)}, (-\gamma^2 + \mathbb{D}^2)V_p^{(1)}\right) + \\ \left(\bar{V}_q^{(1)}, Q_h\mathbb{D}B_p^{(1)}\right)\end{array} & 0 & 0 \\ 0 & \begin{array}{c}\left(\bar{V}_q^{(2)}, (-\gamma^2 + \mathbb{D}^2)V_p^{(2)}\right) + \\ \left(\bar{V}_q^{(2)}, Q_h\mathbb{D}B_p^{(2)}\right)\end{array} & Ra_h\left(\bar{V}_q^{(2)}, T_pe_z\right) \\ 0 & \left(\bar{T}_q, V_p^{(2)} \cdot e_z\right)/2Pr & \left(\bar{T}_q, \nabla^2 T_p\right)/Pr \end{bmatrix}}_{Stiffness-Matrix}\begin{bmatrix} a_p^{(1)} \\ a_p^{(2)} \\ b_p \end{bmatrix} \tag{5.12}
$$

where $\gamma^2 = \xi^2 + \eta^2$ and $\mathbb{D} = \frac{d}{dz}$.

5.2 Linear Stability Analysis

Linear stability of the magnetoconvection equations is investigated by Chandrasekhar [5]. For non-magnetic case, Chandrasekhar found that critical wavenumber and critical Rayleigh number are independent of the Prandtl number at the convective threshold. Reid and Harris [42] found the stability curve has one minima at critical wavenumber equal to 3.117 and critical Rayleigh numbers at 1707.8 for viscous fluids confined between rigid plate. Below the critical value, there is no motion and the heat is transferred by conduction across the fluid layer.

In order to test the solenoidal basis and the projection procedure, first we consider the linear stability of the conductive (no-motion) state leading to the critical values when the convective motion just sets in. At this state, the velocity and temperature perturbations over the conductive state are small, and so the nonlinear terms in the governing equations (2.33) and (2.34) can be linearized around no-motion state to get the residues:

$$R_{\mathbf{u}} = -\frac{\partial \mathbf{u}}{\partial t} - \nabla\Pi + PrRa_h \Theta \mathbf{e}_z + Pr\nabla^2\mathbf{u} + Q_h Pr\left(\mathbf{e}_z \cdot \nabla\right)\mathbf{b}, \qquad (5.13)$$

$$R_{\Theta} = -\frac{\partial \Theta}{\partial t} - \frac{w}{2} + \nabla^2\Theta. \qquad (5.14)$$

and their Galerkin projections as follows:

$$\int_0^{L_x}\int_0^{L_y}\int_{-1}^{1} \bar{V} \cdot R_{\mathbf{u}}\, dz = \int_0^{L_x}\int_0^{L_y}\int_{-1}^{1} \bar{V} \cdot \left[-\frac{\partial \mathbf{u}}{\partial t} - \nabla\Pi + PrRa_h\Theta e_z\right] dxdydz \;\; +$$

$$\int_0^{L_x}\int_0^{L_y}\int_{-1}^{1} \bar{V} \cdot \left[Pr\nabla^2\mathbf{u} + Q_h Pr\left(\mathbf{e}_z \cdot \nabla\right)\mathbf{b}\right] dxdydz = 0 \qquad (5.15)$$

$$\int_0^{L_x}\int_0^{L_y}\int_{-1}^{1} \bar{T}R_{\Theta}\, dz = \int_0^{L_x}\int_0^{L_y}\int_{-1}^{1} \bar{T}\left[-\frac{\partial \Theta}{\partial t} - \frac{w}{2} + \nabla^2\Theta\right] dxdydz = 0. \qquad (5.16)$$

This system of ordinary differential equations can be written in matrix form:

$$\begin{bmatrix} \left(\bar{V}_q^{(1)}, \hat{V}_p^{(1)}\right) & \left(\bar{V}_q^{(1)}, V_p^{(2)}\right) \\ \left(\bar{V}_q^{(2)}, V_p^{(1)}\right) & \left(\bar{V}_q^{(2)}, V_p^{(2)}\right) \end{bmatrix} \begin{bmatrix} \dot{a}_p^{(1)} \\ \dot{a}_p^{(2)} \end{bmatrix} = PrRa_h \begin{bmatrix} \left(\bar{V}_q^{(1)}, T_p e_z\right) \\ \left(\bar{V}_q^{(2)}, T_p e_z\right) \end{bmatrix} \begin{bmatrix} b_p \end{bmatrix}$$

$$+ Pr \begin{bmatrix} \left(\bar{V}_q^{(1)}, \nabla^2 V_p^{(1)}\right) & \left(\bar{V}_q^{(1)}, \nabla^2 V_p^{(2)}\right) \\ \left(\bar{V}_q^{(2)}, \nabla^2 V_p^{(1)}\right) & \left(\bar{V}_q^{(2)}, \nabla^2 V_p^{(2)}\right) \end{bmatrix} \begin{bmatrix} a_p^{(1)} \\ a_p^{(2)} \end{bmatrix} \tag{5.17}$$

$$+ Pr \begin{bmatrix} \left(\bar{V}_q^{(1)}, Q_h \left(\mathbf{e}_z \cdot \nabla\right) B_p^{(1)}\right) & \left(\bar{V}_q^{(1)}, Q_h \left(\mathbf{e}_z \cdot \nabla\right) B_p^{(2)}\right) \\ \left(\bar{V}_q^{(2)}, Q_h \left(\mathbf{e}_z \cdot \nabla\right) B_p^{(1)}\right) & \left(\bar{V}_q^{(2)}, Q_h \left(\mathbf{e}_z \cdot \nabla\right) B_p^{(2)}\right) \end{bmatrix} \begin{bmatrix} a_p^{(1)} \\ a_p^{(2)} \end{bmatrix}$$

$$\left(\bar{T}_q, T_p\right) \dot{b}_p = \left(\bar{T}_q, V_p^{(1)} \cdot e_z\right) a_p^{(1)} + \left(\bar{T}_q, V_p^{(2)} \cdot e_z\right) a_p^{(2)} + \left(\bar{T}_q, \nabla^2 T_p\right) b_p \tag{5.18}$$

Due to construction of the solenoidal basis and their duals, cross inner product terms between the bases and their duals vanish, therefore the system (5.17) and (5.18) reduce to:

$$\begin{bmatrix} \left(\bar{V}_q^{(1)}, \hat{V}_p^{(1)}\right) & 0 \\ 0 & \left(\bar{V}_q^{(2)}, V_p^{(2)}\right) \end{bmatrix} \begin{bmatrix} \dot{a}_p^{(1)} \\ \dot{a}_p^{(2)} \end{bmatrix} = PrRa_h \begin{bmatrix} 0 \\ \left(\bar{V}_q^{(2)}, T_p e_z\right) \end{bmatrix} \begin{bmatrix} b_p \end{bmatrix}$$

$$+ Pr \begin{bmatrix} \left(\bar{V}_q^{(1)}, \nabla^2 V_p^{(1)}\right) & 0 \\ 0 & \left(\bar{V}_q^{(2)}, \nabla^2 V_p^{(2)}\right) \end{bmatrix} \begin{bmatrix} a_p^{(1)} \\ a_p^{(2)} \end{bmatrix} \tag{5.19}$$

$$+ Pr \begin{bmatrix} \left(\bar{V}_q^{(1)}, Q_h \left(\mathbf{e}_z \cdot \nabla\right) B_p^{(1)}\right) & 0 \\ 0 & \left(\bar{V}_q^{(2)}, Q_h \left(\mathbf{e}_z \cdot \nabla\right) B_p^{(2)}\right) \end{bmatrix} \begin{bmatrix} a_p^{(1)} \\ a_p^{(2)} \end{bmatrix}$$

$$\left(\bar{T}_q, T_p\right) \dot{b}_p = \left(\bar{T}_q, V_p^{(2)} \cdot e_z\right) a_p^{(2)} + \left(\bar{T}_q, \nabla^2 T_p\right) b_p \tag{5.20}$$

If the equations (5.19) and (5.20) are combined in a system and written in the matrix form, the Mass and Stiffness matrices for the linearized system are obtained as:

$$
\underbrace{
\begin{bmatrix}
\left(\bar{V}_q^{(1)}, V_p^{(1)}\right) & 0 & 0 \\
0 & \left(\bar{V}_q^{(2)}, V_p^{(2)}\right) & 0 \\
0 & 0 & \left(\bar{T}_q, T_p\right)
\end{bmatrix}
}_{Mass-Matrix}
\begin{bmatrix}
\dot{a}_p^{(1)} \\
\dot{a}_p^{(2)} \\
\dot{b}_p
\end{bmatrix}
=
$$

$$
Pr
\underbrace{
\begin{bmatrix}
\left(\bar{V}_q^{(1)}, (-\gamma^2 + \mathbb{D}^2)V_p^{(1)}\right) + & 0 & 0 \\
\left(\bar{V}_q^{(1)}, Q_h \mathbb{D} B_p^{(1)}\right) & & \\
0 & \left(\bar{V}_q^{(2)}, (-\gamma^2 + \mathbb{D}^2)V_p^{(2)}\right) + & Ra_h\left(\bar{V}_q^{(2)}, T_p e_z\right) \\
& \left(\bar{V}_q^{(2)}, Q_h \mathbb{D} B_p^{(2)}\right) & \\
0 & \left(\bar{T}_q, V_p^{(2)} \cdot e_z\right)/2Pr & \left(\bar{T}_q, \nabla^2 T_p\right)/Pr
\end{bmatrix}
}_{Stiffness-Matrix}
\begin{bmatrix}
a_p^{(1)} \\
a_p^{(2)} \\
b_p
\end{bmatrix}. \qquad (5.21)
$$

These matrices can be computed numerically by using the spatial discretization introduced in section 4.1.

The assumption of time dependence in the form

$$
[a^{(1)}; a^{(2)}; b] \propto exp(\varsigma t) \qquad (5.22)
$$

reduces the system to a generalized eigenvalue problem for the eigenvalues ς. The critical wave-number k_c and Rayleigh number Ra_c values for different Q values are listed in Table 5.1 for the rightmost eigenvalue just crossing the imaginary axis. These are obtained at the selection of $n = 0$ and $m = 1$ (that is, $k_c = \xi_1 = 2\pi/s_x$) in (4.3), (4.4) and (4.5). The variation of the wave number k_c at the onset of the instability as a function of Q and the variation of the critical Rayleigh number for the onset of instability as a function of Q are plotted in Figures 5.2 and 5.3, respectively. The corresponding marginal stability curves for increasing Q values is plotted in Figure 5.5. The eigenvalue spectrum of the critical Rayleigh number for the corresponding Chandrasekhar number is shown in Figure 5.4. These are in agreement with the linear analysis in Chandrasekhar [5]. The increase in the critical wave number with increasing Chandrasekhar number is in agreement with the reported asymptotic dependence on Q of the associated wave number, as stated in Chandrasekhar [5].
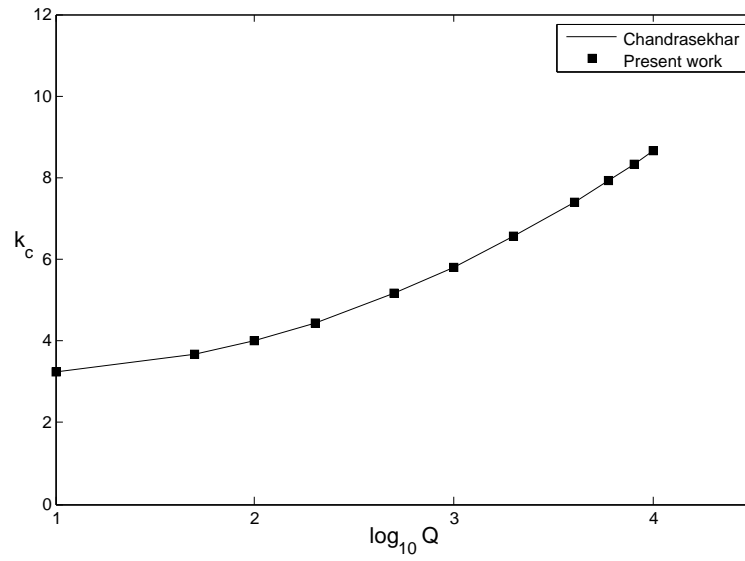
Figure 5.2: Critic wave number(k_c) versus magnetic field strength (Q).
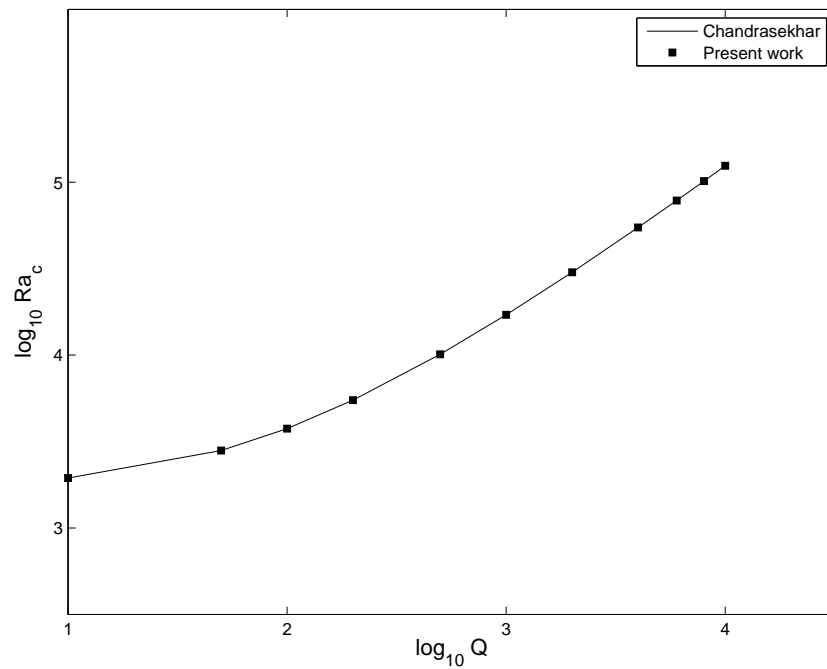
Figure 5.3: Critic Rayleigh number (Ra_c) versus magnetic field strength (Q)

Table 5.1: Linear stability points for various Q and wavenumber k_c

		Chandrasekhar [5]	Present Work (Resolution)
Q	k_c	Ra_c	Ra_c $(N_x \times N_y \times N_z)$
0	3.13	1707.8	1707.8 $(4 \times 4 \times 9)$
10	3.25	1945.9	1945.8 $(4 \times 4 \times 13)$
50	3.68	2802.1	2802.1 $(4 \times 4 \times 13)$
100	4.00	3757.4	3757.4 $(4 \times 4 \times 17)$
200	4.45	5488.6	5488.6 $(4 \times 4 \times 17)$
500	5.16	10110.0	10110.0 $(4 \times 4 \times 21)$
1000	5.80	17103.0	17103.0 $(4 \times 4 \times 21)$
2000	6.55	30125.0	30125.0 $(4 \times 4 \times 25)$
4000	7.40	54697.0	54697.0 $(4 \times 4 \times 29)$
6000	7.94	78391.0	78391.0 $(4 \times 4 \times 29)$
8000	8.34	101606.0	101606.0 $(4 \times 4 \times 29)$
10000	8.66	124509.0	124509.0 $(4 \times 4 \times 33)$

Figure 5.4: Eigenvalue spectrum at critic Rayleigh number for different Chandrasekhar numbers.

Figure 5.5: Linear stability curves for different magnetic field strength. Solid circle shows critic wavenumber, k_c and corresponding critic Rayleigh number, Ra_c.
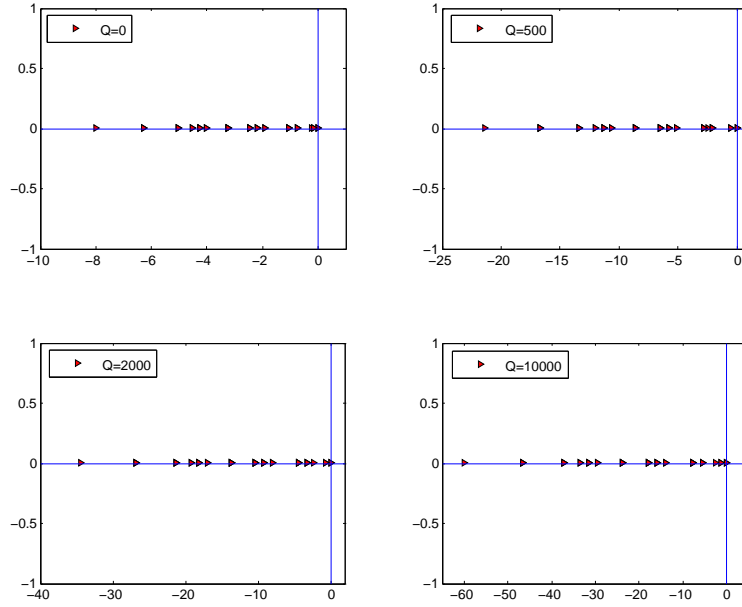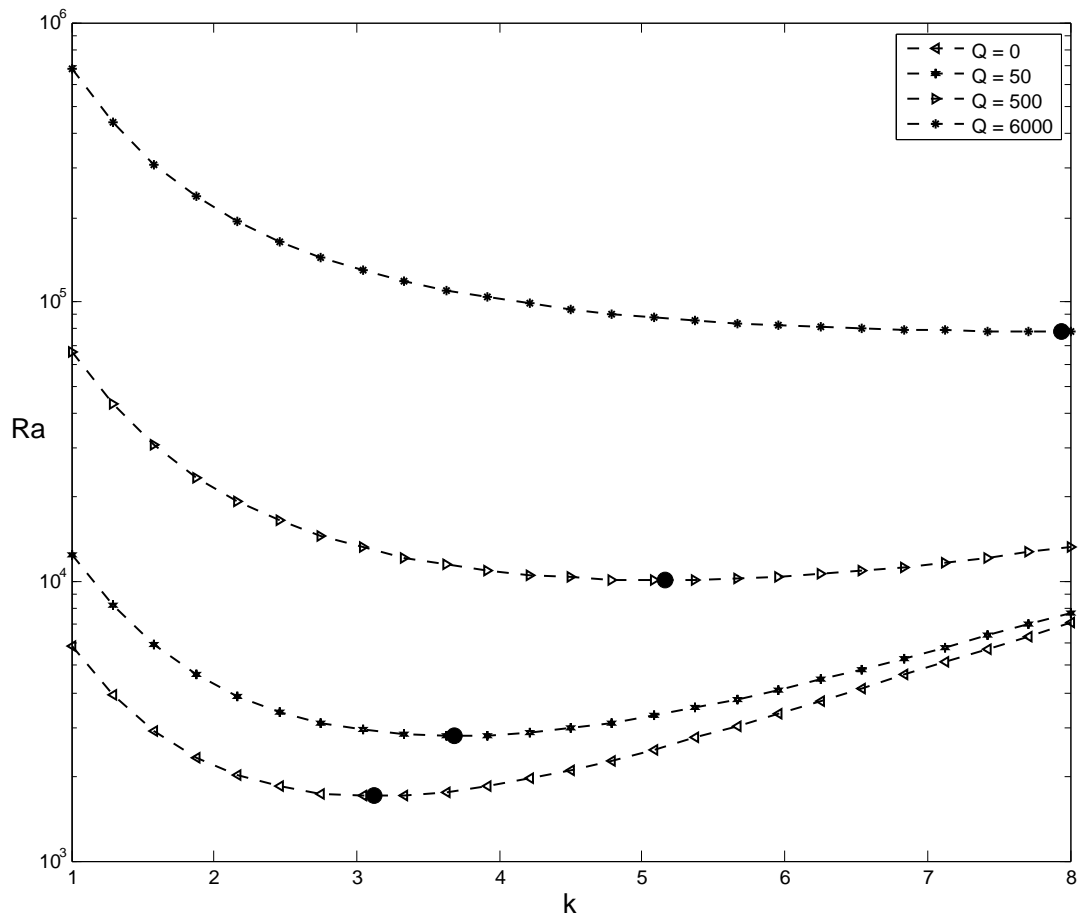
5.3 Nonlinear Analysis

Time discretization of the governing system (5.12) is obtained semi-implicitly by third or-
der Adams-Bashforth (AB3) and Adams-Moulton (AM3) schemes. The nonlinear advective
terms are integrated explicitly using third order Adams-Bashforth and the linear terms are
integrated implicitly by third order Adams-Moulton. The resulting time discretized form of
the nonlinear governing system can be written in more compact form as follows:

$$\left(5Pr\nabla^2 - \frac{12}{\Delta t}\right)\mathbf{u}^{n+1} = g^n, \tag{5.23}$$

$$\left(5\nabla^2 - \frac{12}{\Delta t}\right)\Theta^{n+1} = f^n, \tag{5.24}$$

where

$$
\begin{aligned}
g^n \quad &= -23\left(-(\mathbf{u}\cdot\nabla)\mathbf{u} + PrRa\Theta e_z + Q_h Pr\mathbb{D}\mathbf{b}\right)^n \\
&+ 16\left(-(\mathbf{u}\cdot\nabla)\mathbf{u} + PrRa\Theta e_z + Q_h Pr\mathbb{D}\mathbf{b}\right)^{n-1} \\
&- 5\left(-(\mathbf{u}\cdot\nabla)\mathbf{u} + PrRa\Theta e_z + Q_h Pr\mathbb{D}\mathbf{b}\right)^{n-2} \\
&- \left(8Pr\nabla^2 + \frac{12}{\Delta t}\right)\mathbf{u}^n + Pr\nabla^2\mathbf{u}^{n-1}
\end{aligned}
\tag{5.25}
$$

and

$$
\begin{aligned}
f^n \quad &= -23\left(-(\mathbf{u}\cdot\nabla)\Theta + \frac{w}{2}\right)^n + 16\left(-(\mathbf{u}\cdot\nabla)\Theta + \frac{w}{2}\right)^{n-1} \\
&- 5\left(-(\mathbf{u}\cdot\nabla)\Theta + \frac{w}{2}\right)^{n-2} - \left(8\nabla^2 + \frac{12}{\Delta t}\right)\Theta^n + \nabla^2\Theta^{n-1}.
\end{aligned}
\tag{5.26}
$$

The initial conditions for the time dependent coefficients are obtained from the linear solu-
tion of the governing equations (5.13-5.14). Random perturbations are added onto the time
dependent coefficients of temperature. The numerical integration is continued until transients
disappear. For instance, for 2-D steady roll regime, the integration is continued until the
toroidal component of the kinetic energy (E_{tor}) reduces to 10^{-16}. Each run uses the last nu-
merical flow field of the previous run as the initial condition.

In the horizontal directions, a resolution of $N_x = N_y = 16$ and in the vertical direction, $N_z = 21$
are mostly used in the subsequent simulations unless stated otherwise. In the horizontal direc-
tions 16 nodes are well enough to resolve the model equations, but in the vertical z direction

at least $N_z = 21$ nodes should be used for high Rayleigh and Chandrasekhar numbers. But, higher resolutions, such as $N_z = 25$ or $N_z = 29$, are used in the vertical direction in order to test the results for convergence. Samples of convergence with the resolution are shown in Tables 5.2 and 5.3. Results in these tables are generated for two different Rayleigh numbers, $Ra = 15000$ and $Ra = 30000$, and for $Q = 400$ with an aspect ratio $\Gamma [3 : 1.5]$. Nusselt number values corresponding to the vertical resolution $N_z = 21$, $N_z = 25$ and $N_z = 29$ show little change.

Table 5.2: Grid refinement test in horizontal directions for $Pr = 0.05$ and $Q = 400$.

	$N_x = N_y = 12$	$N_x = N_y = 16$	$N_x = N_y = 20$
$Ra = 15000$	$Nu = 1.4522$	$Nu = 1.4528$	$Nu = 1.4523$
$Ra = 30000$	$Nu = 2.2829$	$Nu = 2.2802$	$Nu = 2.2870$

Table 5.3: Grid refinement test in vertical direction for $Pr = 0.05$ and $Q = 400$.

	$N_z = 21$	$N_z = 25$	$N_z = 29$
$Ra = 15000$	$Nu = 1.4522$	$Nu = 1.4528$	$Nu = 1.4528$
$Ra = 30000$	$Nu = 2.2857$	$Nu = 2.2802$	$Nu = 2.2805$

Polynomial interpolation over Gauss-Legendre-Lobatto (GLL) grid provides denser nodal configurations near the z boundaries, which help representing boundary layers accurately. For example, in order to resolve the thermal boundary layers, at least, three nodes should be included in this layer for stability. Here, the thermal boundary layer thickness δ_θ can be written in terms of heat transfer rate as stated in [45], as follows:

$$\delta_\theta = \frac{1}{2Nu}. \tag{5.27}$$

Time steps Δt are selected in the interval $1 \times 10^{-4} < \Delta t < 5 \times 10^{-3}$. In any case, $\Delta t = 5 \times 10^{-3}$ is used first, if it is not resolving enough, then it is halved and, so on.

Averaged kinetic energy, poloidal and toroidal energy, Nusselt number, frequency of oscillations are monitored during the time integration. The averaged kinetic energy is computed by

integration of the square of the horizontally and time averaged velocity field along z, that is:

$$E = \frac{1}{2} \int_{-1}^{1} \langle u \rangle^2 \, dz. \qquad (5.28)$$

Since the velocity field is solenoidal, it can be decomposed in the following form

$$\mathbf{u} = \nabla \times (\nabla \times \mathbf{e}_z \varphi) + \nabla \times \mathbf{e}_z \psi. \qquad (5.29)$$

Here, the first term denotes the poloidal and the second term the toroidal components of the velocity for some functions φ and ψ. The poloidal component of velocity with vanishing vertical vorticity component is related to the two-dimensional convective rolls. Furthermore, only the poloidal component of motion contributes to the convective heat transport. The poloidal component of the kinetic energy is computed by integration of the square of the average of the first term in (5.29) along z, as follows:

$$E_{pol} = \frac{1}{2} \int_{-1}^{1} \langle \nabla \times (\nabla \times \mathbf{e}_z \varphi) \rangle^2 \, dz. \qquad (5.30)$$

Since the toroidal component of velocity is associated with the vertical vorticity component, it shows oscillatory regime features in which vertical vorticity plays important role and it is inactive for the two-dimensional steady roll regime. The toroidal component of kinetic energy is computed by integration of the square of the average of the second term in (5.29) along z, that is:

$$E_{tor} = \frac{1}{2} \int_{-1}^{1} \langle \nabla \times \mathbf{e}_z \psi \rangle^2 \, dz. \qquad (5.31)$$

The energy of the toroidal component of motion increases with Rayleigh number while that of the poloidal component exhibits the similar variation as the heat transport.

The effectiveness of the convective heat transport is characterized by the dimensionless Nusselt number which is defined by the ratio of the total heat transport to heat transport by heat conduction only between top and bottom plates. It can be computed simply by using the averaged temperature gradient at the wall as follows:

$$Nu = 1 + 2 \left| \left\langle \frac{\partial \Theta}{\partial z} \right\rangle \right|_{wall} . \qquad (5.32)$$

If Nusselt number is close to unity, it indicates weak convective motions. A larger Nusselt number corresponds to stronger convective motions. The frequency f and the period $T = 1/f$ are used to quantify the flow in the oscillatory regimes (periodic, double periodic, etc.)

5.3.1 Stationary Flow

The numerical experiments are performed to study the effects of varying Q (magnetic field strength) and Ra (Rayleigh number) on the convective heat transport efficiency indicated by Nusselt number (Nu). Numerical results are compared with the numerical study of Mössner and Müller [25]. In their study, the flow is numerically investigated in a rectangular cavity with aspect ratio Γ [6 : 3] using a resolution of at least $80 \times 80 \times 128$. In their study, the natural convection is driven by a vertical temperature gradient and magnetic field is vertically oriented. The lateral walls are taken as adiabatic. The calculations are presented for varying Hartmann number, which corresponds to the square root of Chandrasekhar number, for $Ra \leq 5 \cdot 10^4$ and $Pr = 0.05$ and a second-order finite difference scheme with staggered grid is employed to solve the dimensionless equations with Adams-Bashforth time discretization for dimensionless time step $\Delta t = 10^{-3}$ and $\Delta t = 10^{-4}$. They report the dependence of the number convection rolls on Rayleigh and Chandrasekhar numbers. It is shown that the number of the rolls in the cavity decreases with increasing Rayleigh number whereas increases with increasing Chandrasekhar number.

In the present study, a liquid metal with $Pr = 0.05$ is selected as the convective fluid in a layer with aspect ratio Γ [3 : 1.5] and subjected to a vertical magnetic field. The eigenfunctions of the linear stability is taken as the initial condition. In our computation, at most $16 \times 16 \times 21$ grid size is used which is almost mush less than [25] in each direction and perfectly conducting rigid boundaries are taken in z direction whereas z boundaries are electrically insulated in [25]. Despite these differences in configuration, the Nusselt number values obtained in Table 5.4 are all comparable but bigger than those reported in [25]. This is also due to restraining influence of the lateral walls in [25]. The reported result in [25] that the number of the convection rolls increases as the Chandrasekhar number increases is also observed in the present study.

In Figures 5.6-5.9, the time record of nonmagnetic convective flow ($Q = 0$) for three components of velocity and temperature is compared with the magnetoconvective flow at $Q = 400$ for a Rayleigh number of $Ra = 15000$. While a chaotic flow is observed in ($Q = 0$) case, when a magnetic field corresponding to $Q = 400$ is imposed to the convective flow, the fluctuations are damped.

The power spectrum for the nonmagnetic and the magnetoconvective flows are compared

in Figure 5.10 for velocity and in Figure 5.11 for temperature at Chandrasekhar number of $Q = 400$ and Rayleigh number of $Ra = 15000$. When the power spectrum of non-magnetic case ($Q = 0$) is compared with the power spectrum of magnetoconvective flow at $Q = 400$, damping is observed in the whole frequency range. The damping effect of the vertical magnetic field is also observed in Nusselt number values in Figure 5.14. The chaotic flow dampens to a stationary flow when a magnetic field corresponding to $Q = 400$ and $Ra = 15000$ is imposed.

A further verification of the present computation is presented in Figures 5.12 and 5.13 that the lateral extension of the rolls in the $y-$direction decreases with increasing Chandrasekhar number, as also reported in [25].

Table 5.4: *Nu* and flow pattern for *Pr* = 0.05 and **B** ∥ **g**.

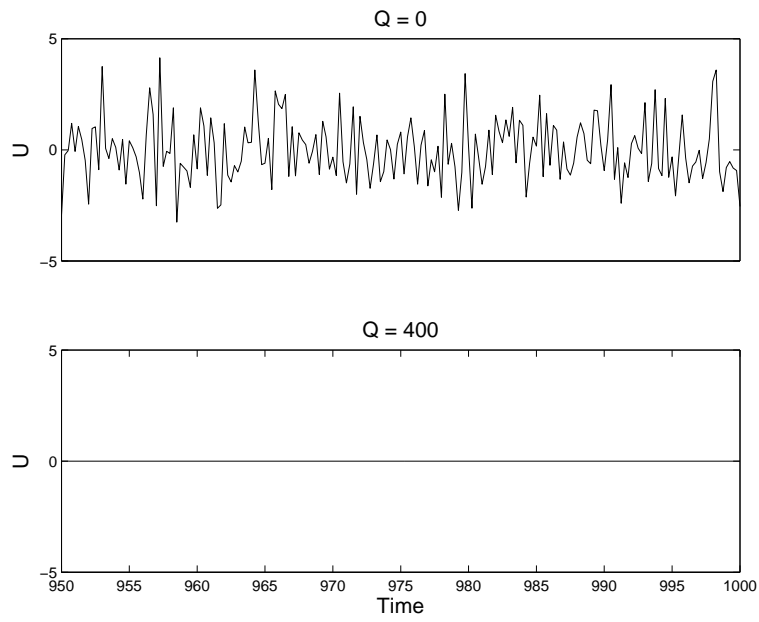|	Chandrasekhar Number (Q)	Nu (Roll numbers)	
		[25] Γ [6 : 3]	Present Work Γ [3 : 1.5]
	$Q = 0$	1.98 (4 rolls)	2.53 (2 rolls)
	$Q = 400$	1.32 (6 rolls)	1.45 (4 rolls)
$Ra = 15000$	$Q = 625$	1.23 (6 rolls)	1.36 (4 rolls)
	$Q = 784$	1.12 (8 rolls)	1.09 (4 rolls)
	$Q = 900$	1	1
	$Q = 0$	2.49 (4 rolls)	2.92 (2 rolls)
	$Q = 400$	2.19 (6 rolls)	2.58 (4 rolls)
$Ra = 30000$	$Q = 900$	1.57 (6 rolls)	1.88 (4 rolls)
	$Q = 1225$	1.31 (8 rolls)	1.49 (4 rolls)
	$Q = 2025$	1	1

Figure 5.6: U component of the velocity variations at $Q = 0$ and $Q = 400$, $Ra = 15000$, $Pr = 0.05$, $16 \times 16 \times 21$ resolution, $x = L_x/4$, $y = L_y/4$ and $z = 0.6941$ with aspect ratio $\Gamma [3 : 1.5]$.
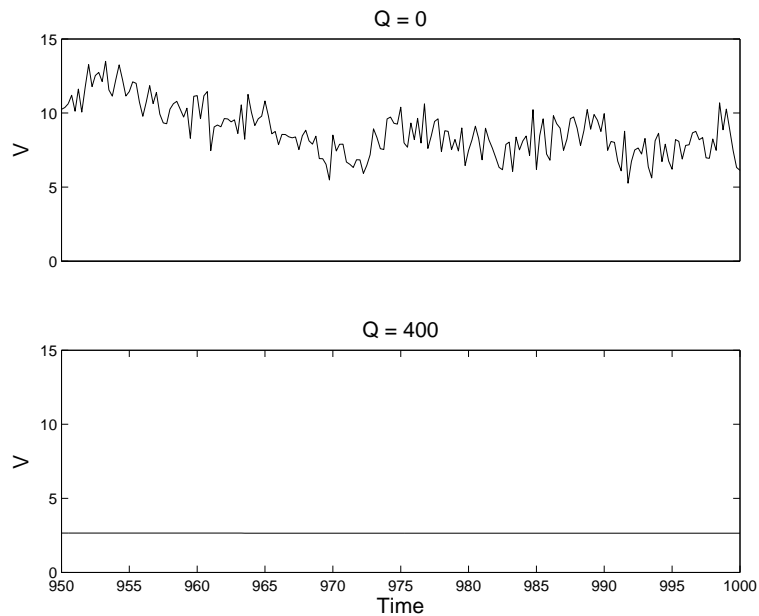

Figure 5.7: V component of the velocity variations at $Q = 0$ and $Q = 400$, $Ra = 15000$, $Pr = 0.05$, $16 \times 16 \times 21$ resolution, $x = L_x/4$, $y = L_y/4$ and $z = 0.6941$ with aspect ratio $\Gamma [3 : 1.5]$.
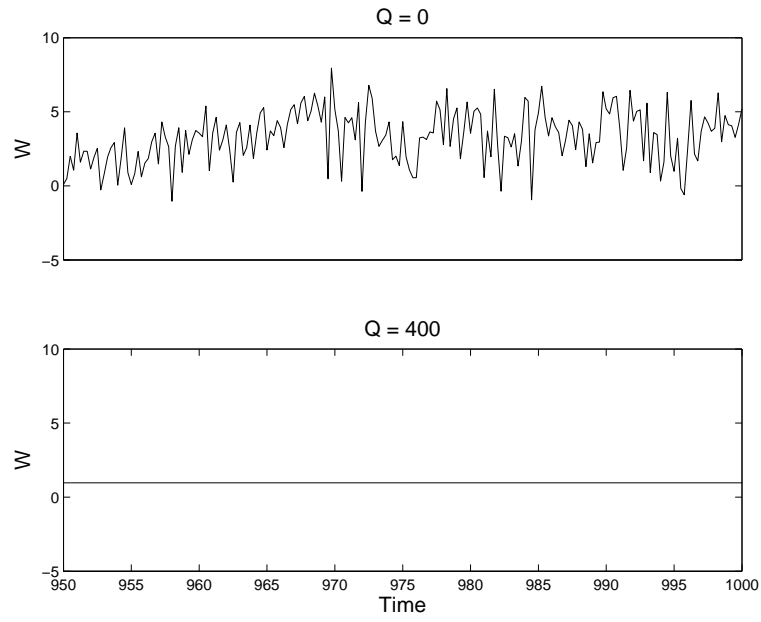
56

Figure 5.8: W component of the velocity variations at $Q = 0$ and $Q = 400$, $Ra = 15000$, $Pr = 0.05$, $16 \times 16 \times 21$ resolution, $x = L_x/4$, $y = L_y/4$ and $z = 0.6941$ with aspect ratio Γ [3 : 1.5].
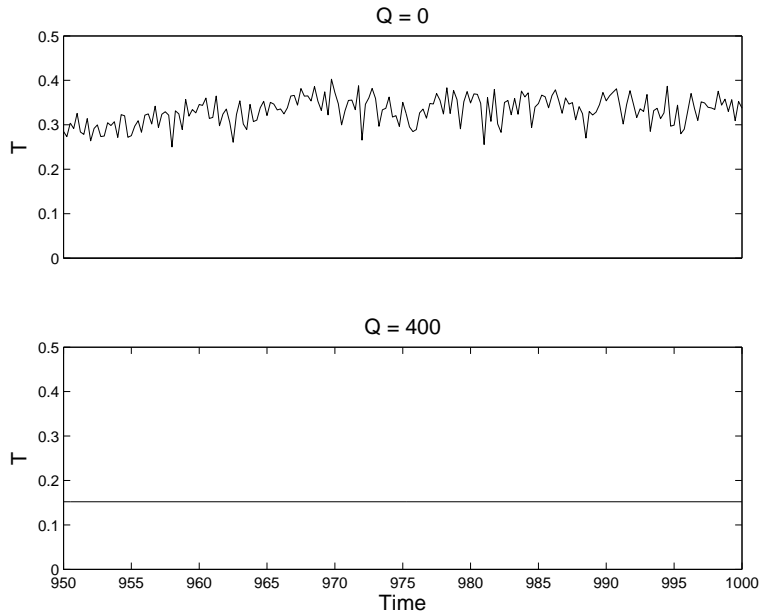

Figure 5.9: Temperature variations at $Q = 0$ and $Q = 400$, $Ra = 15000$, $Pr = 0.05$, $16 \times 16 \times 21$ resolution, $x = L_x/4$, $y = L_y/4$ and $z = 0.6941$ with aspect ratio Γ [3 : 1.5].
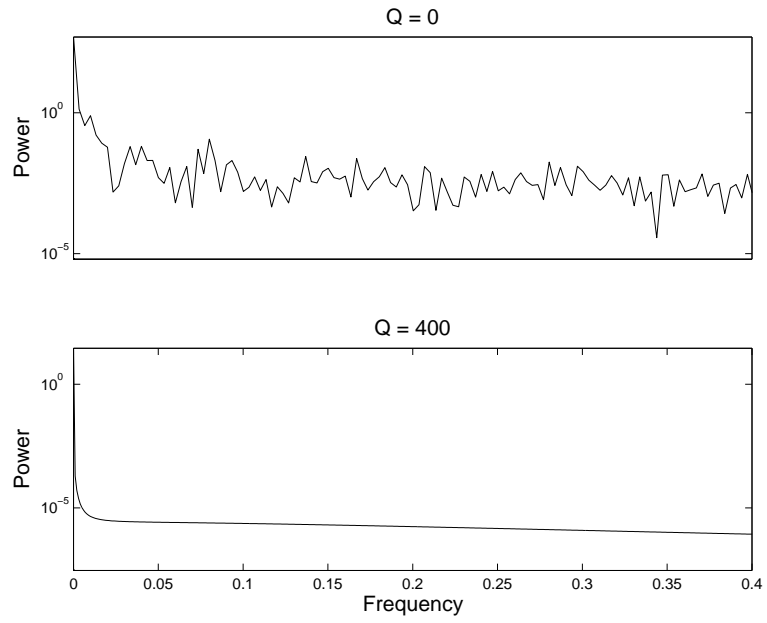
Figure 5.10: Power spectrum of V velocity at $Q = 0$ and $Q = 400$, $Ra = 15000$, $Pr = 0.05$, $16 \times 16 \times 21$ resolution, $x = L_x/4$, $y = L_y/4$ and $z = 0.6941$ with aspect ratio Γ [3 : 1.5].
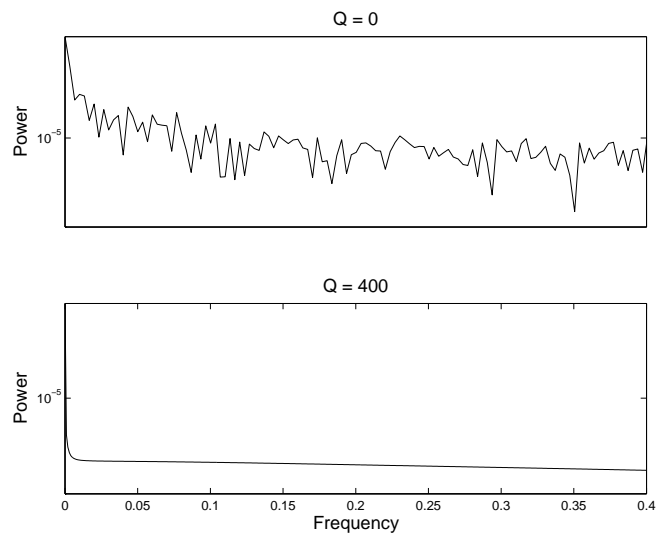

Figure 5.11: Power spectrum of T temperature at $Q = 0$ and $Q = 400$, $Ra = 15000$, $Pr = 0.05$, $16 \times 16 \times 21$ resolution, $x = L_x/4$, $y = L_y/4$ and $z = 0.6941$ with aspect ratio Γ [3 : 1.5].
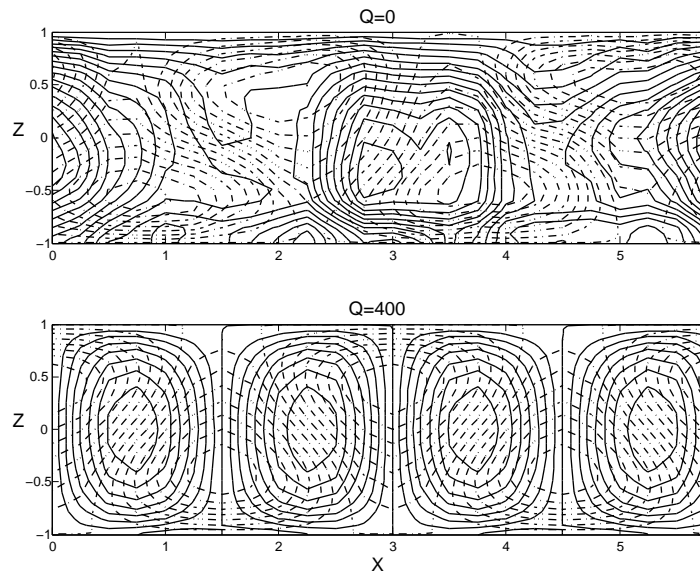
Figure 5.12: The solid lines shows the stream function of the velocity fields and dashed lines shows the temperature contours for $Ra = 15000$ at $Pr = 0.05$ with aspect ratio $\Gamma\,[3:1.5]$. The pattern on the top at $Q = 0$ and on the bottom at $Q = 400$

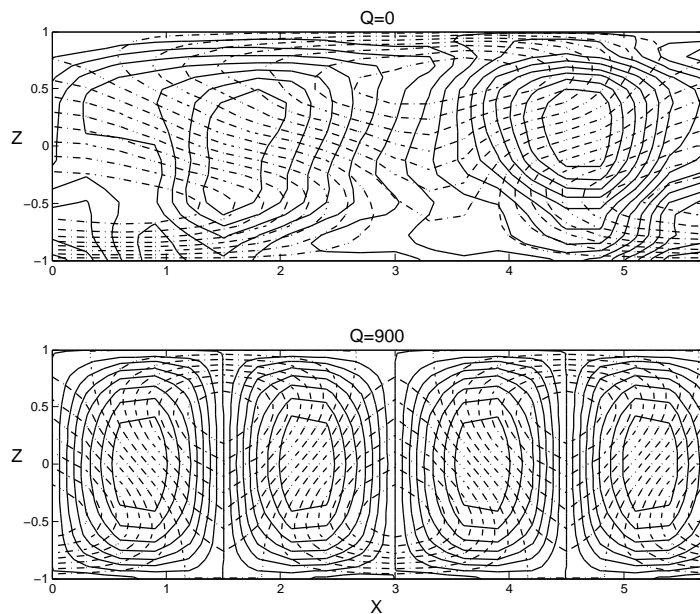
Figure 5.13: The solid lines shows the stream lines of the velocity fields and dashed lines shows the temperature contours for $Ra = 30000$ at $Pr = 0.05$. The pattern on the top at $Q = 0$ and on the bottom at $Q = 900$.
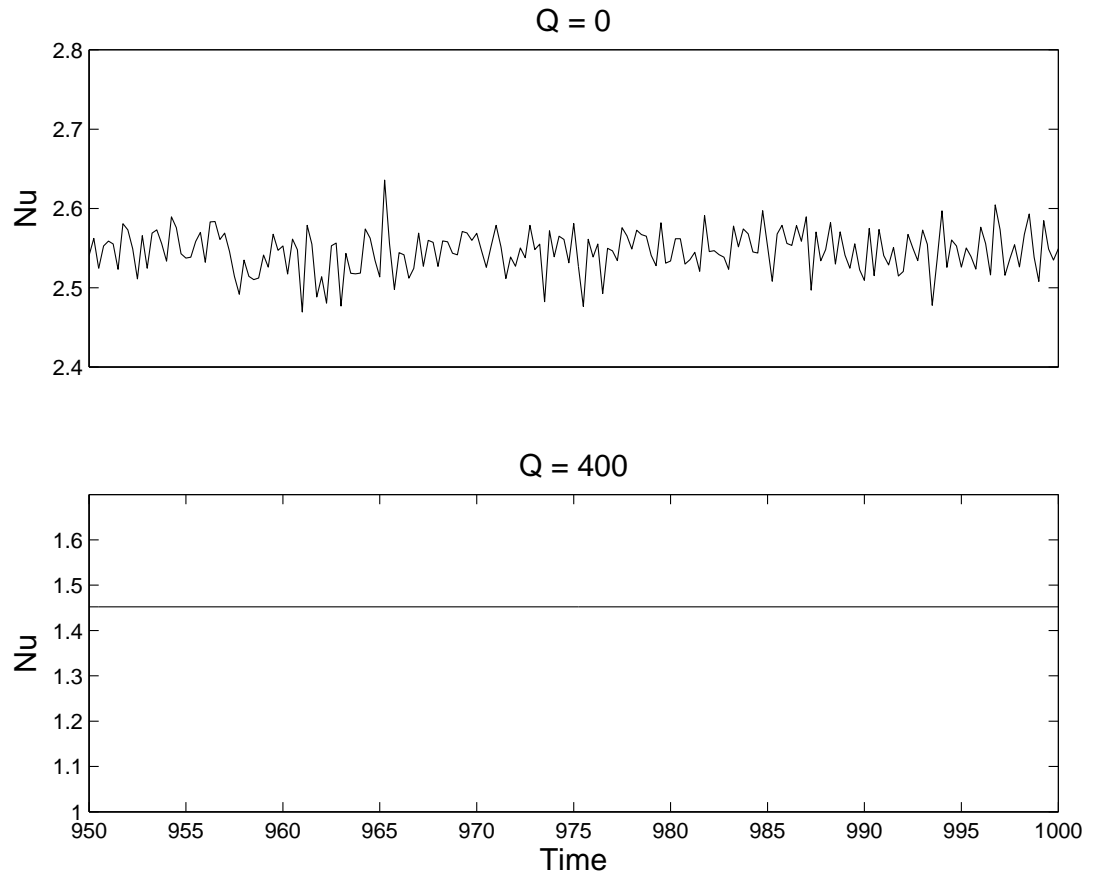
Figure 5.14: Nusselt number variations in time at $Q = 0$ and $Q = 400$, $Ra = 15000$, $Pr = 0.05$, $16 \times 16 \times 21$ resolution with aspect ratio Γ [3 : 1.5].

Further numerical experiments are performed to study the effects of varying magnetic field strength (Q) on the convective heat transport efficiency indicated by Nusselt number (Nu) at selected Rayleigh number (Ra) values. A liquid metal with $Pr = 0.05$ is selected in a layer with aspect ratio $\Gamma[3 : 1.5]$ and subjected to a vertical magnetic field. The computation is started with the flow field just supercritical obtained using the eigenfunctions of the linear stability study. It is known that application of a vertical magnetic field suppresses the convective motions as shown in Figure 5.15 by decreasing Nu values as Q increases, ultimately approaching to the conductive state with $Nu = 1$. In the process, kinks appear at $Q = 1400$ for $Ra = 30000$, at $Q = 2500$ for $Ra = 50000$ and at $Q = 3600$ for $Ra = 80000$. The kinks coincide with the increase in the number of rolls and thus decrease in the wavelength. This is also observed and discussed in an earlier numerical study [37]. This change in the roll pattern is shown in Figure 5.16 when $Q = 2250$ is increased to $Q = 3000$ for $Ra = 50000$ at the transient stages $t = 0, 30, 65$. All these runs are in the steady roll motion regime and use a typical dimensionless time step between 10^{-3} and 10^{-4}.
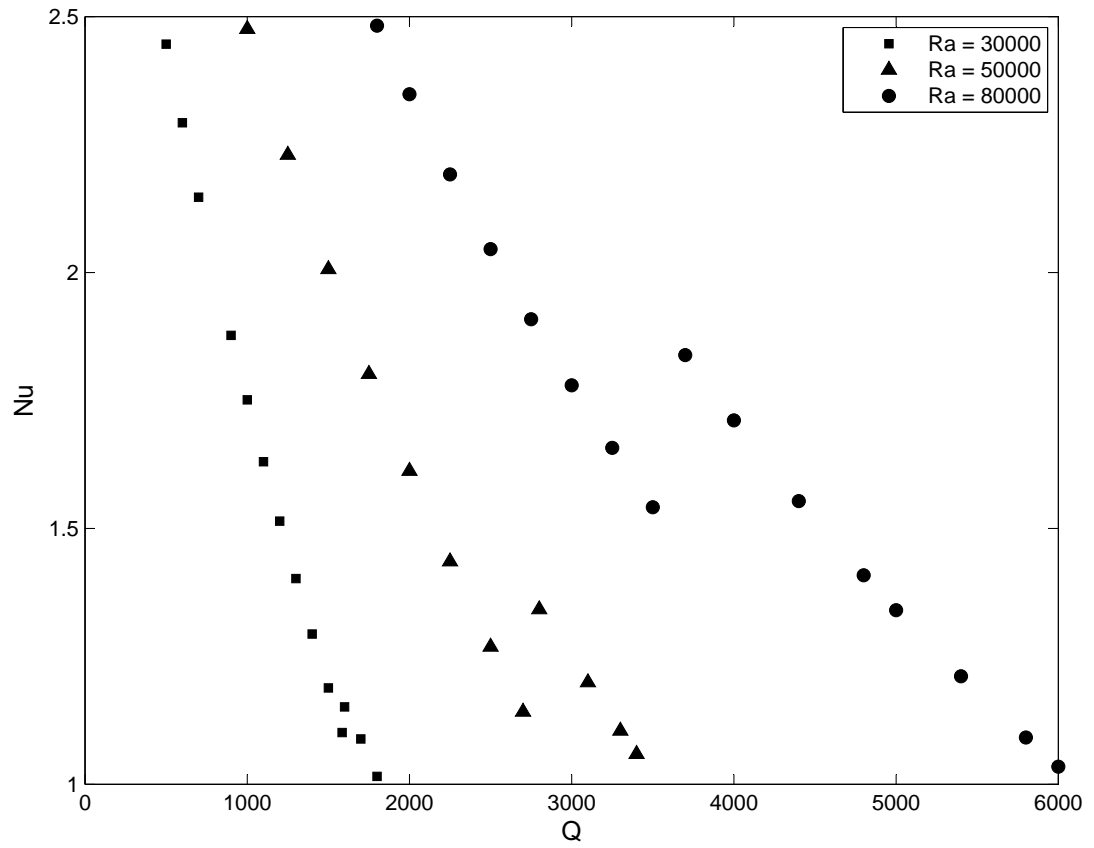
Figure 5.15: Nusselt number, *Nu* versus Chandrasekhar number, *Q* for *Pr* = 0.05 with aspect ratio Γ [3 : 1.5].
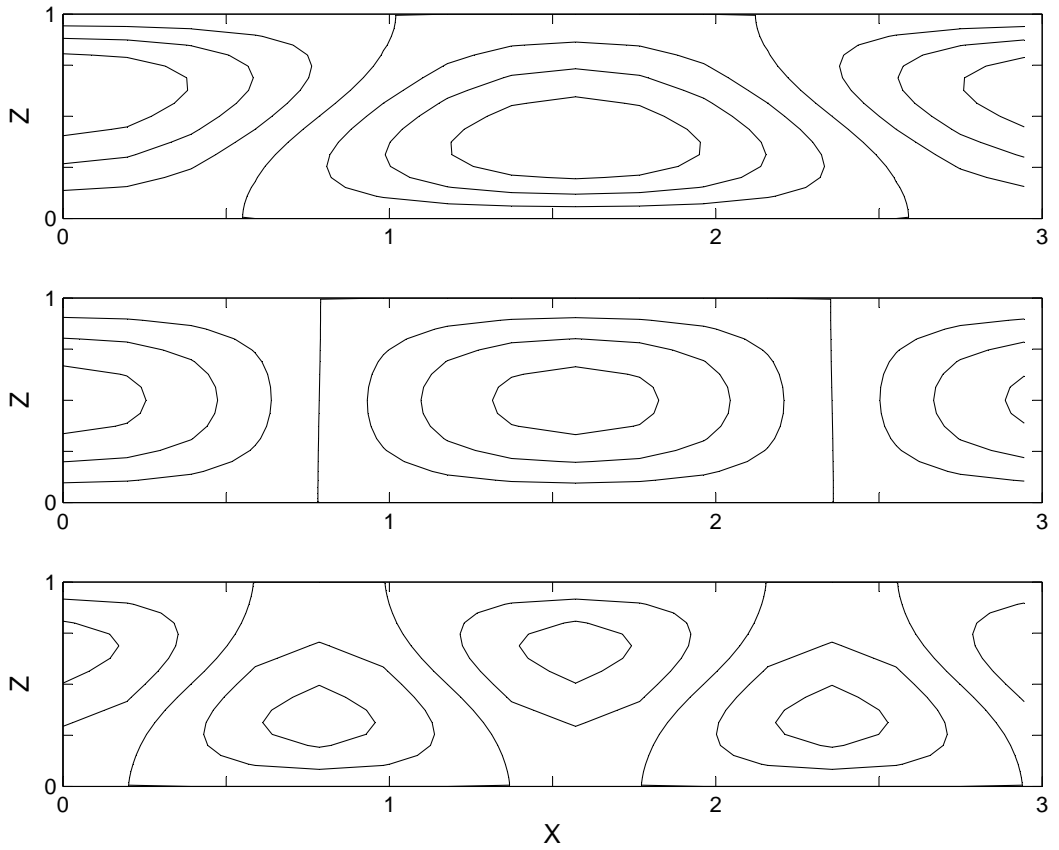
Figure 5.16: Temperature contour in the *xz* plane during the stages *t* = 0, 30, 60 of restructuring when initially *Q* = 2500 is suddenly set to 3000 at *Ra* = 50000, *Pr* = 0.05 with aspect ratio Γ [3 : 1.5].

5.3.2 Time Dependent Flows

In this section, we discuss the effects of the the strong magnetic field Q in the vertical direction on the thermal convection. The Rayleigh number range over the critical value is examined for the impact on heat transport. The results are compared with study of Busse and Clever [19]. In that paper, thermal convection in a fluid layer heated from below is solved numerically in the case of strong vertical magnetic field permeating the convective layer. In [19], spatially periodic solutions in the x and y-directions are assumed and the dependent variables in the z-direction are expanded in a complete system of functions satisfying the boundary conditions. The resulting nonlinear system reduced from the model equations using Galerkin projection is solved using Newton-Raphson method. They observe that for a given horizontal spatial period, the heat transport decreases with increasing Rayleigh number for steady three-dimensional convective flow as well as for time periodic forms of convection. The stability limits of different flow regimes such as stationary, time periodic, etc., are shifted to higher Rayleigh numbers and as the severity of the magnetic field grows, the characteristic time scales are reduced.

In order to compare the result with Busse and Clever [19], $Pr = 0.01$ and $Q = 2000$ and aspect ratio Γ [1.5 : 1] are chosen. As shown in Figure 5.17, the heat transport and poloidal kinetic energy at $Ra = 31000$ show an upward trend and then suddenly decrease with increasing Rayleigh number for steady two-dimensional convective flow as well as for time periodic flows as also observed by Busse and Clever [19]. As the Rayleigh number is further increased to $Ra = 35500$, it is observed that time periodic flow shifts to stationary flow and the heat transport and poloidal kinetic energy begin to rise.

The toroidal component of the kinetic energy appears for $Ra \geq 31500$ that is the underlaying flow contains vertical vorticity component and thus no longer two dimensional. Since the study is performed just above the marginal stability curve corresponding to $Q = 2000$, toroidal values are too small, that is smaller than 10^{-3} and thus it can be considered as noise except those at $Ra = 31500$ and $Ra = 35000$ which are significant. And then at $Ra \geq 35500$, toroidal energy disappears again and we observe two-dimensional steady flow. This situation is supported by the plots of temperature and velocity field in the xy plane for $Ra = 31000 - 3600$ in Figures 5.23 - 5.28. At $Ra = 31000$ the flow is in the form of stationary two dimensional roll motion that means that in the xy plane only parallel lines appear. Otherwise, as in Figures

5.24 - 5.27), the parallel lines disappear and the flow becomes three dimensional.

The power spectrum for $Ra = 32000 - 34500$ are shown in Figure 5.18. Periodic flow regime is observed at Rayleigh numbers in this interval. The power spectrum for periodic $Ra = 32500$ and $Ra = 33500$ are examined and the discrete frequencies are identified in Figures 5.19 and Figure 5.21 respectively. As in Nusselt number, decline in the frequency values is observed as Rayleigh number is increased in this range.

As Rayleigh number is increased, the time series of temperature variation are plotted in Figures 5.29 and 5.30 at $Q = 2000$. Since the flow is steady at $Ra = 31000$, no fluctuations are observed. When toroidal component is present in the flow, a periodic signal is observed as in Figure 5.29 for $Ra = 32000$. A further increase in the Rayleigh number results in more intensive temporal variation up to $Ra = 35000$. As the Rayleigh number is further increased to $Ra = 35500$, it is observed that time periodic flow shifts to stationary flow and the heat transport and poloidal kinetic energy begin to rise due to the strong magnetic field effects on the flow. The flow does not break down the suppressing effect of the strong magnetic field and stay on the steady region up to $Ra = 63000$. At $Ra = 63500$ flow shows periodic behavior and at $Ra = 65000$ transient to the chaotic region.
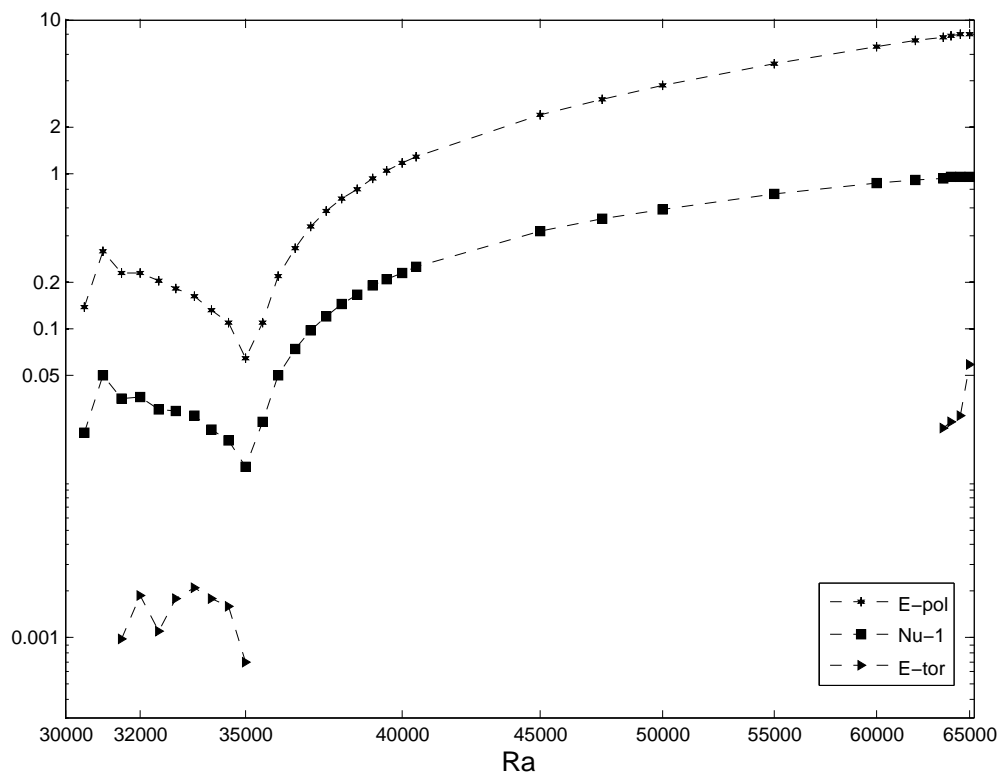
Figure 5.17: Toroidal component of the kinetic energy E_{tor}, poloidal component of kinetic energy E_{pol} and time averaged values of Nusselt number at $\Gamma[1.5:1]$, $Pr = 0.01$ and $Q = 2000$.
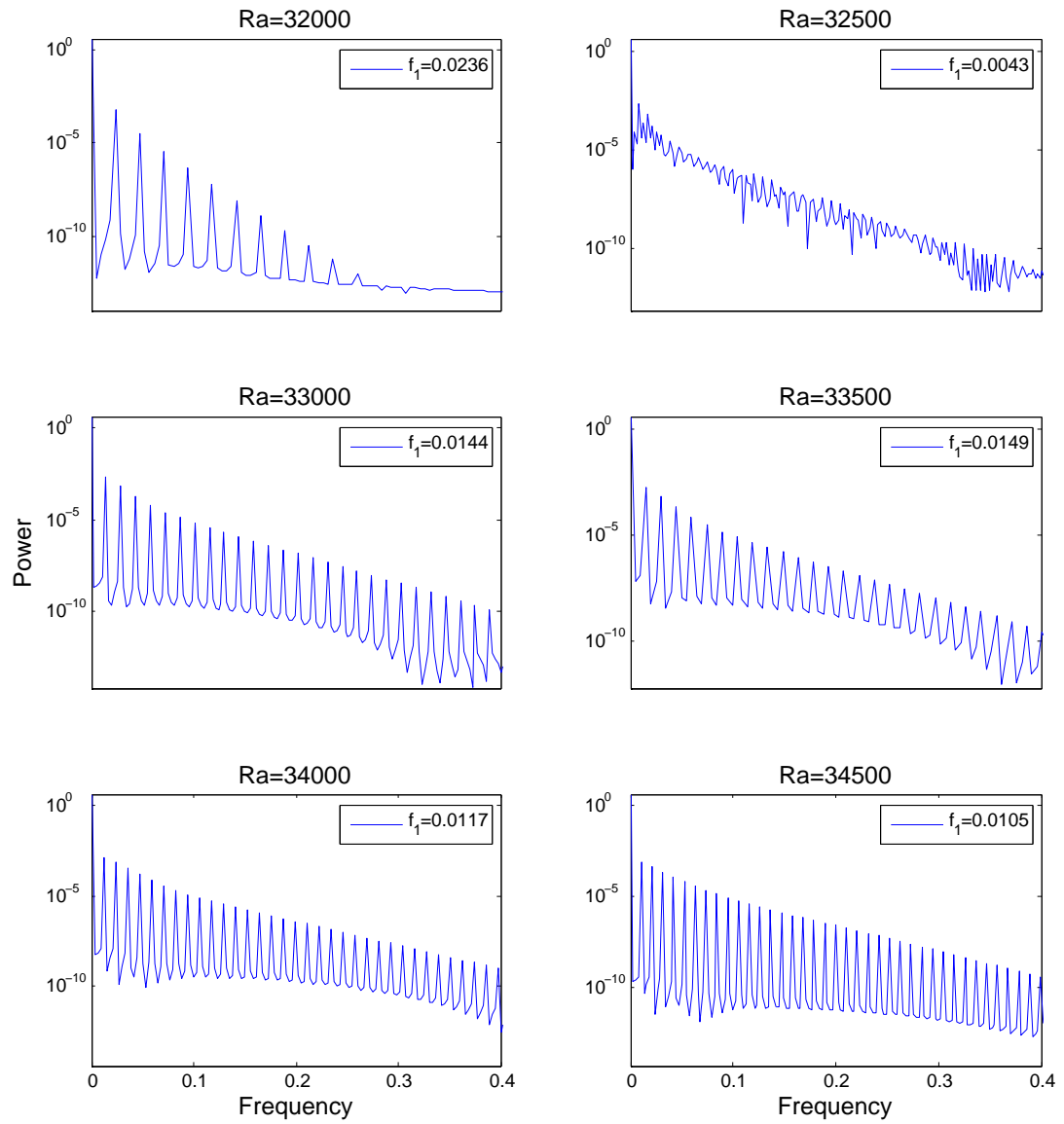
Figure 5.18: Power spectrum on periodic regions for $\Gamma\,[1.5:1]$, $Pr = 0.01$ and $Q = 2000$.

Figure 5.19: Power spectrum on periodic region at $Ra = 32500$ for $\Gamma[1.5:1]$, $Pr = 0.01$ and $Q = 2000$.

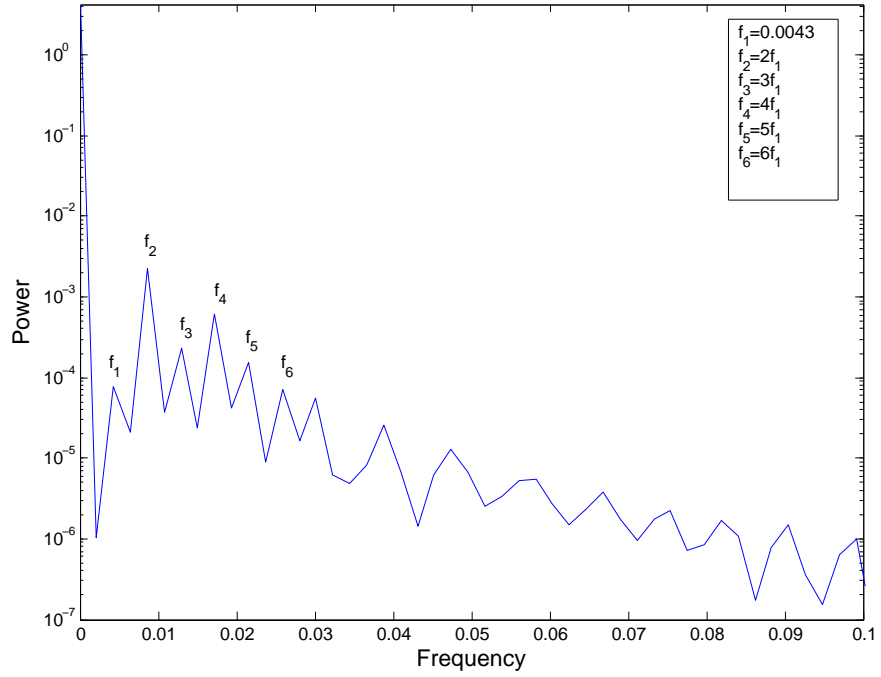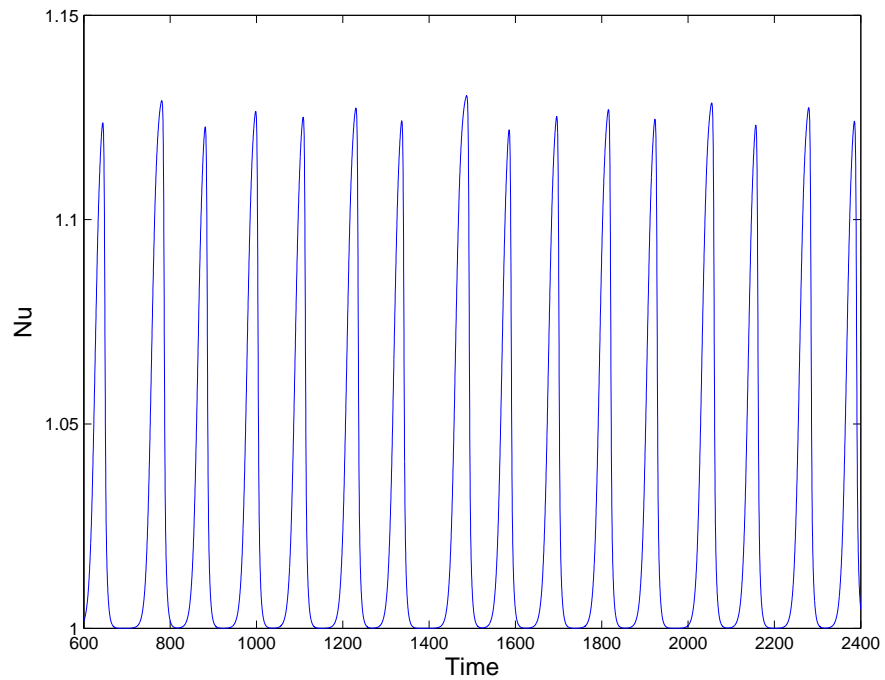Figure 5.20: Nusselt number versus time at $Ra = 32500$ for $\Gamma[1.5:1]$, $Pr = 0.01$ and $Q = 2000$.

68
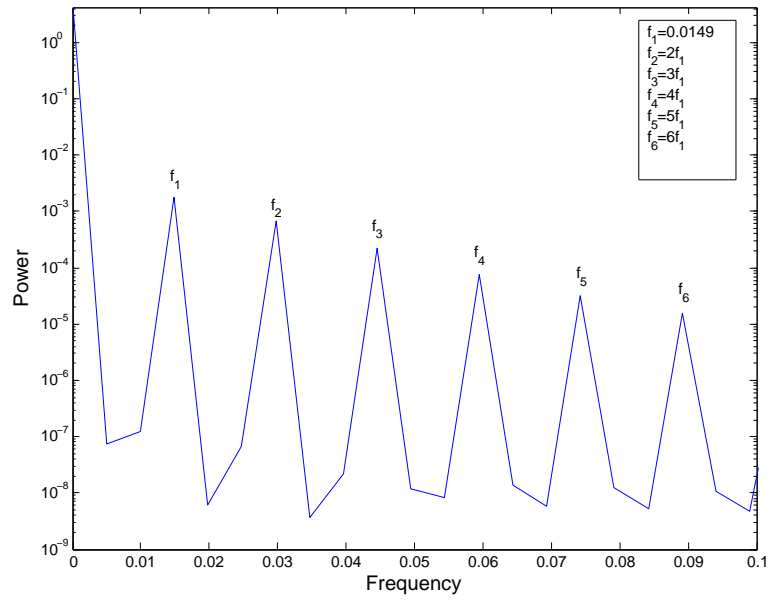
Figure 5.21: Power spectrum on periodic region at $Ra = 33500$ for $\Gamma\,[1.5:1]$, $Pr = 0.01$ and $Q = 2000$.
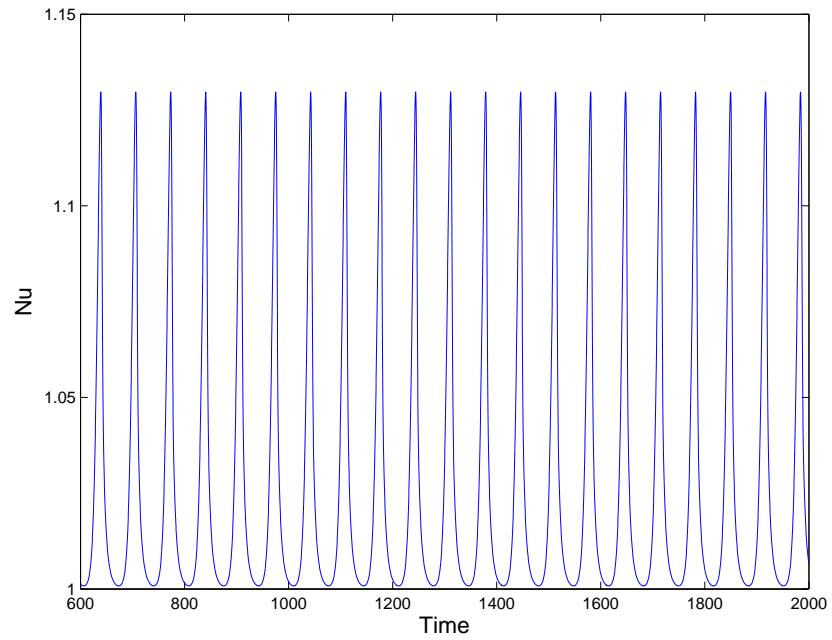
Figure 5.22: Nusselt number versus time at $Ra = 33500$ for $\Gamma\,[1.5:1]$, $Pr = 0.01$ and $Q = 2000$.

Figure 5.23: Velocity field and temperature contour for $Ra = 31000$ at $z = 0.7723$, $\Gamma[1.5 : 1]$, $Pr = 0.01$ and $Q = 2000$. Here, arrows shows the velocity field, solid lines indicate the temperature contour.
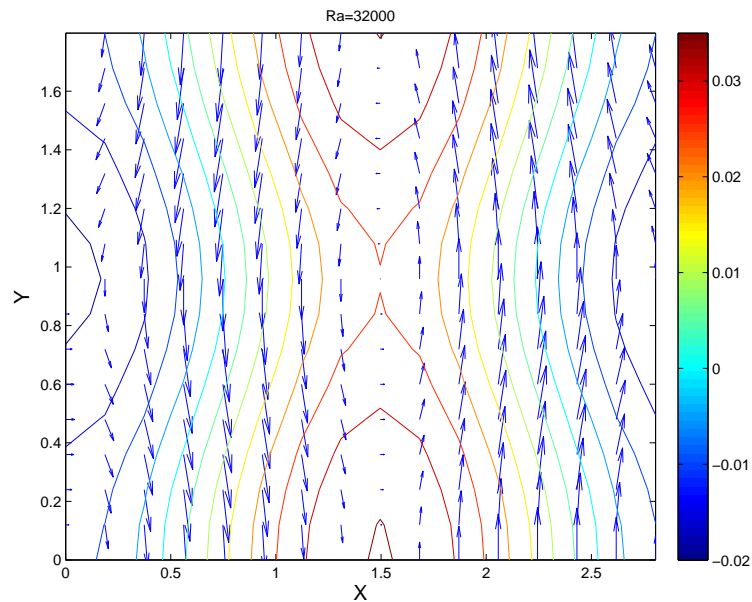
Figure 5.24: Velocity field and temperature contour for $Ra = 32000$ at $z = 0.7723$, $\Gamma[1.5 : 1]$, $Pr = 0.01$ and $Q = 2000$. Here, arrows shows the velocity field, solid lines indicate the temperature contour.
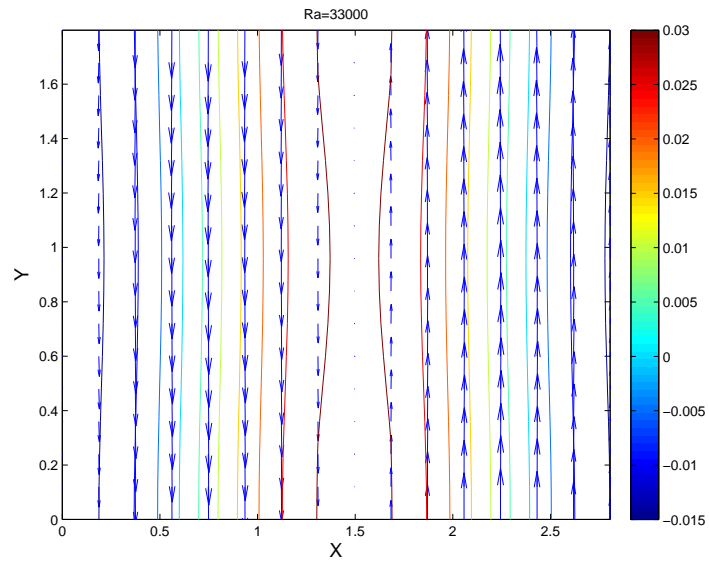
Figure 5.25: Velocity field and temperature contour for Ra = 33000 at z = 0.7723, Γ [1.5 : 1], Pr = 0.01 and Q = 2000. Here, arrows shows the velocity field, solid lines indicate the temperature contour.
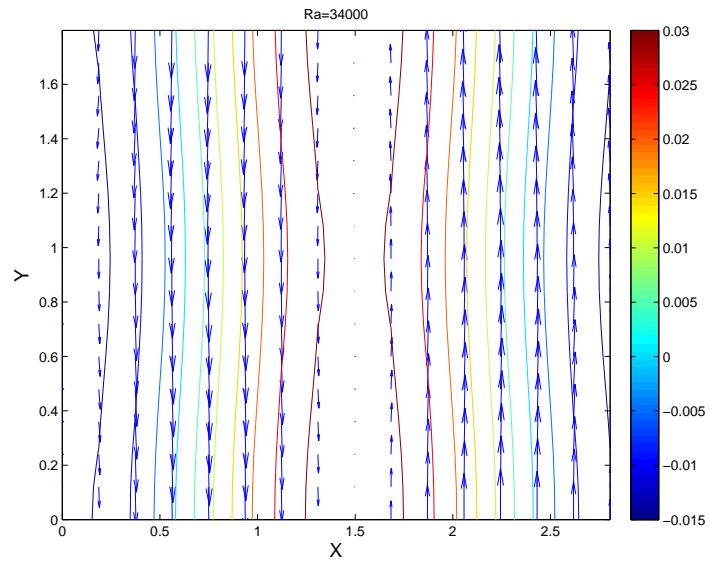
Figure 5.26: Velocity field and temperature contour for Ra = 34000 at z = 0.7723, Γ [1.5 : 1], Pr = 0.01 and Q = 2000. Here, arrows shows the velocity field, solid lines indicate the temperature contour.
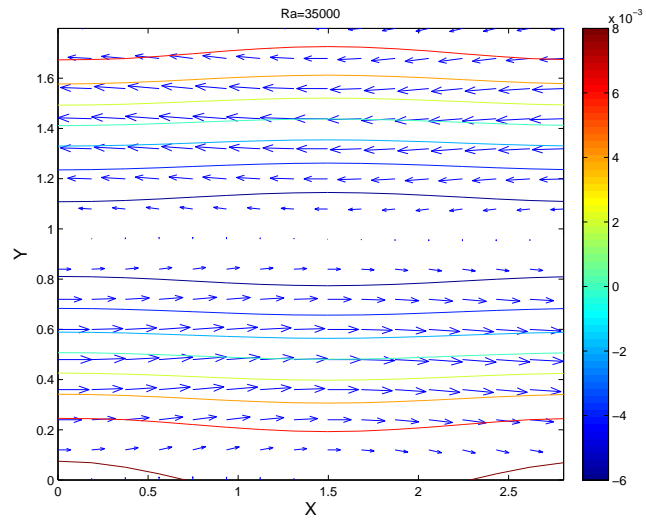
Figure 5.27: Velocity field and temperature contour for $Ra = 35000$ at $z = 0.7723$, $\Gamma [1.5 : 1]$, $Pr = 0.01$ and $Q = 2000$. Here, arrows shows the velocity field, solid lines indicate the temperature contour.
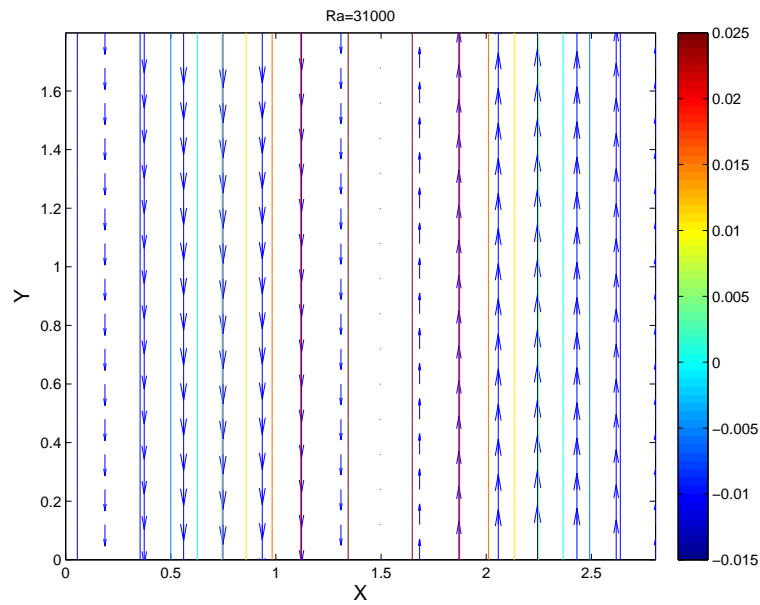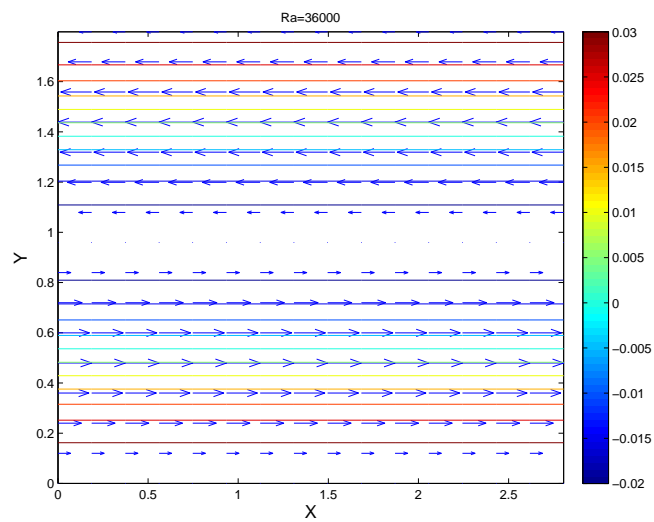

Figure 5.28: Velocity field and temperature contour for $Ra = 36000$ at $z = 0.7723$, $\Gamma [1.5 : 1]$, $Pr = 0.01$ and $Q = 2000$. Here, arrows shows the velocity field, solid lines indicate the temperature contour.
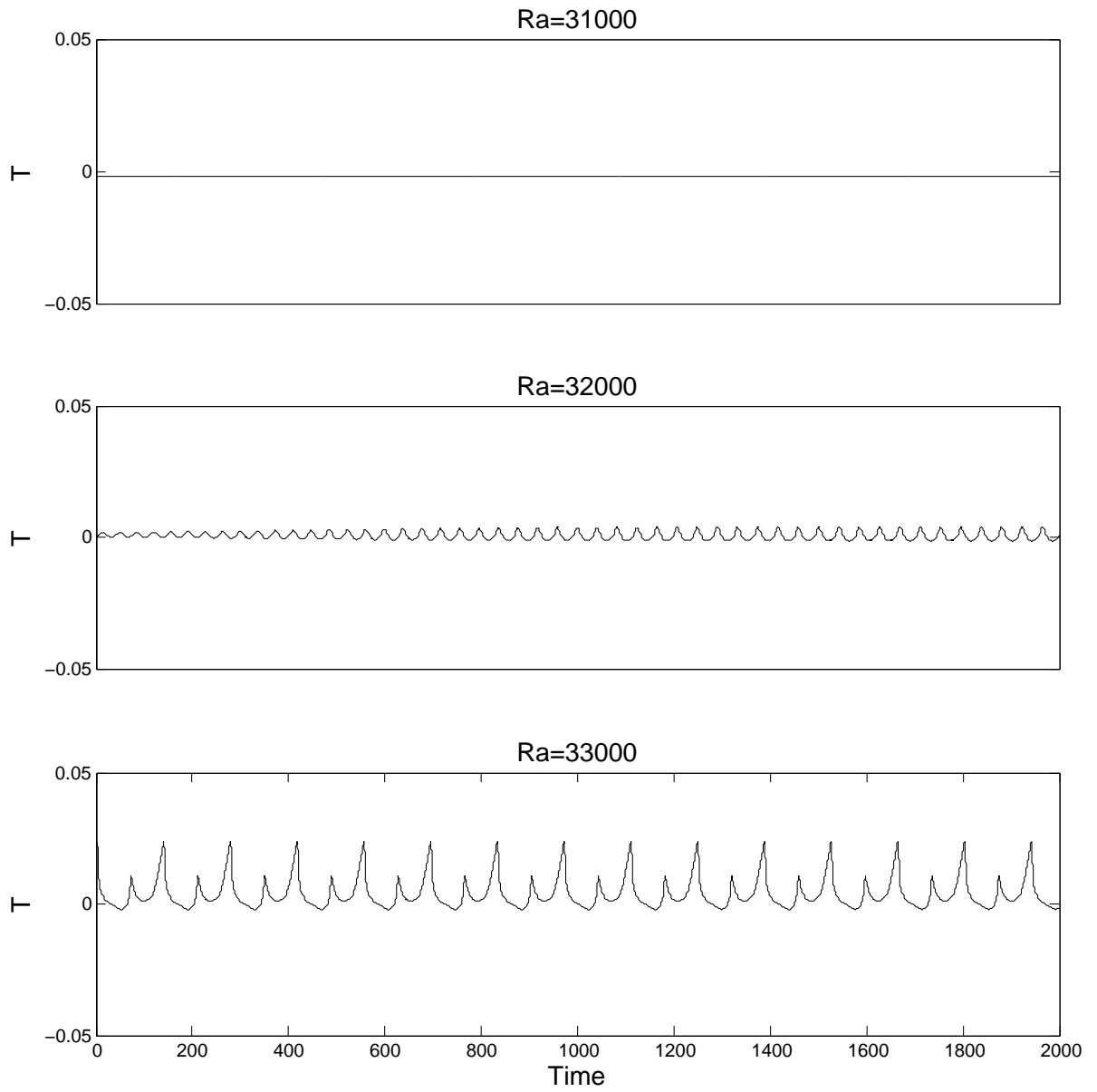
Figure 5.29: Temperature variations at $Ra = 31000$ - $Ra = 33000$, $Q = 2000$, $Pr = 0.05$, $16 \times 16 \times 21$ resolution, $x = L_x/4$, $y = L_y/4$ and $z = 0.6941$.
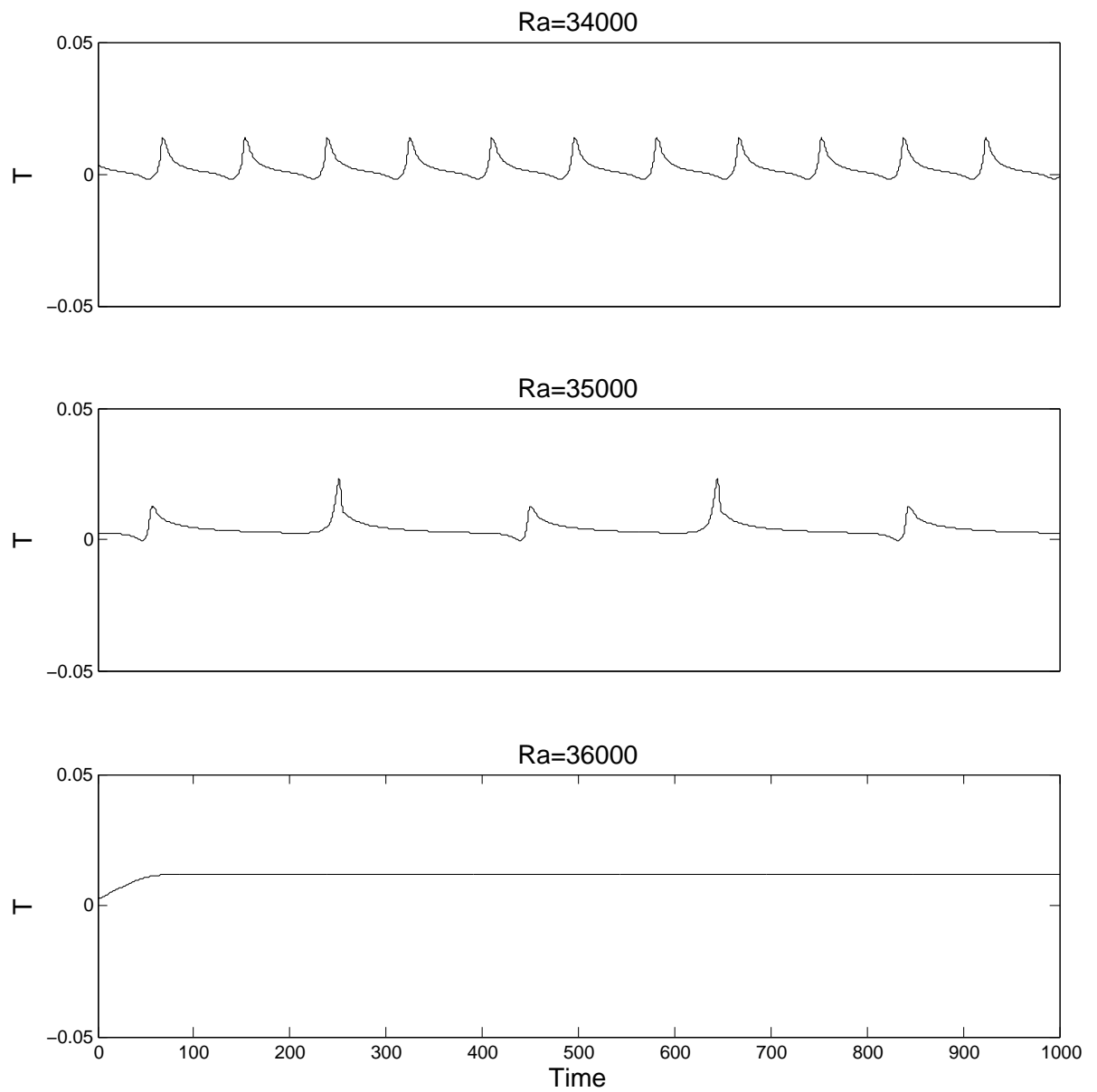
Figure 5.30: Temperature variations at $Ra = 34000$ - $Ra = 36000$, $Q = 2000$, $Pr = 0.05$, $16 \times 16 \times 21$ resolution, $x = L_x/4$, $y = L_y/4$ and $z = 0.6941$.

74

The presented results are also compared with the experimental data generated by Aurnou and Olson in [36]. In that study, small Prandtl number fluid (liquid gallium, $Pr = 0.023$) is used in a large convection tank with aspect ratio Γ [8 : 8]. The experimental data for Nusselt number in supercritical magnetoconvection regime is shown to fit the following power law:

$$Nu = 0.23(Q^{-1}Ra)^{0.50\pm0.03} \quad \text{for} \quad Q = 670 \quad \text{with} \quad Q^{-1}Ra > 25. \quad\quad (5.33)$$

This power law in 5.33 is derived using simple scaling arguments which was formulated by the basic force balance between buoyancy and the Lorentz force in regards to heat transport. However, no upper bound of validity of this law is given in the experimental study of Aurnou and Olson [36].

We performed a numerical study at various spatial and temporal resolutions for the same flow parameters that are used in the experimental study [36]. Sequare box with aspect ratio of Γ [0.8 : 0.8] are chosen due to the computaion cost.

In Figure 5.31 a logarithmic plot of Nusselt number versus $(Q^{-1}Ra)^{0.50}$ is plotted for increasing Rayleigh number at a fixed Chandrasekhar number $Q = 670$ in the range of $Q^{-1}Ra > 25$. At $Ra = 17420$ and $Ra = 20100$ the underlying flow is steady and at $Ra = 23450$ it is periodic, that is, the toroidal component is present in the flow (Figure 5.32). Beyond the value of $Ra = 30150$, chaotic motions are observed. In Figure 5.33, increasing complexity of flow is observed in plots in the xy plane as Rayleigh number is increased. It is observed in Figure 5.31 that the calculated numerical results stay in the range specified by the power law up to $Ra = 36800$ only. This may be a the upper bound for the validity of the power law.
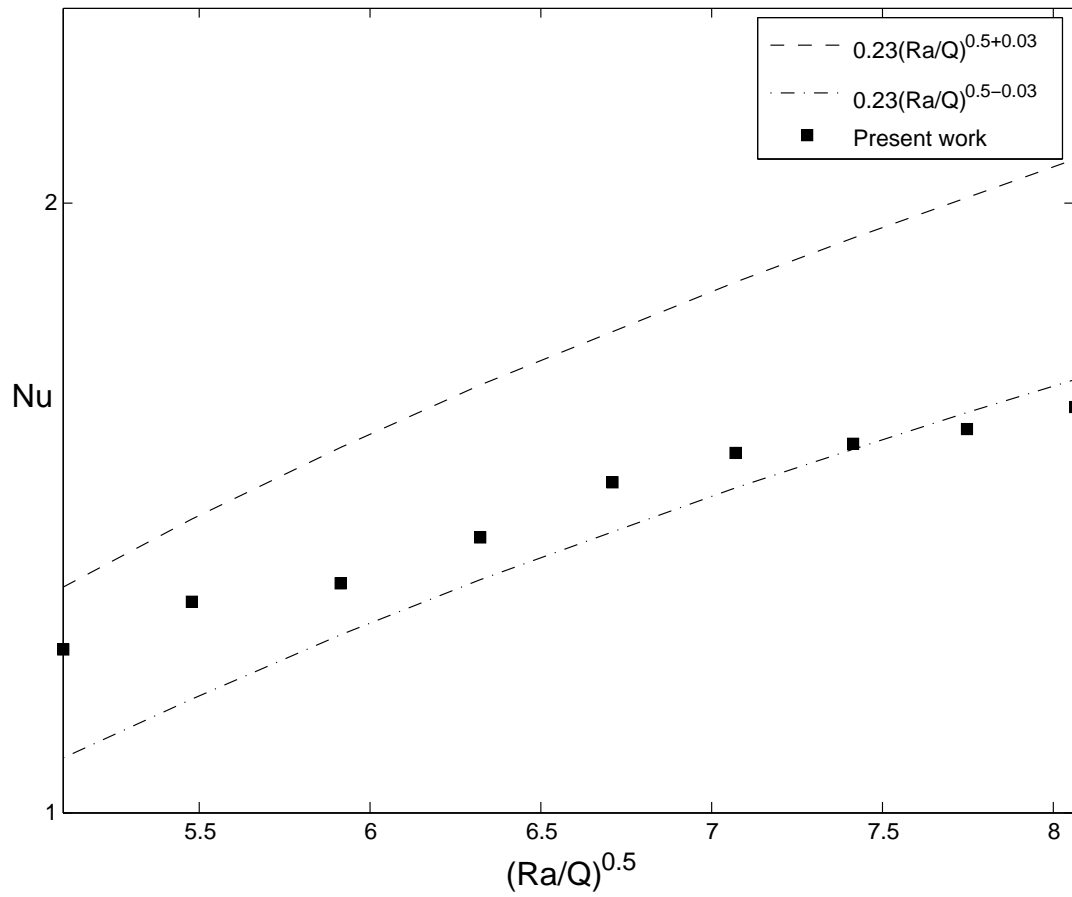
Figure 5.31: Nu versus $(Q^{-1}Ra)^{0.50}$ in logarithmic scale at $Pr = 0.023$, $\Gamma[0.8:0.8]$ and $Q = 670$.
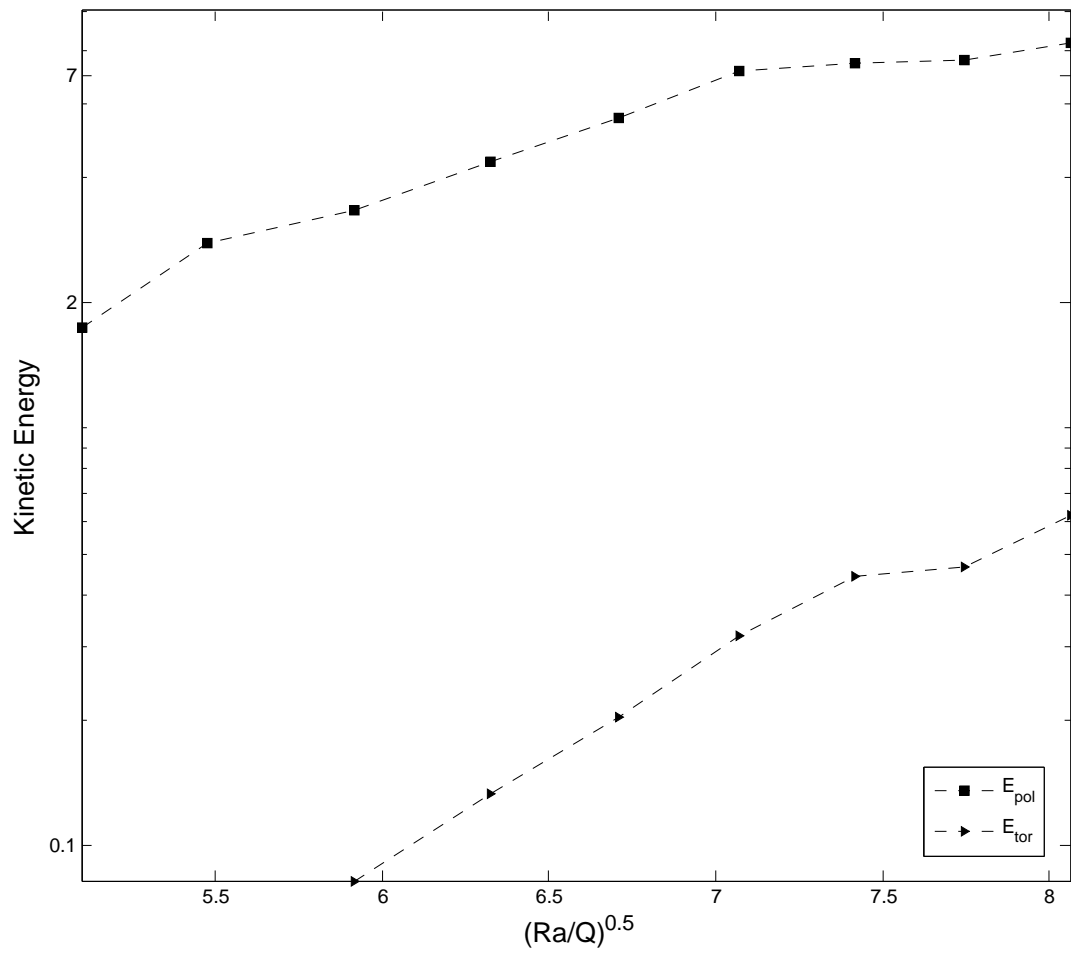
Figure 5.32: Poloidal and toroidal kinetic energy versus Rayleigh number for vertical magnetic field at $Pr = 0.023$, Γ [0.8 : 0.8] and $Q = 670$.
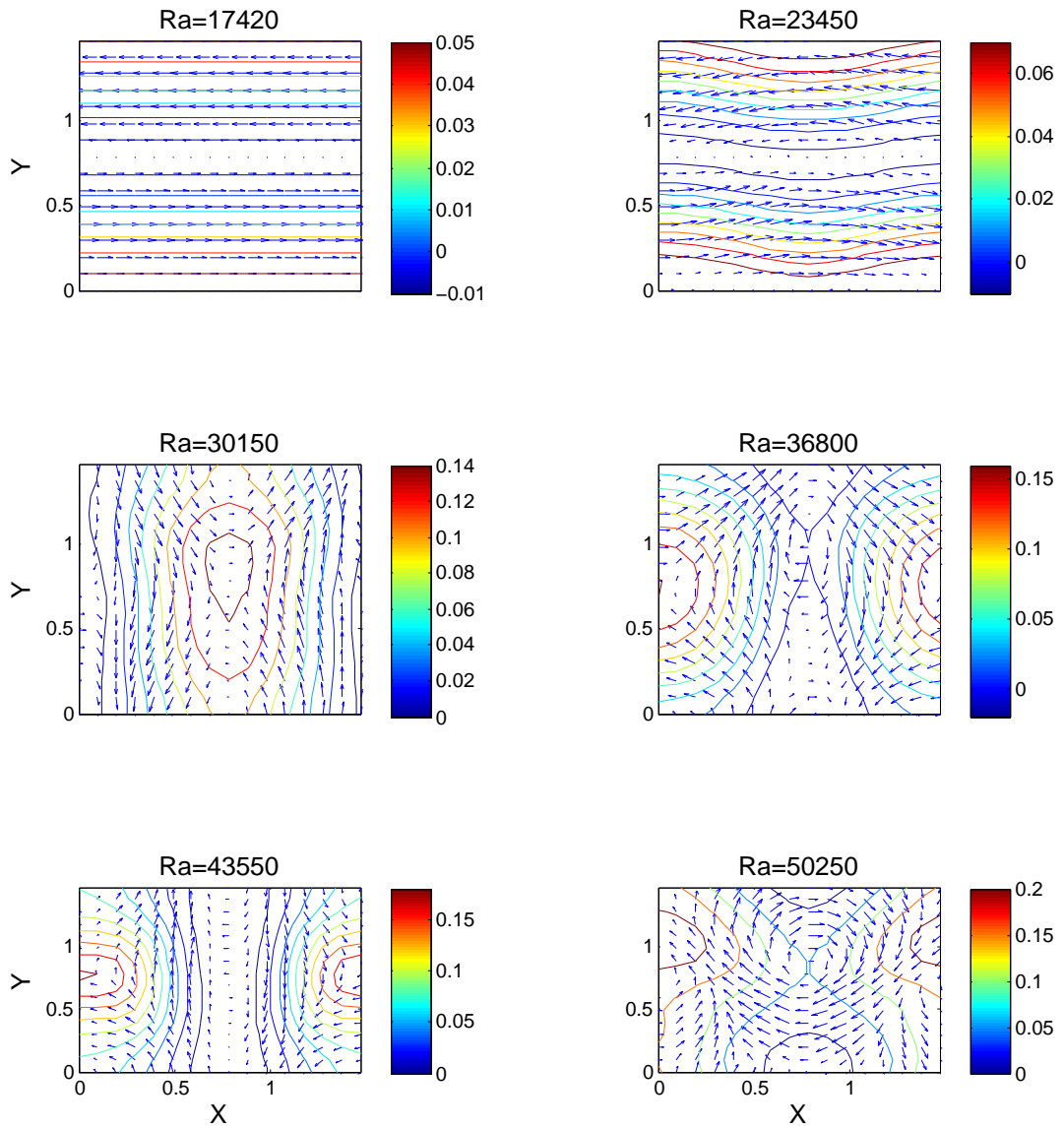
Figure 5.33: Velocity field and temperature contour on *xy* plane at *z* = 0.796, Γ [0.8 : 0.8], *Pr* = 0.023, and *Q* = 670. Here, arrows shows the velocity field, solid lines indicate the temperature contour.

CHAPTER 6

THERMAL CONVECTION UNDER OBLIQUE MAGNETIC FIELD

In the previous chapter, a periodic horizontal layer between conducting plates that are heated from below under the influence of a uniform vertical magnetic field is discussed and as mentioned in the literature, the inhibition effect on an electrically conducting fluid is observed. In this section, the convective flow under the influence of a oblique magnetic field is studied as both vertical and horizontal components of a magnetic field are present.

6.1 Linear Stability Analysis

We consider the linear stability of the conductive (no-motion) state under an oblique magnetic field that leads to critical Rayleigh values when the convective motion just sets in. At this point, the velocity and temperature perturbations over the conductive state are small, so that the nonlinear terms in the governing equations (2.33) and (2.34) can be linearized around no-motion state to get the residual equations:

$$R_{\mathbf{u}} = -\frac{\partial \mathbf{u}}{\partial t} - \nabla\Pi + PrRa_h\Theta\mathbf{e}_z + Pr\nabla^2\mathbf{u} + Q_hPr\left(Cos\chi\partial y + Sin\chi\partial z\right)\mathbf{b}, \qquad (6.1)$$

$$R_{\Theta} = -\frac{\partial\Theta}{\partial t} - \frac{w}{2} + \nabla^2\Theta. \qquad (6.2)$$

after introduction of truncated representations of the flow variables in terms of the corresponding bases (4.3), (4.4) and (4.5). Vanishing Galerkin projection of these residuals in the space spanned by the dual bases yields

$$\int_0^{L_x}\int_0^{L_y}\int_{-1}^1 \bar{V}\cdot R_{\mathbf{u}}\,dz = \int_0^{L_x}\int_0^{L_y}\int_{-1}^1 \bar{V}\cdot\left[-\frac{\partial\mathbf{u}}{\partial t} - \nabla\Pi + PrRa_h\Theta e_z\right]dxdydz \quad +$$

$$\int_0^{L_x} \int_0^{L_y} \int_{-1}^{1} \bar{V} \cdot \left[Pr\nabla^2 \mathbf{u} + Q_h Pr \left(Cos\chi \partial y + Sin\chi \partial z \right) \mathbf{b} \right] dxdydz = 0 \qquad (6.3)$$

$$\int_0^{L_x} \int_0^{L_y} \int_{-1}^{1} \bar{T} R_\Theta \, dz = \int_0^{L_x} \int_0^{L_y} \int_{-1}^{1} \bar{T} \left[-\frac{\partial \Theta}{\partial t} - \frac{w}{2} + \nabla^2 \Theta \right] dxdydz = 0. \qquad (6.4)$$

And, for this general case the system matrices (5.21) can be expanded to the following form:

$$\underbrace{\begin{bmatrix} \left(\bar{V}_q^{(1)}, V_p^{(1)} \right) & 0 & 0 \\ 0 & \left(\bar{V}_q^{(2)}, V_p^{(2)} \right) & 0 \\ 0 & 0 & \left(\bar{T}_q, T_p \right) \end{bmatrix}}_{Mass-Matrix} \begin{bmatrix} \dot{a}_p^{(1)} \\ \dot{a}_p^{(2)} \\ \dot{b}_p \end{bmatrix} =$$

$$Pr \underbrace{\begin{bmatrix} \left(\bar{V}_q^{(1)}, (-\gamma^2 + \mathbb{D}^2) V_p^{(1)} \right) + & & \\ \left(\bar{V}_q^{(1)}, Q_h \left(Cos\chi \eta_m i + Sin\chi \mathbb{D} \right) B_p^{(1)} \right) & 0 & 0 \\ 0 & \left(\bar{V}_q^{(2)}, (-\gamma^2 + \mathbb{D}^2) V_p^{(2)} \right) + & Ra_h \left(\bar{V}_q^{(2)}, T_p e_z \right) \\ & \left(\bar{V}_q^{(2)}, Q_h \left(Cos\chi \eta_m i + Sin\chi \mathbb{D} \right) B_p^{(2)} \right) & \\ 0 & \left(\bar{T}_q, V_p^{(2)} \cdot e_z \right) / 2Pr & \left(\bar{T}_q, \nabla^2 T_p \right) / Pr \end{bmatrix}}_{Stiffness-Matrix} \begin{bmatrix} a_p^{(1)} \\ a_p^{(2)} \\ b_p \end{bmatrix}.$$

$$(6.5)$$

The assumption of time dependence in the form $[a^{(1)} a^{(2)} b]^T \propto exp(\varsigma t)$ reduces the system to a generalized eigenvalue problem for the eigenvalues ς. The critical wave-number k_c and Rayleigh number Ra_c values for $Q = 100$ and for various angle χ values are listed in Table 6.1 for the rightmost eigenvalue just crossing the imaginary axis. These are obtained at the selection of $n = 1$ and $m = 0$ in (4.3), (4.4) and (4.5). The corresponding marginal stability curves for $Q = 100$ for $\chi = 0°$ to $\chi = 90°$ are plotted in Figure 6.1. These are in agreement with the linear analysis in Chandrasekhar [5] and Busse and Clever [18]. The increase in the critical wave numbers with increasing Chandrasekhar numbers is associated with the lateral dimension of the convective rolls, as stated in Chandrasekhar [5]. This is explained in the study of Burr and Müller, [38] by the lack of Joule dissipation for the vertical motions. Thus, the system reduces the horizontal motion in order to minimize the loss of Joule dissipation resulting in a decrease in the wavelength (increase in the wavenumber).

Table 6.1: Linear stability points for various Angle χ and wavenumber k_c for constant oblique magnetic field $Q = 100$

		Clever and Busse [18]	Present Work (Resolution)
Angle	k_c	Ra_c	Ra_c $(N_x \times N_y \times N_z)$
$\chi = 0°$	3.117	1707.8	1707.8 $(4 \times 4 \times 9)$
$\chi = 10°$	3.16	1781.0	1781.7 $(4 \times 4 \times 9)$
$\chi = 20°$	3.29	1984.9	1985 $(4 \times 4 \times 13)$
$\chi = 30°$	3.45	2281.3	2281.4 $(4 \times 4 \times 13)$
$\chi = 40°$	3.61	2625.5	2625.6 $(4 \times 4 \times 13)$
$\chi = 50°$	3.75	2974.7	2974.9 $(4 \times 4 \times 13)$
$\chi = 60°$	3.86	3290.7	3290.5 $(4 \times 4 \times 13)$
$\chi = 70°$	3.94	3541.3	3541.4 $(4 \times 4 \times 17)$
$\chi = 80°$	4.00	3701.9	3702.1 $(4 \times 4 \times 17)$
$\chi = 90°$	4.01	3757.2	3757.4 $(4 \times 4 \times 17)$
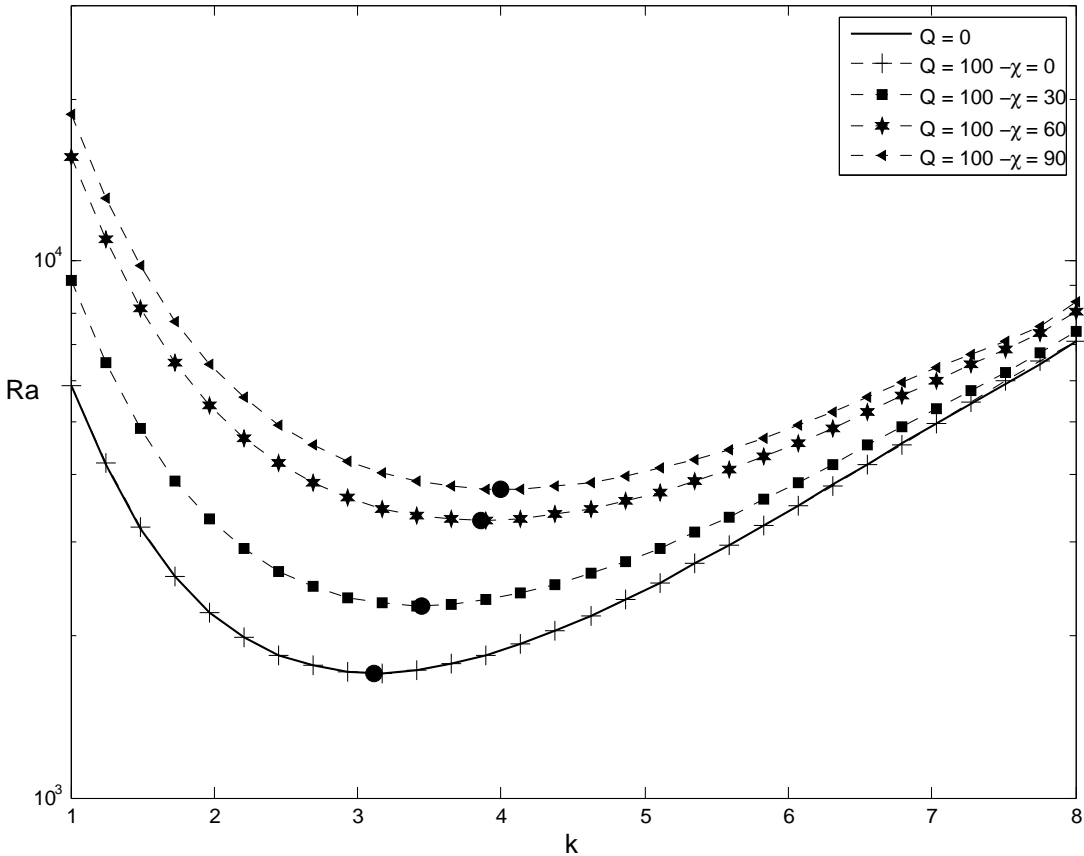
Figure 6.1: Stability curves for non-magnetic case and a fixed magnetic field ($Q = 100$)is applied at different angles. Solid circle shows critic wavenumber, k_c and corresponding critic Rayleigh number, Ra_c.

The verification of the claim that in the two dimensional roll regime, only the vertical component of the oblique magnetic field has an inhibition effect on the flow is shown in Figure 6.2. The results of the vertical magnetic field with intensity $QSin^2\chi$ is compared with inclined magnetic field Q with angle $\chi = 30°$ in Figure 6.2. This claim is also supported by Figure 6.3 and Figure 6.4 amongst the angle χ, critical Rayleigh number and the critical wave number. It can be observed from the Figure 6.3 and Figure 6.4, that, closer the angle to the vertical (horizontal), higher (lower) the critical Rayleigh number and and the critical wave number. In fact, in this regime the horizontal component contributes only to the alignment of the rolls along. In Figure 6.3 and Figure 6.4 critical Rayleigh number, $Ra_c(\chi, Q)$ and corresponding wave number, $k_c(\chi, Q)$ is always larger than the Rayleigh-Bénard convection.

Figure 6.2: Comparison the result of the vertical magnetic field $QSin^2\chi$ with inclined magnetic field Q with angle $\chi = 30°$, at $Q = 100$.

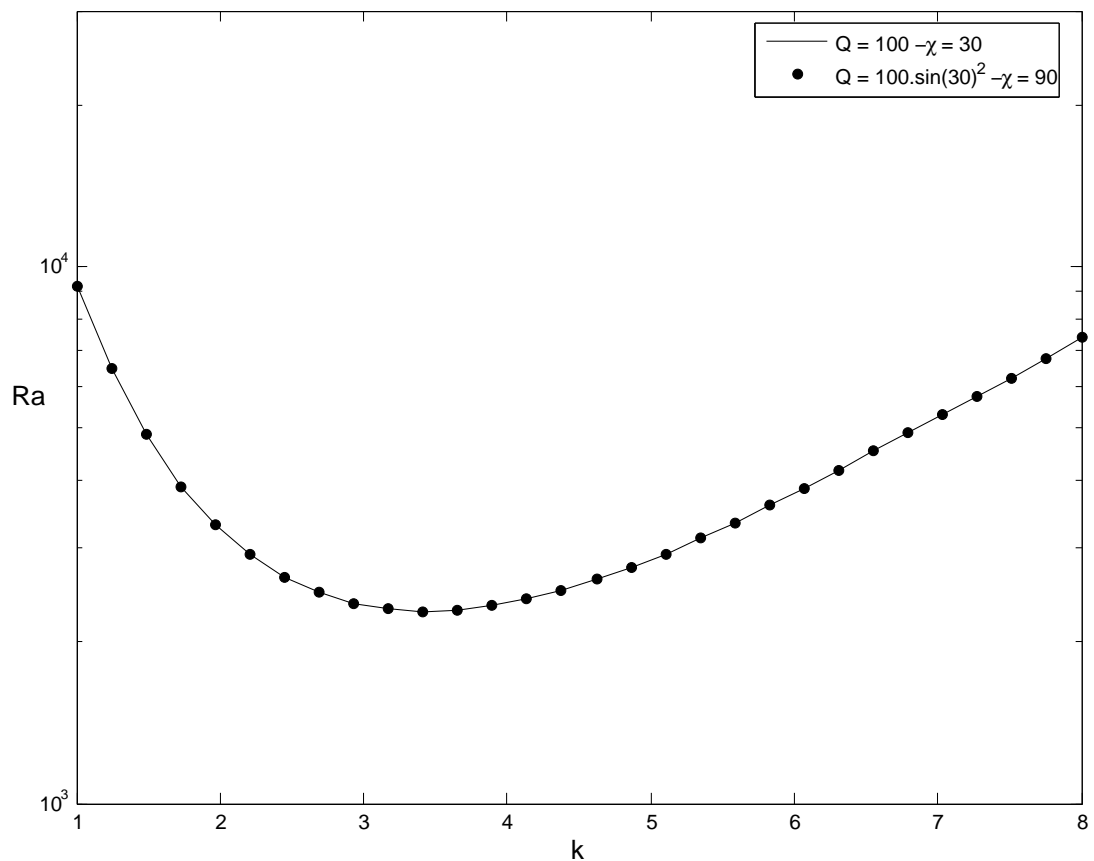And also, critical Rayleigh number and corresponding wave numbers are listed in Table6.2 for the onset of the convection in the presence of oblique magnetic field Q. This table gives an idea about the effects of the oblique magnetic field on the onset of the convection.

Table 6.2: Linear stability points for critic Rayleigh number Ra_c (upper number) and corresponding critic wavenumber k_c (lower number) for the onset of the convection in the presence of oblique magnetic field Q.

| Q	0°	10°	20°	30°	40°	50°	60°	70°	80°	90°
0	1707.8	1707.8	1707.8	1707.8	1707.8	1707.8	1707.8	1707.8	1707.8	1707.8
	3.117	3.117	3.117	3.117	3.117	3.117	3.117	3.117	3.117	3.117
100	1707.8	1781	1984.9	2281.3	2625.5	2974.7	3290.7	3541.3	3701.9	3757.2
	3.117	3.16	3.29	3.45	3.61	3.75	3.86	3.94	4	4.01
200	1707.8	1852.9	2246.4	2802	3435.2	4071.3	4644.3	5097.8	5388.5	5488.5
	3.117	3.21	3.43	3.68	3.91	4.1	4.25	4.36	4.42	4.45
300	1707.8	1923.6	2496.3	3290.7	4188.7	5088.4	5898.9	6540.8	6952.5	7094.3
	3.117	3.25	3.55	3.86	4.14	4.36	4.53	4.65	4.72	4.74
400	1707.8	1993.5	2737.6	3757.8	4906.2	6056.8	7094.6	7917.8	8445.1	8627.3
	3.117	3.31	3.67	4.02	4.32	4.56	4.76	4.87	4.96	4.97
500	1707.8	2061.8	2970.9	4207.9	5597.3	6991.1	8249	9247.6	9888.8	10109.8
	3.117	3.33	3.75	4.14	4.47	4.73	4.92	5.06	5.14	5.17
600	1707.8	2130	3198.5	4644.7	6268.6	7900.9	9374	10544	11297	11556
	3.117	3.385	3.82	4.27	4.61	4.83	5.06	5.20	5.28	5.31
700	1707.8	2196.9	3422	5074	6931.7	8798.6	10487	11829	12694	12990
	3.117	3.388	3.87	4.3	4.7	4.9	5.1	5.3	5.35	5.45
800	1707.8	2263	3640	5489	7569	9661	11556	13064	14034	14368
	3.117	3.39	3.96	4.44	4.8	5.1	5.31	5.45	5.53	5.59
900	1707.8	2328	3854	5900	8202	10520	12622	14295	15371	15743
	3.117	3.53	4.1	4.58	4.942	5.22	5.45	5.59	5.68	5.72
1000	1707.8	2393	4065	6302.8	8825	11367	13674	15510	16692	17101
	3.117	3.57	4.11	4.61	5.01	5.295	5.57	5.69	5.79	5.85
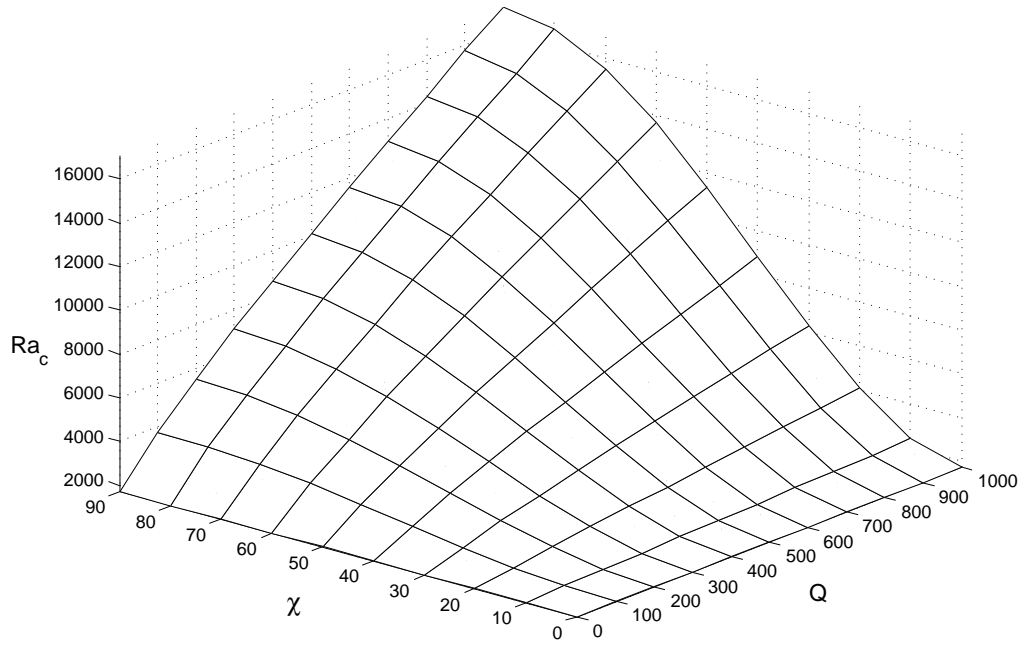
Figure 6.3: Critical Rayleigh numbers, Ra_c as a function of angle, χ and magnetic filed, Q.
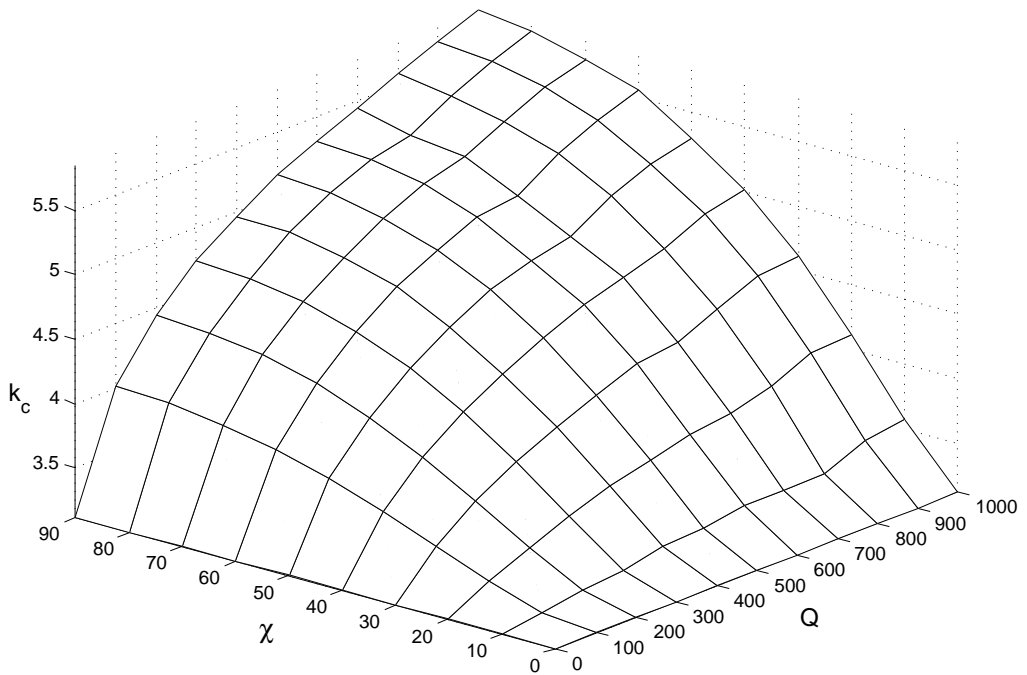

Figure 6.4: Critical wave numbers, k_c as a function of angle, χ and magnetic filed, Q.

84

6.2 Nonlinear Analysis

The numerical experiments are performed to study the effects of varying angle (χ) and Rayleigh number on the convective heat transport efficiency indicated by Nusselt number. We investigate the results in a square based convective box with the aspect ratio Γ [2.02 : 2.02] for small Prandtl number, $Pr = 0.05$, at the supercritical parameter values. While the magnetic field strength is kept at a constant value $Q = 100$, the Rayleigh number is increased and the external magnetic field angle χ is varied. The computation is started with the initial flow field just supercritical obtained using the eigenfunctions of the previous linear stability study. As shown in Figure 6.5, Nusselt number increases with Rayleigh number. However, at one point, at which the flow passes from stationary two dimensional roll motion to time periodic motion, Nusselt number suddenly drops and continue to increase as Rayleigh number increase. As Rayleigh number is further increased, the flow passes to the double periodic and then to chaotic regimes. This is also shown in Figures 6.6 to 6.9 by the emergence of toroidal component of kinetic energy at that point, up to which only the poloidal component of kinetic energy was present in the system.

Since the horizontal component of the magnetic field has only the effect of aligning the rolls along in the steady roll motion regime and the vertical magnetic field has an inhibition effect on the steady flow, the angle of the magnetic field is an important parameter at the point where the flow starts to oscillate. Chandrasekhar [5], Busse and Clever [18] and Burr Müller [39] state that the horizontal component of the magnetic field has no effect on the steady convection rolls until roll solutions begin to loose its stability. This is observed in this study. Therefore, the amplitude of the oscillations rises at $Ra \geq 12650$ for $\chi = 90°$, $Ra \geq 9000$ for $\chi = 60°$, $Ra \geq 5450$ for $\chi = 30°$ and $Ra > 2900$ for nonmagnetic cases. After the onset of oscillations, the horizontal component has more inhibition effect than the vertical component of the magnetic field [18]. This is observed in Figure 6.5 and that Nusselt number values for various angle values tend to get closer to each other as Rayleigh number increase. This means that the slope of the Nusselt-Rayleigh number curve decreases for smaller angle χ values that is closer to the horizontal axis. Furthermore, for high Rayleigh numbers the heat transport tends to decrease faster in the case of an oblique magnetic field at an angle closer to the horizontal axis.
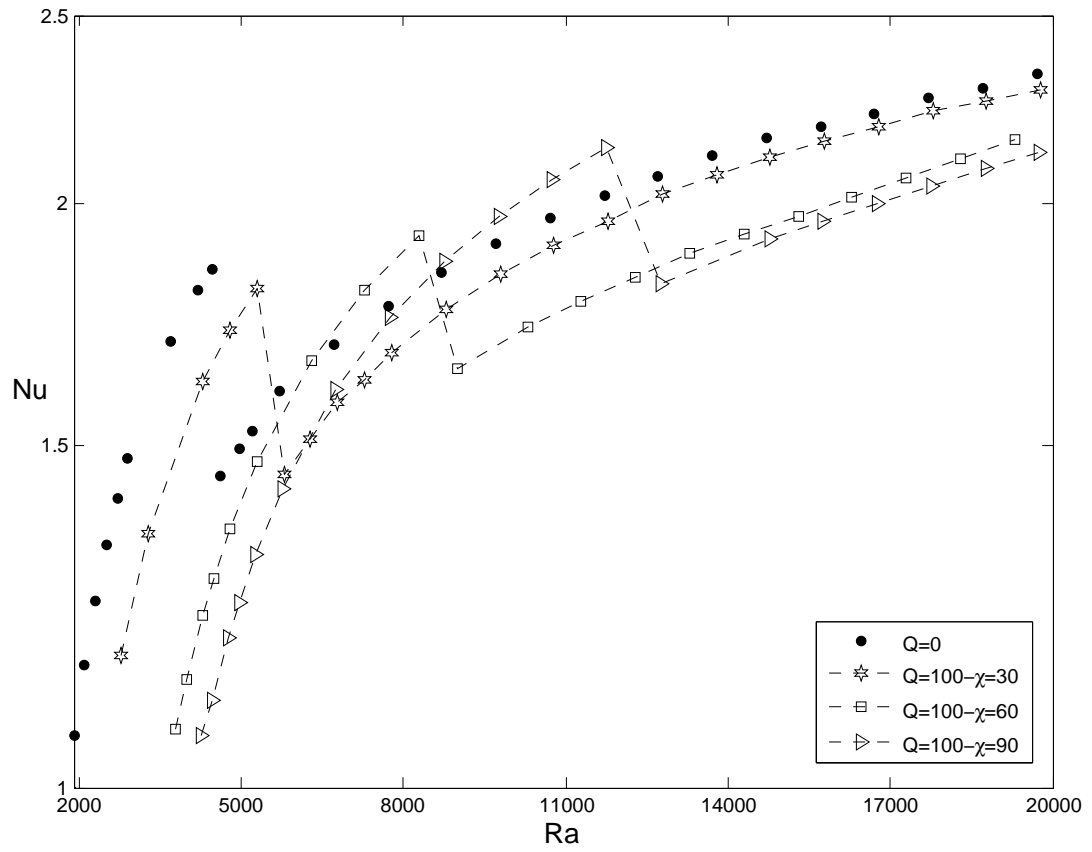
Figure 6.5: Nusselt versus Rayleigh number for different angle χ at $Pr = 0.05$, Γ [2.02 : 2.02] and $Q = 100$.

After this point oblique magnetic field with angle $\chi = 30°$ and $\chi = 60°$ are considered only. This selection is motivated by the associated directions being close to the horizontal and to the vertical, respectively. The detailed analysis of the vertical magnetic field in chapter 5 will serve as a reference state. First, the study of the oblique magnetic field with angle $\chi = 60°$ is performed.
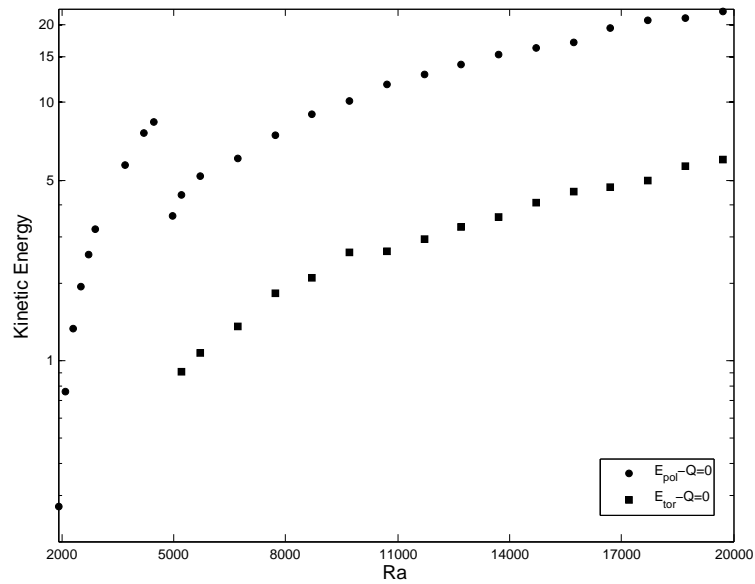
Figure 6.6: Poloidal and toroidal kinetic energy versus Rayleigh number for nonmagnetic case ($Q = 0$) at $Pr = 0.05$, Γ [2.02 : 2.02].

Figure 6.7: Poloidal and toroidal kinetic energy versus Rayleigh number for oblique magnetic field at angle $\chi = 30°$, $Pr = 0.05$, Γ [2.02 : 2.02] and $Q = 100$.

Figure 6.8: Poloidal and toroidal kinetic energy versus Rayleigh number for oblique magnetic field at angle $\chi = 60°$, $Pr = 0.05$, Γ [2.02 : 2.02] and $Q = 100$.
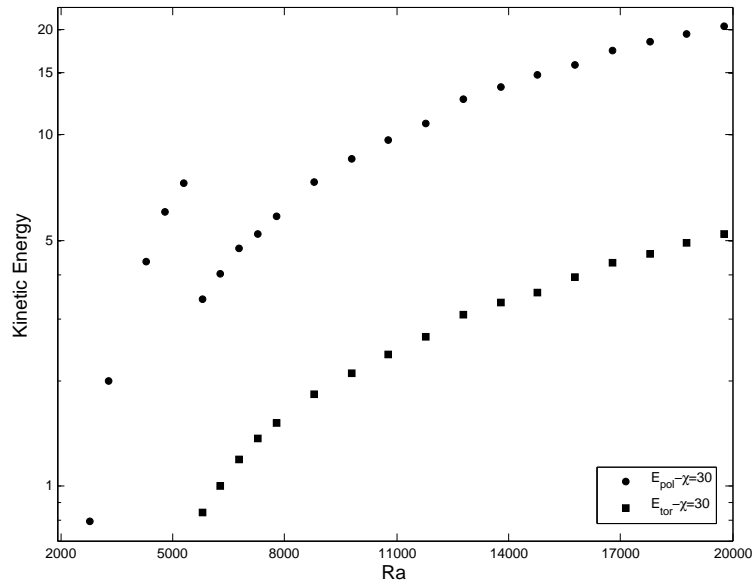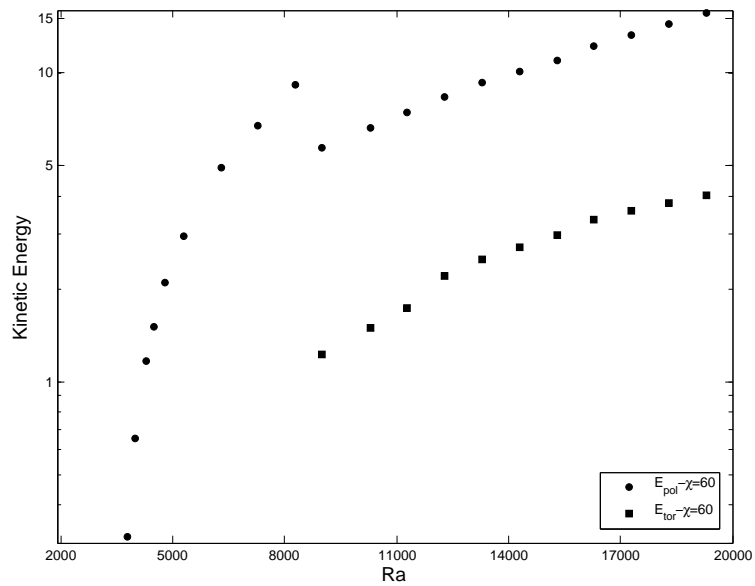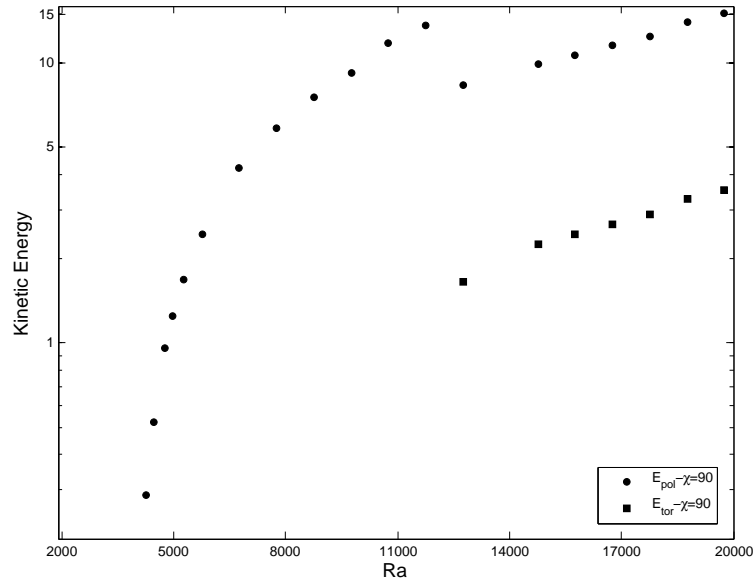
Figure 6.9: Poloidal and toroidal kinetic energy versus Rayleigh number for vertical magnetic field at angle $\chi = 90°$, $Pr = 0.05$, Γ [2.02 : 2.02] and $Q = 100$.

Transition to the oscillatory regime from the two dimensional steady parallel roll regime occurs at $Ra \geq 9000$ for an oblique magnetic field in the $yz-$plane with angle $\chi = 60°$ at $Q = 100$ and $Pr = 0.05$. The steady two dimensional rolls are observed in their projections onto $yz-$plane and onto the $xy-$plane in Figures 6.10 and 6.11 at $Ra = 8750$. If Rayleigh number is increased just above this value, oscillatory motion is observed in the $xy-$plane in Figure 6.12 and the rolls in the $yz-$plane appear in Figure 6.13 at $Ra = 9300$. At this value of Rayleigh number the flow is periodic and this period is computed using the frequency diagram in Figure 6.16. If Rayleigh number is further increased to $Ra = 10300$, the periodic regime gives way to a chaotic regime. As expected, the motion in the $xy-$plane becomes more complex (Figure 6.14) than $Ra = 9300$ and this can also be seen in the frequency diagram in Figure 6.17 where many more frequencies are excited.

89

Figure 6.10: Velocity field and temperature contour on *xy* plane at $z = 0.796$, $Ra = 8750$, Γ [2.02 : 2.02], $Pr = 0.05$, $\chi = 60°$ and $Q = 100$. Here, arrows shows the velocity field, solid lines indicate the temperature contour.
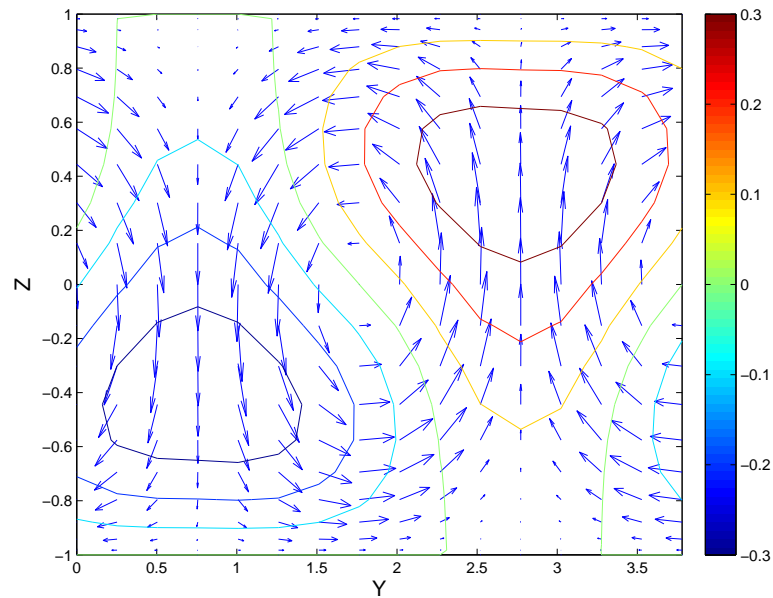
Figure 6.11: Velocity field and temperature contour on *yz* plane at $x = 0.7854$, $Ra = 8750$, Γ [2.02 : 2.02], $Pr = 0.05$, $\chi = 60°$ and $Q = 100$. Here, arrows shows the velocity field, solid lines indicate the temperature contour.
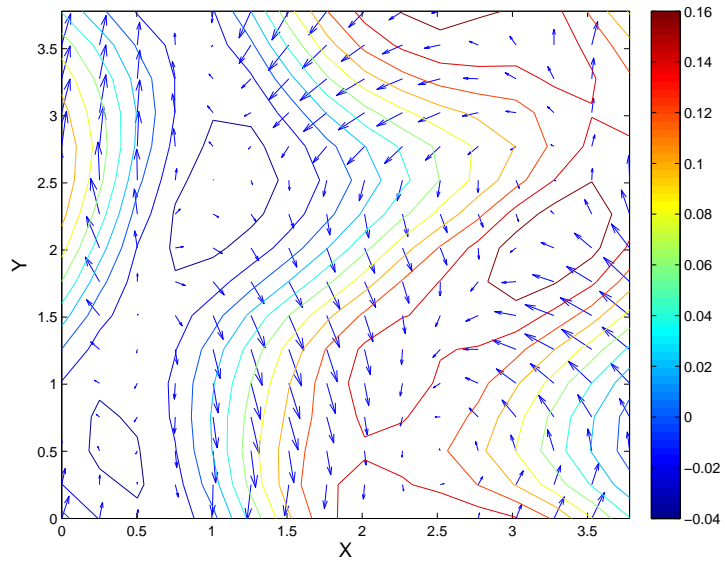
Figure 6.12: Velocity field and temperature contour on *xy* plane at $z = 0.796$, $Ra = 9300$, $\Gamma\,[2.02 : 2.02]$, $Pr = 0.05$, $\chi = 60°$ and $Q = 100$. Here, arrows shows the velocity field, solid lines indicate the temperature contour.

Figure 6.13: Velocity field and temperature contour on *yz* plane at $x = 0.7854$, $Ra = 9300$, $\Gamma\,[2.02 : 2.02]$, $Pr = 0.05$, $\chi = 60°$ and $Q = 100$. Here, arrows shows the velocity field, solid lines indicate the temperature contour.
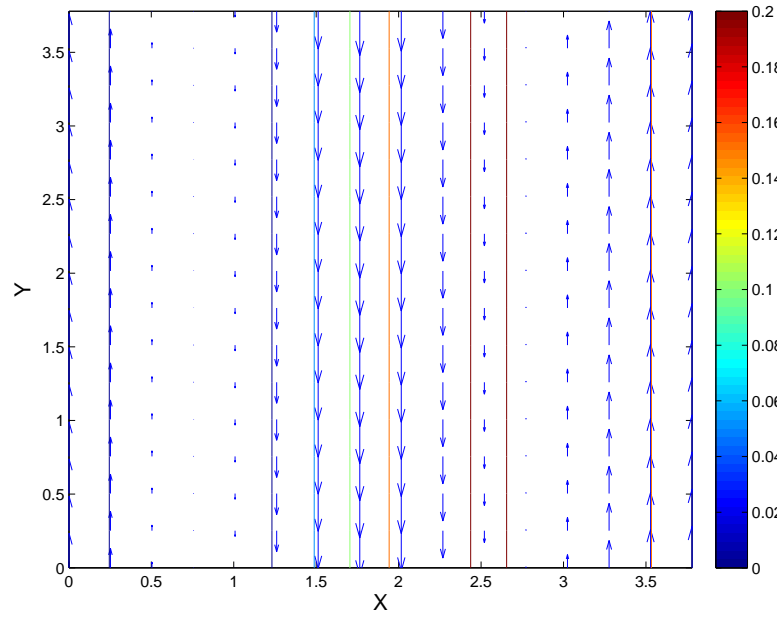
Figure 6.14: Velocity field and temperature contour on *xy* plane at $z = 0.796$, $Ra = 10300$, Γ [2.02 : 2.02], $Pr = 0.05$, $\chi = 60°$ and $Q = 100$. Here, arrows shows the velocity field, solid lines indicate the temperature contour.

Figure 6.15: Velocity field and temperature contour on *yz* plane at $x = 0.7854$, $Ra = 10300$, Γ [2.02 : 2.02], $Pr = 0.05$, $\chi = 60°$ and $Q = 100$. Here, arrows shows the velocity field, solid lines indicate the temperature contour.
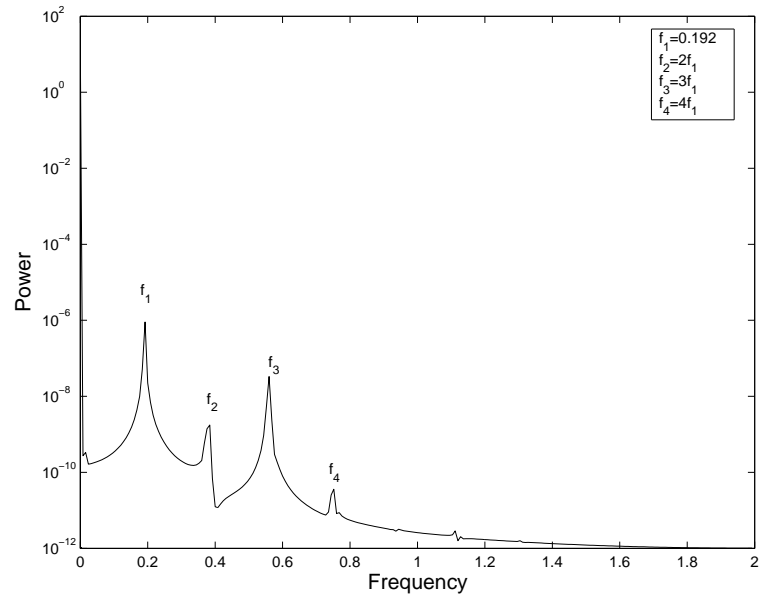
Figure 6.16: Frequency spectrum for $Ra = 9300$, $\Gamma [2.02 : 2.02]$, $Pr = 0.05$, $\chi = 60°$ and $Q = 100$.
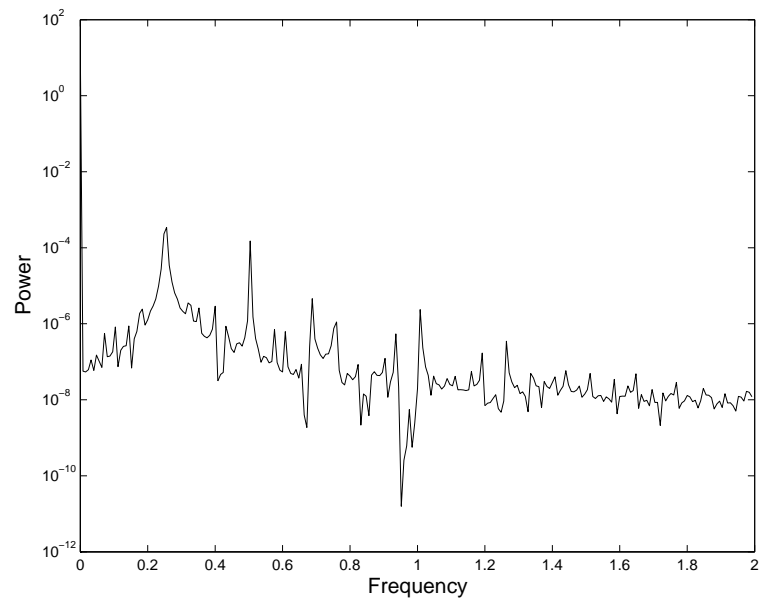
Figure 6.17: Frequency spectrum at $Ra = 10300$, $\Gamma [2.02 : 2.02]$, $Pr = 0.05$, $\chi = 60°$ and $Q = 100$.

Transition to the oscillatory regime from the two dimensional steady roll regime for an oblique magnetic field with an angle $\chi = 30°$ and $Q = 100$ occurs for $Ra > 5400$ before the transition for $\chi = 60°$. This is due to the angle $\chi = 30°$ being closer to the horizontal axis. The corresponding flow projections are shown in Figures 6.18, 6.19 for $Ra = 5400$, depicting two dimensional steady roll motion and in Figures 6.20 and 6.21 for $Ra = 5450$, depicting the fluctuations superimposed onto the two dimensional rolls. Except the differences at the transition Rayleigh number, the flow patterns are similar to those observed with angle $\chi = 60°$. The periodic motion is also depicted using the frequency diagram in Figure 6.24. As Rayleigh number is increased to $Ra = 6281$, the periodic regime gives way to chaotic motions. As expected, the screen-shot of the motion in the xy−plane become more complex in (Figure 6.22) in comparison to that for $Ra = 5450$ and this is also shown in the frequency diagram in Figure 6.25. In this frequency diagram besides the peaks representing the underlying flow, there exist peaks at various frequency values.
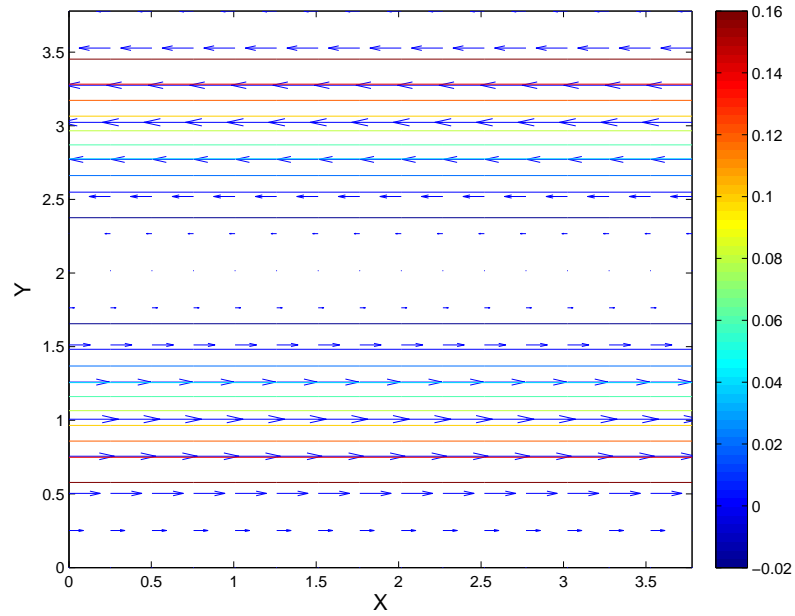
Figure 6.18: Velocity field and temperature contour on *xy* plane at $z = 0.796$, $Ra = 5400$, $\Gamma [2.02 : 2.02]$, $Pr = 0.05$, $\chi = 30°$ and $Q = 100$. Here, arrows shows the velocity field, solid lines indicate the temperature contour.
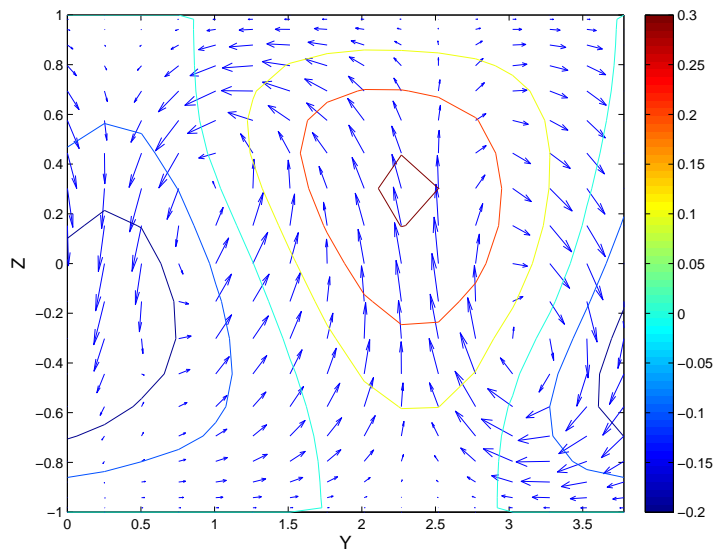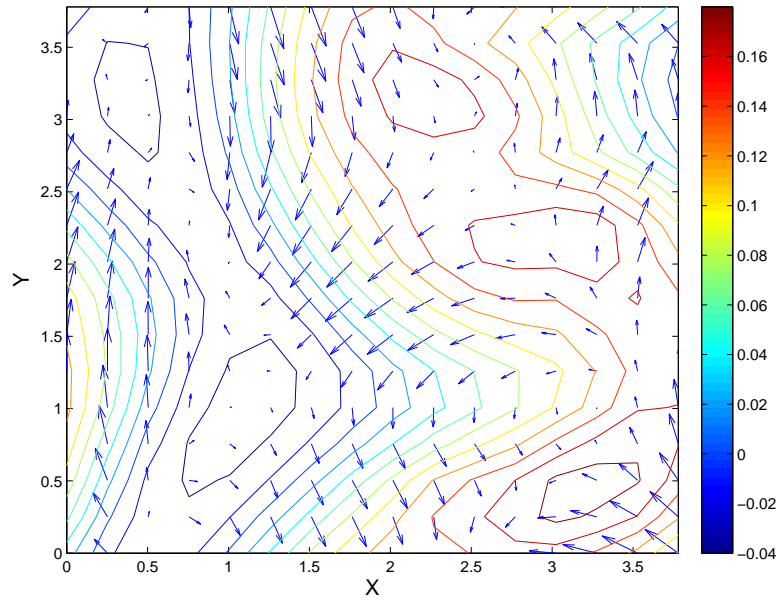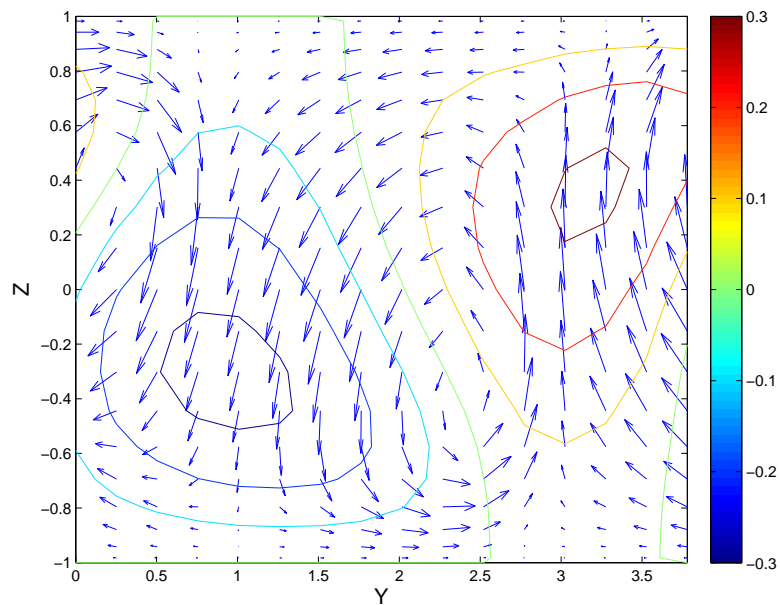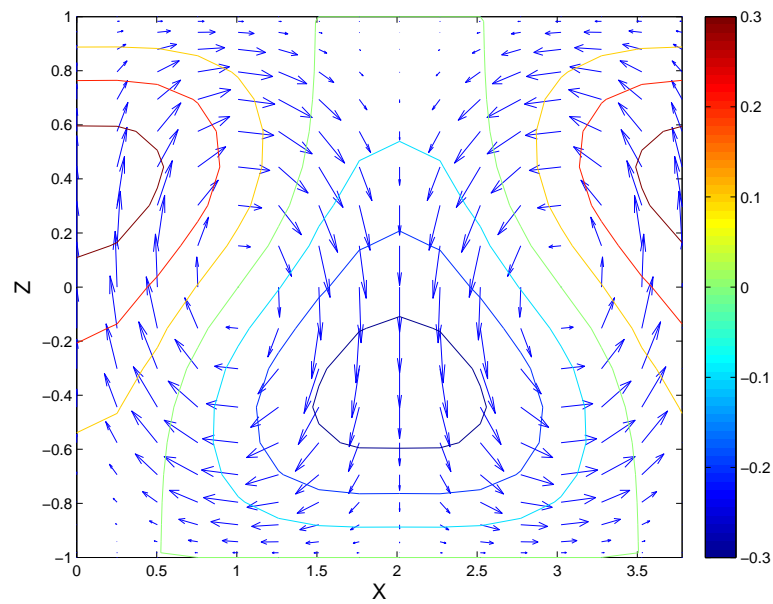

Figure 6.19: Velocity field and temperature contour on *xz* plane at $y = 0.7854$, $Ra = 5400$, $\Gamma [2.02 : 2.02]$, $Pr = 0.05$, $\chi = 30°$ and $Q = 100$. Here, arrows shows the velocity field, solid lines indicate the temperature contour.
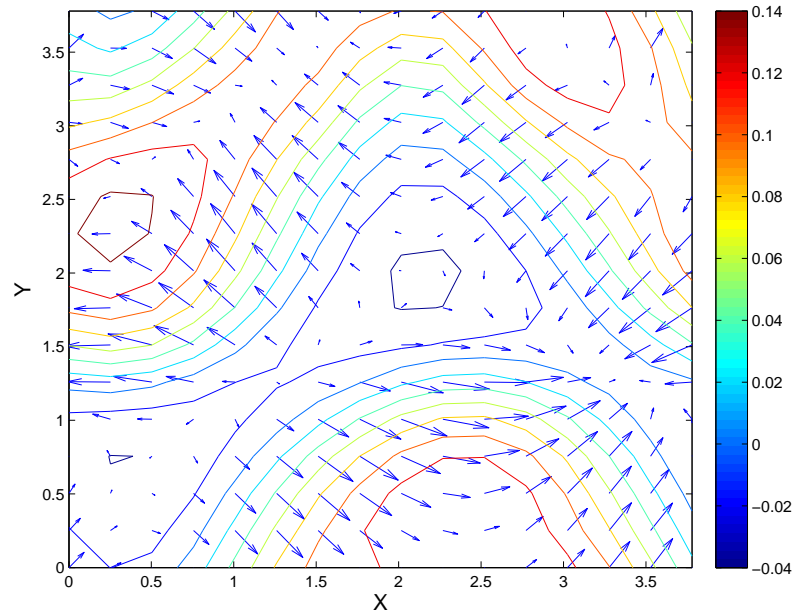
Figure 6.20: Velocity field and temperature contour on *xy* plane at $z = 0.796$, $Ra = 5450$, Γ [2.02 : 2.02], $Pr = 0.05$, $\chi = 30°$ and $Q = 100$. Here, arrows shows the velocity field, solid lines indicate the temperature contour.
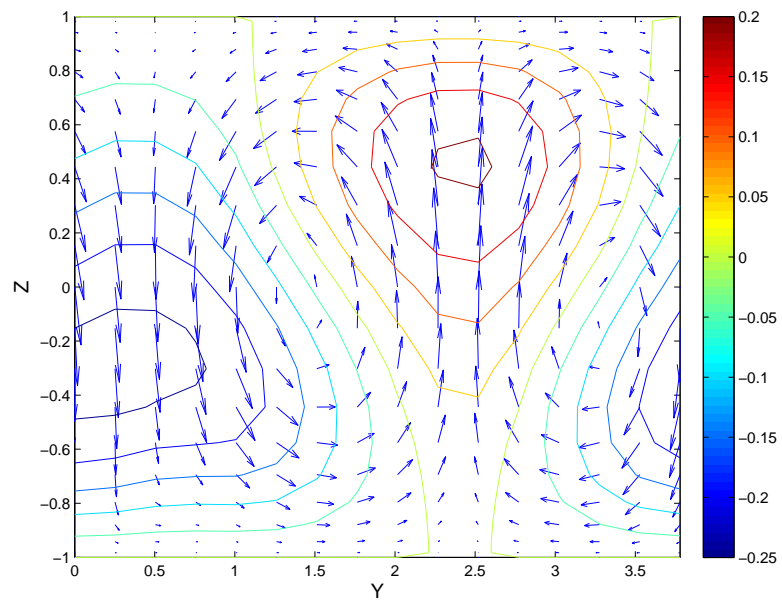

Figure 6.21: Velocity field and temperature contour on *xz* plane at $y = 0.7854$, $Ra = 5450$, Γ [2.02 : 2.02], $Pr = 0.05$, $\chi = 30°$ and $Q = 100$. Here, arrows shows the velocity field, solid lines indicate the temperature contour.
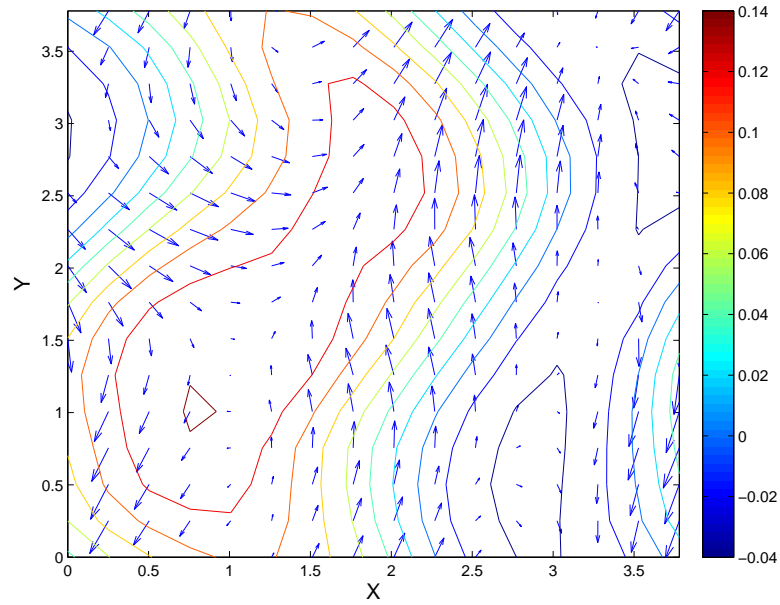
Figure 6.22: Velocity field and temperature contour on *xy* plane at $z = 0.796$, $Ra = 6281$, Γ [2.02 : 2.02], $Pr = 0.05$, $\chi = 30°$ and $Q = 100$. Here, arrows shows the velocity field, solid lines indicate the temperature contour.

Figure 6.23: Velocity field and temperature contour on *yz* plane at $x = 0.7854$, $Ra = 6281$, Γ [2.02 : 2.02], $Pr = 0.05$, $\chi = 30°$ and $Q = 100$. Here, arrows shows the velocity field, solid lines indicate the temperature contour.

Figure 6.24: Frequency spectrum at $Ra = 5450$, $\Gamma[2.02 : 2.02]$, $Pr = 0.05$, $\chi = 30°$ and $Q = 100$.
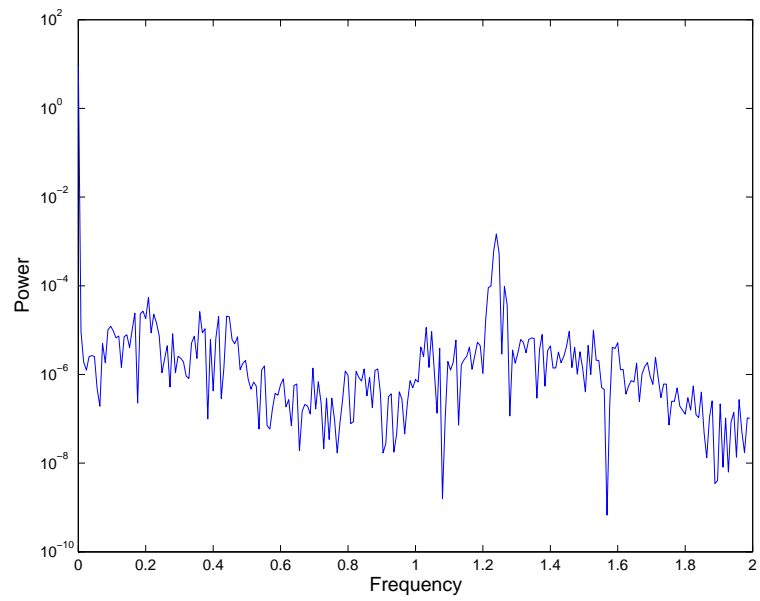
Figure 6.25: Frequency spectrum at $Ra = 6281$, $\Gamma[2.02 : 2.02]$, $Pr = 0.05$, $\chi = 30°$ and $Q = 100$.

CHAPTER 7

CONCLUSIONS

In this study, the effect of an imposed oblique magnetic field on the thermal convection in a layer of an electrically conducting low Prandtl fluids (i.e liquid metals) between rigid plates heated from below under the influence of gravity is numerically simulated in a computational domain with periodic horizontal extent. Due to the assumptions of the rigidity of the plate boundaries and periodicity in the horizontal extend, while no slip boundary conditions are used at the vertical boundaries, periodic boundary conditions are employed in the horizontal directions for the velocity and temperature components. The assumption of perfectly conducting plates dictated the magnetic boundary conditions. Rayleigh-Bénard convection in an electrically conducting fluid in the presence of magnetic field has long been studied both numerically and experimentally in literature. Solenoidal bases approach has been applied in various configurations and in various ways. The current flow configuration has been studied by Busse and Clever in [15] - [19] using solenoidal basis functions in a semi-analytic approach. However, the solenoidal bases approach used in this study is novel in the way of the construction and the approach in the flow configuration of thermal convection under a magnetic field. This approach provides a new perspective to numerical simulation of incompressible flows in efficiently overcoming the hurdle of treating the pressure variable.

The two crucial stages in this work are the use of the Legendre polynomials and the associated Gauss-Legendre-Lobatto (GLL) quadrature and the use the quasi-steady relationship between velocity and magnetic fields under the limit of $\kappa \ll \lambda$ to generate the solenoidal basis functions for the magnetic field from those constructed for the velocity field. Legendre polynomial representation provides a numerically stable interpolation property and the associated GLL quadrature provides the tools for accurate evaluation of the integrals arising in the formulation

of the model equations in the weak form. The construction of the solenoidal bases and their duals are easier in their representation in terms of Legendre polynomials. This is due to the unity weight associated with the integrals involving Legendre polynomials. The quasi-steady relationship between velocity and magnetic fields provides the link to carry the solenoidal property from velocity basis functions already constructed to be solenoidal to the magnetic bases in a manner inherent to the model system. These features help eliminating five equations from the model system. Moreover, careful construction of the dual bases help eliminating the pressure variable from the model system clearing an important obstacle towards an efficient numerical simulation.

In the time integration of the model equations, an implicit algorithm has high cost per time step. Therefore, in this study, time discretization is performed by a semi-implicit scheme composed of an explicit scheme for the nonlinear terms and of an implicit scheme for the linear terms in the models equations. Various combinations of explicit and implicit schemes such as second order explicit Adams-Bashforth (AB2) and implicit Crank Nicolson (CN) schemes, or Runge-Kutta schemes are tested for performance. It is observed that for short time integration second order Adams-Bashforth is quite satisfactory, but for long time integration it is not. Third order Adams-Bashforth scheme has performed satisfactorily for long time integration which is robust and less costly in comparison to fourth and higher order Runge-Kutta schemes as also stated in Boyd [41]. Thus, the non-linear advective terms are integrated explicitly using third order Adams-Bashforth and the linear terms integrated implicitly by third order Adams-Moulton schemes. So, the results represented in this study are third order accurate with time steps Δt varying in the interval $1 \times 10^{-3} < \Delta t < 1 \times 10^{-4}$.

First, the system is validated in linear stability analysis of conduction regime loosing its stability towards convective regime under the influence of vertical and oblique magnetic fields. The linear stability results obtained in this study is in good agreement with the experimental and theoretical studies in literature. This initial stage provided the necessary verification for the formulation and the implementation before attempting a nonlinear analysis. The numerical experiments in the nonlinear regime are implemented for the Rayleigh number in the range $1800 < Ra < 10^5$ and Chandrasekhar number in the range of $0 < Q < 4000$ for low Prandtl fluid (liquid metals). Computational tests were performed at different spatial and temporal resolutions and it is concluded that a spatial resolution of at most $16 \times 16 \times 21$ is necessary for satisfactory results. Many numerical experiments are performed in order to test and compare

our findings results against those in literature. With relatively lower resolution requirement in comparison to other work in literature, the current approach is tested to be robust and efficient.

7.1 Future Works

A future study of natural thermal convection under the influence of both magnetic field and rotation is a rational extension for the current numerical approach. The competing effects of magnetic field and rotation on thermal convection has been receiving attention in literature. Other geometries, such as cylindrical, spherical or rectangular without the periodic extent, may be considered for future study as well.

In general, time integration has been the most demanding part of this study. Due to time constraints, we refrain from experimenting with more time solvers. Fully implicit schemes with their more relaxed time step restrictions are worth to try as future improvements on this study. With the incorporation of outer Newton iterations as nonlinear system solver together with efficient iterative sparse linear system solvers for inner iterations, fully implicit methods may prove to be valuable.

The current computational approach for studying transitionary flow phenomena such as undertaken in this work may be adapted for a bifurcation study as flow parameters varied. Such a future study would be combining the efficiency of the current numerical approach with the well developed tools of bifurcation analysis for the model equations as a dynamical system.

REFERENCES

[1] Thompson, V., Thermal convection in a magnetic field, *Phi. Mag. Ser.*, **7**, 1417–1432 (1951).

[2] Chandrasekhar, S., On the inhibitions of convection by a magnetic field, *Phi. Mag. Ser.*, **7(340)**, 501–532 (1952).

[3] Lehnert, B., *Quart. App. Math.*, **12**, 321 (1955).

[4] Veronis, G., Cellular convection with finite amplitude in a rotating fluid, *J. Fluid Mech.*, **5**, 401–435 (1959).

[5] Chandrasekhar, S., Hydrodynamics and Hydromagnetic Instability, *Oxford: Clarendon Press*,(1961).

[6] Deissler, R.B., Magneto-fluid dynamic turbulence with a uniform imposed magnetic field, *Pyhs. Fluids*, **6**, 1250 (1963).

[7] Nestlerade J.A., Lumey, J.L., Initial response of the spectrum of isotropic turbulence to the sudden application of a strong magnetic field, *Pyhs. Fluids*, **6**, 1260 (1963).

[8] Nakagawa, Y., An experiment on the inhibition of thermal convection by a magnetic field, *Proc. R. Soc. Lond. A*, **175**, 417–419 (1955).

[9] Nakagawa, Y., Experiments on the Inhibition of Thermal Convection by a Magnetic Field, *Proc. R. Soc. Lond. A*, **240**, 108–113 (1957).

[10] Spiegel, E.A., Convection in stars II. Special effects, *Ann. Rev. Astron. Astrophys.*, **10**, 261–304 (1972).

[11] Weiss, N.O., Magnetic fields and convection, *Adv. Chem. Pyhs.*, **32**, 101–107 (1975).

[12] Busse, F.H., Nonlinear interaction of magnetic field and convection, *J. Fluid Mech.*, **71, part 1**, 193–206 (1975).

[13] Fauve, S., Laroche, C. and Libchaber, A., Effect of a horizontal magnetic field on convective instabilities in mercury, *J. Physique-Lettres*, **42**, 455–457 (1981).

[14] Proctor, M.R.E, Weiss, N.O., Magneto-convection, *Rep. Prog. Pyhs.*, **45**, 1317–1379 (1982).

[15] Busse, F.H. and Clever, R.M., Stability of convection rolls in the presence of a vertical magnetic field, *Phys. Fluids*, **25**, 931–935 (1982).

[16] Busse, F.H. and Clever, R.M., Stability of convection rolls in the presence of a horizontal magnetic field, *J. Méc. Théor. Appl.*, **2**, 495–502 (1983).

[17] Busse, F. H. and Clever, R. M., Nonlinear oscillatory convection in the presence of a vertical magnetic field, *J. Fluids Mech.*, **201**, 507–523 (1989).

[18] Busse, F. H. and Clever, R. M., Finite amplitude convection in the presence of an inclined magnetic field, *Eur. J. Mech.*, **9**, 225–238 (1990).

[19] Busse, F. H. and Clever, R. M., Three-dimensinal convection in the presence of strong vertical magnetic field, *Eur. J. Mech., B/Fluids*, **15**, 1–15 (1996).

[20] H. Ozoe and M. Maruo, 'Magnetic and gravitational natural convection of melted silicon-two dimensional numerical computations for the rate of heat transfer', *JSME*, **30**, 774–784 (1987).

[21] Orszag, S.A. and Kells, L.C., Transition to turbulence in plane Poiseuille flow and plane Couette flow, *J. Fluid Mech.*, **96**, 159–205 (1980).

[22] Kleiser, L. and Schumann, U., Treatment of incompressibility and boundary conditions in 3-D numerical spectral simulations of plane channel flows, in Hirschel, In proceedings of the *E.H. (ed.): Third GAMM Conference on Numerical Methods in Fluid Mechanics*, Vieweg, Braunschweig, 165–173 (1980).

[23] G. M. Oreper and J. Szekely, 'The effect of an externally imposed magnetic filed on bouyancy driven flow in a rectangular cavity', *J. Cryst. Growth*, **64**, 505–515 (1983).

[24] Canuto, C., Hussaini, M.Y., Quarteroni, A. and Zang, T.A., Spectral Methods: Evolution to Complex Domains and Applications to Fluid Dynamics, *Springer, New York*, (2007).

[25] MöBner , R. and Müller, U., A numerical investigation of three dimensional magneto convection in rectangular cavities, *Int. J. Heat Mass Transf.*, **42**, 1111–1121 (1999).

[26] Brackbill, J.U and Barnes, D.C., The effect of nonzero divergence on the numerical solution of the MHD equations, *J. Comp. Phys.*, **35**, 426–430 (1980).

[27] Balsara, D.S. and Kim, J., A comparison between divergence-cleaning and staggered-mesh formulations for numerical magnetohydrodynamics, *Astrophysical Journal*, **602**(2-I), 1079–1090 (2004).

[28] Leonard, A. and Wray, A., A new numerical method for the simulation of three-dimensional flow in a pipe, *NASA Technical Memorandum*, (1982).

[29] Moser, R. D., Moin, P., and Leonard, A., A spectral numerical method for the Navier-Stokes equations with applications to Taylor-Couette flow, *J. Comput. Phys.*, **52**, 524–544 (1983).

[30] Mhuiris, N.M.G., The construction and use of divergence free vector expansions for incompressible fluid flow calculations, *NASA Technical Memorandum*, (1986).

[31] Pasquarelli, F., Quarteroni, A., and Sacchi-Landriani, G., Spectral approximations of the Stokes problem by divergence-free functions, *J. Sci. Comput.*, **2**, 195–226 (1987).

[32] Kessler, R., Nonlinear transition in three-dimensional convection, *J. Fluid Mech.*, **174**, 357–379 (1987).

[33] Noack, B.R. and Eckelmann, H., A low-dimensional Galerkin method for the three-dimensional flow around a circular cylinder, *Phys. Fluids*, **6**(1), 124–143 (1994).

[34] Meseguer, A. and Trefethen, L.N., Linearized pipe flow to Reynolds number 10^7, *J. Comp. Phys.*, **186**, 178–197 (2003).

[35] Tarman, I. H., Reduced order modeling of thermal convection under a magnetic field, In proceedings of the *European Conference on Computational Fluid Dynamics*, WCCM8 - ECCOMAS 2008.

[36] Aurnou, J. M. and Olson, P. L., Experiments on Rayleigh Benard convection, magneto convection and rotating magneto convection in liquid gallium, *J. Fluid Mech.*, **430**, 283–307 (2001).

[37] Güray, E. and Tarman, I. H.,Thermal convection in the presence of a vertical magnetic field, *ACTA Mechanica*, **194**, 33–46 (2007).

[38] Burr, U. and Müller, U., Rayleigh-Bénard convection in liquid metal layers under the influence of a vertical magnetic field, *Phys. Fluids*, **13**, 3247–3257 (2001).

[39] Burr, U. and Müller, U., Rayleigh-Bénard convection in liquid metal layers under the influence of a horizontal magnetic field, *J. Fluid Mech.*, **453**, 345–369 (2002).

[40] Davidson, P. A., An Introduction to Magnetohydrodynamics, *Cambridge University Press*,(2001).

[41] Boyd, J. P., Chebyshev and Fouries Spectral Methods, *New York: Springer-Verlag*,(1989).

[42] Reid, W. H. and Harris, D. L., Some further results on the Bénard problem, *Phys. Fluids*, **1**, 102–110, 1958

[43] Peyret, R., Spectral Methods for incompressible flow, *New York: Springer*,(2000).

[44] Weideman J. A. C., Reddy S. C., A MATLAB Differentiation Matrix Suite, ACM Transactions on Mathematical Software, 26, pp. 465-519, 2000

[45] Haidvogel D. B, Zang T., The accurate solution of Poisson's equations by expansion, *J. Comp. Phys.*, **30**, 167–180 (1979).

[46] Kurt E., Busse F. H. and Pesch W., Hydrodynamic convection in a rotating annulus with an azimuthal magnetic field, *Theoret. Comput. Fluid Dynamics*, **18**, 251–263 (2004).

[47] Kurt E., Busse F. H. and Pesch W., Pattern formation in the rotating annulus with an azimuthal magnetic field at low Prandtl Numbers, *Journal of Vibration and Control*, **13**, 1321–1330 (2006).

[48] Yıldırım, C. and Yarımpabuç, D. and Tarman, H. I., Transitional Dynamics in Thermal Convection Between Rigid Plates, *Journal of Vibration and Control*, **13**, 1331–1342 (2007).

[49] Yarımpabuç, D. and Tarman, H. I., Numerical Simulation of Thermal Convection Under the Influence of a Magnetic Field by Using Solenoidal Bases, *ECCOMAS CFD 2010 Conference, Lisbon, Portugal*, **1**, 102 (June 2010).

APPENDIX A

ANALYTICAL SOLUTION FOR MAGNETIC BASES

Analytical solution of magnetic bases for the vertical case will only be shown in this section. The other cases can be made in similar manner. Let's consider the boundary value problem (3.35) obtained from the quasi-steady relation (3.32):

$$\mathbb{D}^2\mathbf{B} - \gamma^2\mathbf{B} = -\mathbb{D}\mathbf{V}, \tag{A.1}$$

for $\mathbf{B}(z)$ subject to the boundary conditions

$$\mathbb{D}B_x = \mathbb{D}B_y = B_z = 0 \quad \text{at} \quad z = \pm 1. \tag{A.2}$$

Horizontal and vertical components of the boundary value problem according to the type of the boundary conditions can be written separately by the following way:

$$\mathbb{D}^2 B_x - \gamma^2 B_x = -\mathbb{D}V_x = f_x(z), \quad with \quad \mathbb{D}B_x(z = \pm 1) = 0 \tag{A.3}$$

$$\mathbb{D}^2 B_y - \gamma^2 B_y = -\mathbb{D}V_y = f_y(z), \quad with \quad \mathbb{D}B_y(z = \pm 1) = 0 \tag{A.4}$$

$$\mathbb{D}^2 B_z - \gamma^2 B_z = -\mathbb{D}V_z = f_z(z), \quad with \quad B_z(z = \pm 1) = 0 \tag{A.5}$$

Since the boundary type of the x and y component are the same, only the solution of the x and z component will be done. By using separation of variables method, homogeneous and particular solution of the equations (A.3) can be written as follows:

$$B_{xh} = C_1 cosh\left(\gamma\left(z+1\right)\right) + C_2 sinh\left(\gamma\left(z+1\right)\right) \tag{A.6}$$

$$B_{xp} = u_1 cosh\left(\gamma\left(z+1\right)\right) + u_2 sinh\left(\gamma\left(z+1\right)\right) \tag{A.7}$$

where

$$\mathbb{D}u_1 = \frac{w_1}{w} \qquad \mathbb{D}u_2 = \frac{w_2}{w} \tag{A.8}$$

such that

$$w_1 = \begin{vmatrix} 0 & sinh\,(\gamma\,(z+1)) \\ f_x(z) & \gamma cosh\,(\gamma\,(z+1)) \end{vmatrix} = -f_x(z)sinh\,(\gamma\,(z+1)), \tag{A.9}$$

$$w_2 = \begin{vmatrix} cosh\,(\gamma\,(z+1)) & 0 \\ \gamma sinh\,(\gamma\,(z+1)) & f_x(z) \end{vmatrix} = f_x(z)cosh\,(\gamma\,(z+1)), \tag{A.10}$$

$$w = \begin{vmatrix} cosh\,(\gamma\,(z+1)) & sinh\,(\gamma\,(z+1)) \\ \gamma sinh\,(\gamma\,(z+1)) & \gamma cosh\,(\gamma\,(z+1)) \end{vmatrix} = \gamma. \tag{A.11}$$

Therefore $\mathbb{D}u_1$ and $\mathbb{D}u_2$ can be written in the following form:

$$\mathbb{D}u_1 = -\frac{1}{\gamma}f_x(z)sinh\,(\gamma\,(z+1)) \qquad \mathbb{D}u_2 = \frac{1}{\gamma}f_x(z)cosh\,(\gamma\,(z+1)) \tag{A.12}$$

and then particular solution becomes,

$$B_{xp} = -\frac{1}{\gamma}cosh\,(\gamma\,(z+1)) \int\limits_{-1}^{z} f_x(\tau)sinh\,(\gamma\,(\tau+1))\,d\tau +$$

$$\frac{1}{\gamma}sinh\,(\gamma\,(z+1)) \int\limits_{-1}^{z} f_x(\tau)cosh\,(\gamma\,(\tau+1))\,d\tau. \tag{A.13}$$

So, the analytical solution of the equation (A.3) is the sum of the homogeneous and particular solution and written as follows:

$$B_x = C_1cosh\,(\gamma\,(z+1)) + C_2sinh\,(\gamma\,(z+1)) - \frac{1}{\gamma}cosh\,(\gamma\,(z+1)) \int\limits_{-1}^{z} f_x(\tau)sinh\,(\gamma\,(\tau+1))\,d\tau +$$

$$\frac{1}{\gamma}sinh\,(\gamma\,(z+1)) \int\limits_{-1}^{z} f_x(\tau)cosh\,(\gamma\,(\tau+1))\,d\tau. \tag{A.14}$$

with Neumann type boundary conditions $\mathbb{D}B_x(z = -1) = 0$ and $\mathbb{D}B_x(z = 1) = 0$. It can be easily shown that the constant C_2 becomes zero ($C_2 = 0$) for $\mathbb{D}B_x(z = -1) = 0$. The other constant C_1 is calculated from the boundary condition $\mathbb{D}B_x(z = 1) = 0$ in the following way:

$$C_1 = -\frac{1}{\gamma}\frac{cosh\,(2\gamma)}{sinh\,(2\gamma)} \int\limits_{-1}^{1} f_x(\tau)cosh\,(\gamma\,(\tau+1))\,d\tau + \frac{1}{\gamma} \int\limits_{-1}^{1} f_x(\tau)sinh\,(\gamma\,(\tau+1))\,d\tau. \tag{A.15}$$

If the calculated value of the constants C_1 and C_2 are put into equation (A.14) and rearranged, x component of the solenoidal magnetic bases takes the following form:

$$B_x = -\frac{cosh\,(\gamma\,(z-1))}{\gamma\,sinh\,(2\gamma)} \int\limits_{-1}^{1} f_x(\tau)cosh\,(\gamma\,(\tau+1))\,d\tau$$

$$+\frac{cosh\,(\gamma\,(\tau+1))}{\gamma} \int\limits_{z}^{1} f_x(\tau)sinh\,(\gamma\,(\tau+1))\,d\tau$$

$$-\frac{sinh\,(\gamma\,(\tau+1))}{\gamma} \int\limits_{z}^{1} f_x(\tau)cosh\,(\gamma\,(\tau+1))\,d\tau. \tag{A.16}$$

Here the function $f_x(z)$ is the n-th degree Legendre polynomial. The integrals in the equation (A.16) can easily be solved by using integration by parts rule.

The z component of the solenoidal magnetic bases can be solved in the same way of the equation (A.3), so the equation (A.14) is rearranged and written as follows:

$$B_z = C_3 cosh\,(\gamma\,(z+1)) + C_4 sinh\,(\gamma\,(z+1)) - \frac{1}{\gamma}cosh\,(\gamma\,(z+1)) \int\limits_{-1}^{z} f_z(\tau)sinh\,(\gamma\,(\tau+1))\,d\tau +$$

$$\frac{1}{\gamma}sinh\,(\gamma\,(z+1)) \int\limits_{-1}^{z} f_z(\tau)cosh\,(\gamma\,(\tau+1))\,d\tau. \tag{A.17}$$

with Dirichlet type boundary conditions $B_z(z = -1) = 0$ and $B_z(z = 1) = 0$. It can be easily shown that the constant C_3 becomes zero ($C_3 = 0$) for $B_z(z = -1) = 0$. The other constant C_4 is calculated from the boundary condition $B_z(z = 1) = 0$ in the following way:

$$C_4 = \frac{1}{\gamma}\frac{cosh\,(2\gamma)}{sinh\,(2\gamma)} \int\limits_{-1}^{1} f_z(\tau)sinh\,(\gamma\,(\tau+1))\,d\tau - \int\limits_{-1}^{1} f_x(\tau)cosh\,(\gamma\,(\tau+1))\,d\tau. \tag{A.18}$$

If the calculated value of the constants C_3 and C_4 are put into equation (A.18) and rearranged, z component of the solenoidal magnetic bases becomes:

$$B_z = \frac{sinh\,(\gamma\,(z-1))}{\gamma\,sinh\,(2\gamma)} \int\limits_{-1}^{1} f_z(\tau)sinh\,(\gamma\,(\tau+1))\,d\tau$$

$$+\frac{cosh\,(\gamma\,(\tau+1))}{\gamma} \int\limits_{z}^{1} f_z(\tau)sinh\,(\gamma\,(\tau+1))\,d\tau$$

$$-\frac{sinh\,(\gamma\,(\tau+1))}{\gamma} \int\limits_{z}^{1} f_z(\tau)cosh\,(\gamma\,(\tau+1))\,d\tau. \tag{A.19}$$

CURRICULUM VITAE

PERSONAL INFORMATION

- **Surname, Name**   :Yarımpabuç, Durmuş

- **Nationality**   :Turkish

- **Date and Place of Birth** :23 January 1979, Antakya

- **Marital Status**   :Single

- **E-mail**   :durmusuz@gmail.com

EDUCATION

- Antakya High School, 1997.

- B.S. Department of Mathematics, Hacettepe University, 2002.

WORK EXPERIENCE

Year	**Place**	**Enrollment**
August 2002- Present	METU Dept. of Engineering Sciences	Research Assistant
September 2007 - Febuary 2008	TU Delft (NETHERLAND)	Visiting Scholar

FOREIGN LANGUAGES

- English (fluent)

COMPUTER EXPERIENCE

- **Operating System**   :Windows XP, Linux

- **Programming Language** :FORTRAN, Jawa

- **Computing Software** :Matlab, Mathematica, Mathcad

AWARDS

- Honor award provided by Sakarya University in 1998

- First Degree Award provided by provided by Hacettepe University in 2001-2002

- İhsan DOĞRAMACI Superior Success Award provided by Hacettepe University in 2002

PUBLICATIONS

Journal Articles

- Yarımpabuç, D. and Tarman, H. I.,Numerical Simulations of Thermal Convection under the Influence of Oblique Magnetic Field by Using Solenoidal Bases. In preparation.

- Yarımpabuç, D. and Tarman, H. I.,Numerical Simulations of Thermal Convection under the Influence of a Magnetic Field by Using Solenoidal Bases at low Prandtl Numbers. Submitted.

- Yıldırım, C. and Yarımpabuç, D. and Tarman, H. I., Transitional Dynamics in Thermal Convection Between Rigid Plates, *Journal of Vibration and Control*, **13**, 1331–1342 (2007).

Proceedings

- Yarımpabuç, D. and Tarman, H. I., Numerical Simulation of Thermal Convection Under the Influence of a Magnetic Field by Using Solenoidal Bases, *ECCOMAS CFD 2010 Conference, Lisbon, Portugal*, **1**, 102 (June 2010).

- Yarımpabuç, D. and Tarman, H. I., Numerical Simulation of Long Wave Run-up on a Sloping Beach, XV. Ulusal Mekanik Kongresi (XV. National Congress of Mechanics), Kayseri, Turkey (2009)

- Yıldırım, C. and Yarımpabuç, D. and Tarman, H. I., Transitional Dynamics in Thermal Convection Between Rigid Plates, *Mathematical Methods in Engineering International Symposium, Ankara, Turkey*, (April, 2006).

Reports

- D. Yarımpabuç and M.B. van Gijzen, Spectral deflation applied to Helmholtz problems that are preconditioned with a shifted Laplacian. Technology University of Delft, 2008.

SOCIAL ACTIVITIES

- I am a member of METU Subaqua Society 01 September 2004 till date. METU Subaqua Society have made scientific research in shoreline of Turkey since 1985(www.sat.metu.edu.tr).